

An External Calibration System for DBF Receiver Arrays at Ka-Band

Minh Nhat Pham



An External Calibration System for DBF Receiver Arrays at Ka-Band

Vom Promotionsausschuss der
Technischen Universität Hamburg
zum Erlangen des akademischen Grades
Doktor-Ingenieur (Dr.-Ing.)
genehmigte Dissertation

von

Minh Nhat Pham

aus

Ho-Chi-Minh Stadt, Vietnam

2019

-
1. Gutachter: Prof. Dr.-Ing. Arne F. Jacob
 2. Gutachter: Prof. Dr.-Ing. Peter Knott

Tag der mündlichen Prüfung: 28th November 2018

Acknowledgement

This work was done during my time being a member of the scientific staff at the Institut für Hochfrequenztechnik, Technische Universität Hamburg. Firstly I would like to express my gratitude to my *Doktorvater*, Prof. Dr.-Ing. Arne F. Jacob for his continuous guidance and encouragement to my Ph.D study and research, for his trust, patience and motivation. Besides my advisor, I would like to thank Prof. Dr.-Ing. Peter Knott for the valuable insightful comments and input.

I would also like to show my appreciation to my co-workers in the institute for the pleasant and productive working environment. In particular, I am grateful to Dipl.-Ing. Thomas Jaschke and Dipl.-Ing. Benjamin Rohrdantz for all the invaluable technical discussions. Additionally, I am indebted to Mrs. Carmen Hajunga, Mrs. Anja-Maria Doobe-Jöstingmeier and Dipl.-Ing. Jürgen Winkelmann for all support in the experiments.

Last but not least, I would like to thank my parents for all their love and assistance to me in all my pursuits. And most of all for the love and faithful support to enable this work of my supportive and patient wife Hoa Dang, and my two charming children Hien and Bach Pham are deeply appreciated.

Leinfeld-Echterding, January 2019

Minh Nhat Pham

Abstract

The approach of phased arrays with digital beam forming (DBF) is interesting for satellite communication systems. However, a complex system of large-size arrays with more than 1000 channels is necessary. Thus, one of the most critical tasks is integrating and controlling a huge number of active and passive components in a compact system.

The topic of the present dissertation is the development and the analysis of an online calibration system with probes surrounding the DBF receiver array. In comparison to other concepts in literature, this so-called external concept is chosen for large-size arrays because of its low impact on the integration density and its moderate hardware complexity. This thesis discusses its applicability to the calibration of channel deviations and its extension to further include their mutual coupling in a joint procedure.

Three aspects of the calibration procedure for channel deviations are improved, namely the probe design, the model of the probe-receiver coupling, and the algorithmic part.

- The probes are realized as coaxial monopole antennas with an approximately omni-directional radiation pattern to improve their robustness against fabrication tolerances.
- An analytical model of the probe-receiver coupling is developed to enhance the accuracy with acceptable computational complexity.
- A combination of the arithmetical and the geometrical mean is proposed to improve the stability of the calibration procedure.

In addition, the concept is extended towards a joint calibration of the channel deviations and their mutual coupling. A simplified model of the coupling matrix of a receiver system is shown to be necessary to limit the hardware cost. Additionally, three decoupling algorithms are considered. The common Least-Square (LS) method is the first approach in case of a large number of probes and calibration signals with a high signal-to-noise-ratio (SNR). Furthermore, the necessity of at least one separate reference channel is demonstrated. In the second approach, the LS algorithm is complemented by a Principle Component Analysis (PCA). The accuracy is shown to be improved for a limited number of probes. However, the approach is suitable only for the calibration of small-size receiver arrays because of the required high signal-to-noise ratio (SNR) and the huge computational cost. Finally, an extension of LS with multiple reference receivers (MRR) is suggested to diversify

the modeling errors and to achieve the best possible calibration accuracy for a limited SNR. Although the hardware cost is higher, this approach is relevant for the calibration of a large-size array.

The usefulness of the proposed calibration procedure is demonstrated in laboratory experiments with linear and planar receiver arrays. The correction of the main beam direction as well as the improvement of the side-lobe level of the receiver array are reported.

Finally, a tolerance analysis is performed to determine the technical requirements of the calibration system, such as the number of probes and reference channels or the required SNR of the calibration signals.

Contents

1	Introduction	1
1.1	Context	1
1.2	Formulation of the Problem	3
1.3	Thesis Topic and Outline	4
2	Antenna Basics	7
2.1	Antenna Parameters	7
2.2	Polarization	10
2.3	Receiver System	11
2.4	Tolerance effects	14
3	Calibration Concept	18
3.1	Error Sources	18
3.1.1	Channel fluctuations	18
3.1.2	Mutual Coupling	19
3.2	Calibration Concepts	21
3.2.1	Internal Calibration Concept	23
3.2.2	External Calibration Concept	24
3.2.3	Calibration Procedure	26
3.3	Conclusion	27
4	Calibration of Channel Deviations	29
4.1	Calibration Probes	30
4.2	Probe-Patch Coupling	31
4.2.1	Analytical Model	31
4.2.2	Propagation model K_1	32
4.2.3	Radiation characteristics K_2 of the patch	36
4.2.4	Model Expansion with Superposition Principle	37
4.3	Algorithms	38
4.4	Simulation	40
4.5	Summary	41

5	Calibration of Coupling Matrix	43
5.1	Coupling Matrix	43
5.2	Decoupling Algorithms	45
5.2.1	Calibration Procedure	45
5.2.2	Least-Square (LS) Method	49
5.2.3	Principle Component Analysis (PCA)	49
5.2.4	Extension with Multiple reference receivers (MRR)	50
5.3	Simulation	52
5.4	Summary	55
6	Experiments	56
6.1	Measurement Setup	56
6.2	Microstrip Probe	58
6.3	Coaxial Probe	59
6.3.1	Calibration of Channel Fluctuations	59
6.3.2	Joint Calibration of Channel Fluctuations and Mutual Coupling	64
6.4	Summary	71
7	Tolerance Analysis and Scalability	73
7.1	Surrogate model	74
7.2	Uncertainty Propagation	75
7.3	Effects on the Beam Pattern	76
7.3.1	Worst-Case Bound	77
7.3.2	Statistical Analysis	78
7.3.3	Monte-Carlo Simulation	78
7.4	Scalability	78
7.4.1	Channel deviations	79
7.4.2	Effect of mutual coupling	83
7.5	Summary	87
8	Conclusion and Outlook	89
	Bibliography	92

1 Introduction

1.1 Context

Connectivity and mobility are two subjects of most concern in modern community. Thereby, internet access is nowadays indispensable not only in business but also in personal life as it is crucially required in many applications such as websites, e-mail, file sharing, and video call. As presented in the report of BITKOM ¹ in 2015, three out of four EU citizens aged between 16 and 74 year-old (76%) use Internet at least once per week. Additionally, the trend of Internet usage per mobile devices is recognizably rising. More than half of EU citizens according to BITKOM use Internet via smart phones whilst one-third uses mobile computers such as laptops, notebooks, and tablets. Moreover, a steady growth of broadband services is also observed. In 2015, 96% of the companies in Germany had broadband Internet access whilst this number is 88% for households. The estimated data traffic volume in Fig. 1.1 for the period from 2014 to 2019 presented in Cisco Visual Networking Index [1] indicates a substantial rise. Compared to nearly 30% increase of the fixed network, the usage of the mobile service shows growth of more than 65% over five years. This fact demonstrates a potential leap of mobile broadband services in the near future. As an important part of the modern communication services, high demand of satellite communications is also expected, especially in regions with poor infrastructure.

Digital Video Broadcasting- Satellite (DVB-S) is one of the well-known satellite services nowadays. The video signals are broadcast via satellites such as those from Astra ², or Eutelsat ³ from 10.7 GHz to 12.75 GHz (Downlink) and from 14 GHz to 17.5 GHz (Uplink) at Ku band. Additionally, satellites at C- and L-band [2] are also used for radio and navigation services. However, the capacity offered by these satellites is not enough for multimedia applications. Hence, communication systems at higher frequency bands, e.g., Ka band, are proposed to achieve higher bandwidth.

For example, those systems were suggested for the services on mobile platforms such as aircrafts or ships and examined intensively in the last ten years. High directivity and tracking ability are two main desired characteristics of these communication systems. By the way of tracking, namely mechanical and electronic, two kinds of systems are classified. The first one is based on reflector

¹Die Bundesverband Informationswirtschaft, Telekommunikation und neue Medien e.V. Website: <https://www.bitkom.org/Marktdaten/Konsum-Nutzungsverhalten/Facts-zu-Internet.html>. 2015

²Astra: <https://www.astra.de>

³Eutelsat: <https://www.eutelsat.com/de/Dienste/tv-direktempfang/programme-frequenzen.html>, 2015

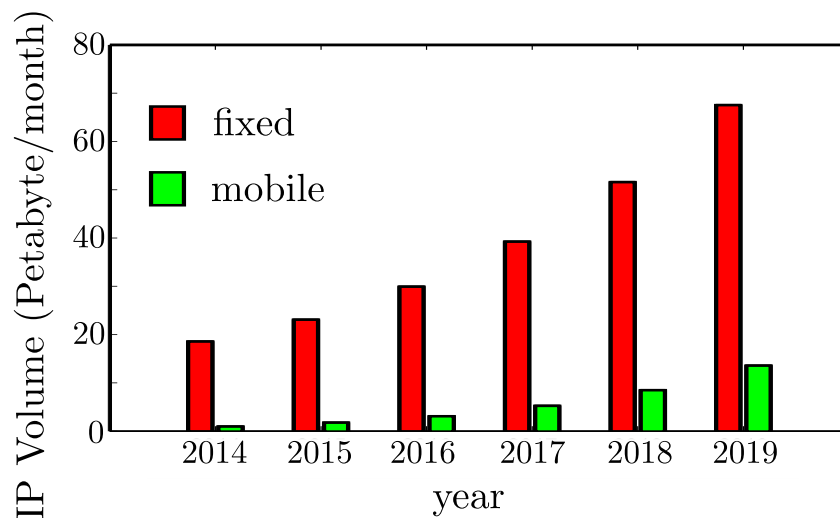


Figure 1.1: Traffic volume of the Global consumer Internet video (the values since 2016 are estimated)

antennas [3], [4]. In this approach, the direction of the main beam can be steered and error caused by the movement of the platform can be compensated by rotating the reflector mechanically.

The beam forming can be performed much faster in the second approach, which relies on phased arrays. Additionally, nulls in radiation pattern can be located at desired positions by configuring the system electronically, hence, interferences can be suppressed. The electronically reconfigurable antenna system can be divided further into two kinds of system implementations, namely a phased array and a Digital Beam Forming system (DBF).

In the phased array receiver system, each channel is equipped with an amplifier and a phase shifter. In this case, the phase and the amplitude of the signal can be weighted directly to form a sum pattern in the direction of interest. Because the beam pattern is constructed in an analogue way, phased array technique is also called Analogue Beam Forming (ABF).

On the other hand, in a DBF system each channel is provided with an A/D-converter instead of a phase shifter. The beam pattern is then constructed digitally by a Digital Signal Processing (DSP) board. Due to its capability of accessing all received signals, and not only the sum signal, the DBF system offers the most flexibility in the signal processing compared to the two other system types mentioned above. This approach offers some other functions than suppression of interferences, including but not limited to multi-beam operation, adaptive beam steering or high resolution processing techniques.

The aim of implementing a scalable satellite communication system at Ka band efficiently in term of cost is one of the main themes of the projects SANTANA I, II, III (Smart Antenna Terminal) [5], [6] and SAMOA (Smart terminal Antenna for Mobile Applications) [7], which were funded by the German Aerospace Center DLR (Deutsches Zentrum für Luft- und Raumfahrt) on behalf of the Ger-

man Federal Ministry of Economics and Technology BMWi (Bundesministerium für Wirtschaft und Technologie). There are two main challenges addressed in these projects, namely high directivity or large number of channels, as well as high integration density.

The first challenge bases on the energy balance calculation [8] for a communication distance between a mobile platform on the earth and a geostationary satellite. As a result, at least 1000 channels are required in a phased array system in order to perform the transmit- and receive functions. Thus, the circuitry of such a system is complex and hardware cost is significant.

Moreover, the second challenge stems from the requirement of a $\lambda/2$ -grid (λ : free space signal wavelength) to avoid grating lobes in the beam pattern of the system. The distance between antenna elements of a Ka-band system is only 5 mm (at 30 GHz for the Uplink) and 7.5 mm (at 20 GHz for the Downlink). This means that the integration concept of a C- or L-band system cannot be simply scaled, but that it has to be completely redesigned not only to fit all components into the defined area of $(\lambda/2) \times (\lambda/2)$ but also to minimize the cross-talk between the channels.

Besides the implementation, other related aspects of the communication system such as the development of calibration concept are also examined in these projects. This defines the frame of the present work.

1.2 Formulation of the Problem

Calibration is an important task, in which all errors and uncertainties of the system are identified and compensated to guarantee the desired system performance.

Regarding the first challenge in the system design at Ka band, an enormous number of active and passive components has to be integrated. Besides fabrication tolerances, also constraints in the design procedure due to the limited available space lead to variations in the signal paths. As a result, amplitudes and phases of the channels are distributed statistically in contrast to the ideal assumptions. Additionally, cross-talk is difficult to be avoided, especially in a communication system with high integration density of components and despite the effort to minimize it as much as possible in the design procedure. Based on these two main problems, the communication system can operate properly only after a calibration procedure.

Whilst systematic errors of the system can be characterized and corrected by means of measurements performed in an anechoic chamber before operation, uncertainties caused by environmental changes as well as system instability during operation have to be compensated by a periodical on-line procedure. This means, that the calibration system has to be autonomous and integrated into the receiver array.

Many calibration approaches have been proposed in the literature not only for DBF systems, but also for ABF phased arrays. Due to similar architectures, the calibration concept used in a DBF system can be extended to be applied in the case of ABF and vice versa. However, more errors can be found

in a DBF system due to its hardware complexity. Its advantage of accessing all channel signals eases the calibration task and offers more flexibility for the signal processing algorithms. So, both kinds of approaches are reviewed in this work.

Internal and external approaches are the two main classes of on-line calibration concepts regarding the way of feeding the calibration signals. In the first approach, integrated couplers behind the antenna are used commonly to couple calibration signals into the channels of a receiver system or to sample a small part of the transmitted signals in the case of transmitter arrays. The existence of integrated couplers and a distribution network of the internal calibration system increases immensely the integration density. On the other side, the external approach is more suitable for large-size arrays. Calibration probes are placed outside the array to detect the electromagnetic field radiated by the transmitters or to radiate calibration signals into the receivers. By this way, the calibration system is constructed outside the main system, and thus, the integration density is nearly unaltered.

Three ways of implementing calibration probes were proposed in literature. The first approach is to distribute the calibration system into the main system. Due to the sparsity of the calibration elements, the average integration density does not increase much. The calibration element has to be either an integrated transmit/ receive module [9], [10] or a transmit module in a receiver array (or vice versa) [11]. This set-up, however, leads to disturbances in the radiation pattern of the main array in operation.

Secondly, an on-board probe can be constructed in the broad-side of the array [12], [13], [14]. Whilst this set-up is supposed to get the highest calibration accuracy, solid mechanical probe holders are necessary, which is rather complex to build on an aircraft. Additionally, due to the appearance of the extra mechanical holders and probes, the pattern of the main system operation can be modified and disturbed.

The last one is the placement of the probes at the off-side of the array as proposed in [15]. This construction demonstrates maximum decoupling between the calibration and main operation of the system. Thus, the on-board calibration system with external probes at the off-side is examined and developed in this work.

1.3 Thesis Topic and Outline

The topic of this thesis in the context of the SAMOA project is the further development and analysis of external on-line calibration procedures for DBF receiver arrays. Due to the high integration density of the receiver system and hence the limited space for the calibration system, the external set-up proposed in [15] is applied and developed further. In this work, not only the autonomous calibration procedure for channel deviations is deepened to achieve better accuracy, but also the decoupling algorithm is improved to take the mutual coupling into account. Moreover, experiments are performed for a small-size array at 20 GHz to demonstrate the usefulness of the proposed concept. Last but not

least, the extension and the scalability of the calibration system for large-size arrays are discussed by means of tolerance analysis.

Three main contributions of this work can be highlighted here: (1) the analytical modeling procedure of the probe-receiver coupling, (2) the development of a decoupling procedure to consider not only channel fluctuations but also the cross-talk in the system and (3) the discussion about the complexity and the scalability of the calibration procedure for a given receiver array.

The remainder of this work is structured as follows:

In Chapter 2, all important characteristics of antenna systems such as gain, directivity, and polarization are highlighted. Furthermore, the receiver architecture is discussed and a simplified system used in the experiments is presented. Last but not least, the impact of channel errors on the system performance is also reviewed in this chapter.

Secondly, the error sources appearing in a DBF receiver system are identified and discussed in Chapter 3. Then, the calibration concepts known from literatures are briefly reported. Additionally, advantages and disadvantages of these approaches are also highlighted and discussed in the context of the application scenario. As will be shown, despite some minor drawbacks, the external calibration concept is chosen in this work because of its implementation simplicity and flexibility for medium to large arrays.

The focus of this work on the calibration of channel deviations in a receiver array is discussed in Chapter 4. As the starting point of the calibration procedure, the characteristics of two implemented calibration probes are considered. Based on system theory, an analytical model of the probe-receiver coupling is developed to improve the calibration accuracy, but still keep the simulation complexity as small as possible. Furthermore, the calibration procedure with various averaging methods is also analyzed and its usefulness is then verified with a two-step simulation procedure.

The joint calibration of channel fluctuations and mutual coupling is the theme of Chapter 5. Firstly, the description of the coupling matrix is reviewed mathematically and a simplified version is proposed to reduce the computational complexity. Secondly, three decoupling algorithms, namely Least-Square and its extension by means of a Principle Component Analysis as well as with Multiple Reference Receivers is considered. At this end, the proposed signal processing concepts are validated by simulation.

Chapter 6 reports experimental results for various system architectures. Because of its simplicity and flexibility of fabrication, a printed probe is first used in the experiments with a three-patch antenna array. The demand for high SNR calibration measurements as well as the necessity of a better model for the probe-receiver coupling are demonstrated. As an improvement, a coaxial probe is then used in the other experiments with a linear array and a planar array. Various networks are connected to the passive antenna array to represent different architectures of the receiver array. By analyzing the results, the applicability of the proposed calibration procedures is discussed for various situations.

As a last point of this work, a tolerance analysis is performed in Chapter 7. In case of small arrays, a

theoretical analysis based on linear approximation and uncertainty propagation is performed. On the other hand, a Monte-Carlo simulation is applied in case of large array to illustrate the robustness of the decoupling algorithm against fabrication uncertainty and system noise. As a result, the scalability of the calibration system for a large-size receiver array is also demonstrated.

Finally, a summary of this work is reported in Chapter 8.

2 Antenna Basics

In this chapter, we review briefly several aspects of antenna theory, which are relevant to the design procedure of the external calibration concept.

2.1 Antenna Parameters

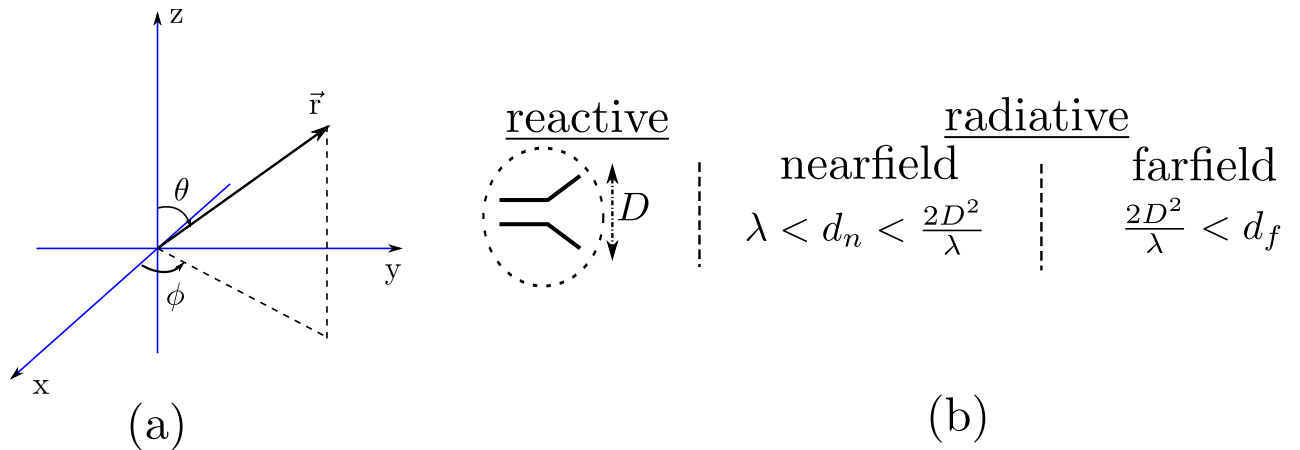


Figure 2.1: (a) Spherical coordinate system and (b) three observation regions: reactive (non-radiative), near-field and far-field radiative regions.

An antenna is a reciprocal structure and acts like a spatial filter, which converts electromagnetic waves radiated in free space into guided waves in a transmission structure or vice versa. Its behavior at a point in space is described by a Green's function in spherical coordinates as depicted in Fig. 2.1(a). Depending on the distance d_n or d_f to the observation point, this characteristic Green's function can be classified into three regions, namely a reactive (non-radiative), a near-field (Fresnel) and a far-field radiative (Fraunhofer) region which are illustrated in Fig. 2.1(b). Due to the large distance to satellites, the far-field condition $d_f > \frac{2D^2}{\lambda}$ is always satisfied with λ and D being the signal wavelength and the antenna aperture, respectively. Thus, the Green's function is determined as

$$E = G(r) = \frac{e^{-j2\pi r/\lambda}}{4\pi r} P_e(\theta, \phi). \quad (2.1)$$

Here, P_e , a function of only two angular variables θ and ϕ , is defined as the radiation pattern of the antenna. If P_e is constant in all directions, we have an omni-directional antenna. If not, the antenna is said to be directive. The directivity is defined as

$$Dir = \frac{P_{e,max}}{P_{e,omi}} = \frac{4\pi P_{e,max}}{\int_{\theta} \int_{\phi} P_e(\theta, \phi) d\phi \cdot d\theta}. \quad (2.2)$$

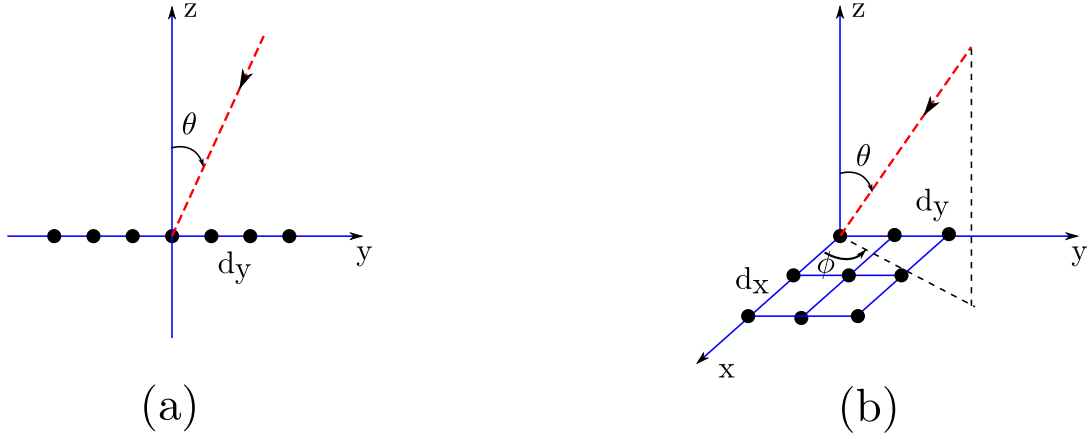


Figure 2.2: (a) A 7-element linear array and (b) a 3x3-element planar array.

In order to improve the performance of receiver systems, a group of antennas, which is distributed in a defined configuration such as linear or planar as depicted in Fig. 2.2(a) and Fig. 2.2(b), respectively, is operated coherently. If the antennas are identical, the array factor of a linear array is calculated as

$$AF = \sum_{n=1}^N W_n \exp\left(-j \frac{2\pi n d_y \sin(\theta)}{\lambda}\right), \quad (2.3)$$

and that of a planar array as

$$AF = \sum_{n_1=1}^{N_x} \sum_{n_2=1}^{N_y} W_{n_1 n_2} \exp\left(-j \frac{2\pi n_2 d_y \sin(\theta) \sin(\phi)}{\lambda}\right) \exp\left(-j \frac{2\pi n_1 d_x \sin(\theta) \cos(\phi)}{\lambda}\right). \quad (2.4)$$

Here, W_n and $W_{n_1 n_2}$ are complex values denoting the weighting factor of channel n and (n_1, n_2) , respectively. The radiation pattern of the whole array is determined as

$$P_a(\theta, \phi) = P_e(\theta, \phi) \cdot AF. \quad (2.5)$$

In addition, the Half-Power-Beam-Width (HPBW) of the array is defined in [8] as the angle interval between two points of half-power-intensity (-3 dB) with respect to the maximum of the main beam as depicted in Fig. 2.3. Following [16], the 3 dB- beam width of a linear phased array with uniform amplitude distribution can be estimated as

$$HPBW = \arcsin\left[\sin(\theta_0) + 0.443 \frac{\lambda}{L}\right] - \arcsin\left[\sin(\theta_0) - 0.443 \frac{\lambda}{L}\right], \quad (2.6)$$

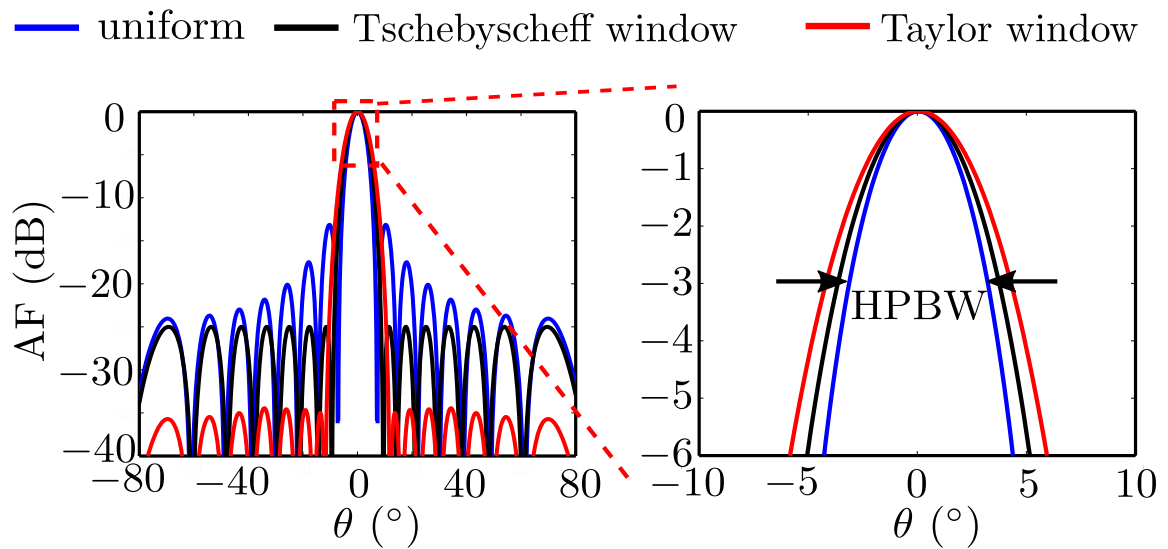


Figure 2.3: Array factor and HPBW of a linear array with 16 elements with three different window functions: uniform weighting (side-lobe of -13 dB), Tschebyscheff function [17] (side-lobe of -25 dB) and Taylor function [18] (side-lobe of -35 dB).

with θ_0 and L being direction of the main beam as well as length of the array, respectively.

Furthermore, the side-lobes in the radiation pattern can be reduced by applying window function to the array weighting factor A_n . As an example, the radiation patterns for three window functions, namely uniform, Tschebyscheff [17] and Taylor [18], are shown in Fig 2.3. As a trade-off, the HPBW increases with decreasing side-lobe level.

Besides, in order to avoid the repetition of the main beam (grating lobes) in the Field-Of-View (FOV)

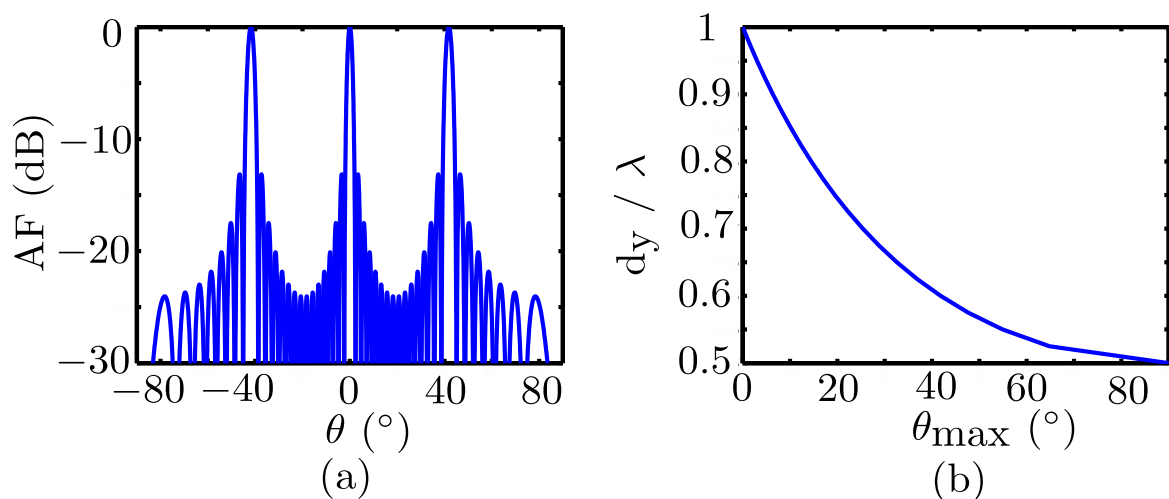


Figure 2.4: (a) Radiation pattern of a 16-element linear array with element distance $d_y = 1.5\lambda$ and (b) element distance versus maximum scanning angle.

of the phased array, the Nyquist sampling criterion needs to be fulfilled. As an example, two grating lobes are observed in the radiation pattern of an array with an element spacing of 1.5λ as shown in Fig. 2.4(a). Following [19], the maximum distance d_y between array elements is estimated as

$$d_y = \frac{1}{1 + |\sin(\theta_{\max})|}, \quad (2.7)$$

with θ_{\max} being the maximum angle of the scanning range. As depicted in Fig. 2.4(b), a scanning range up to 60° requires the element distance to be smaller than 0.54λ .

2.2 Polarization

The polarization is a characteristic of a transversal electromagnetic wave, which shows the trace described by the tip of the electric field over time. We differentiate between linear, circular, and elliptical polarization according to the shape of the trace. Additionally, the axial ratio (AR)

$$AR = \frac{\sqrt{E_x^2 + E_y^2 + \sqrt{E_x^4 + E_y^4 + 2E_x^2E_y^2 \cos(2\varphi_x - 2\varphi_y)}}}{\sqrt{E_x^2 + E_y^2 - \sqrt{E_x^4 + E_y^4 + 2E_x^2E_y^2 \cos(2\varphi_x - 2\varphi_y)}}} \quad (2.8)$$

is used to classify the polarization of a signal propagating in \vec{z} -direction.

The signal is circularly polarized if $AR = 0\text{dB}$, whilst it is linearly polarized for $AR \rightarrow \infty$. In all other cases, we have elliptical polarization. Lastly, the right (left)-handed circular polarization is defined by the clockwise (counter-clockwise) rotation direction of the vector. As an example, a right-handed circular-polarized (RHCP) signal is plotted in Fig. 2.5.

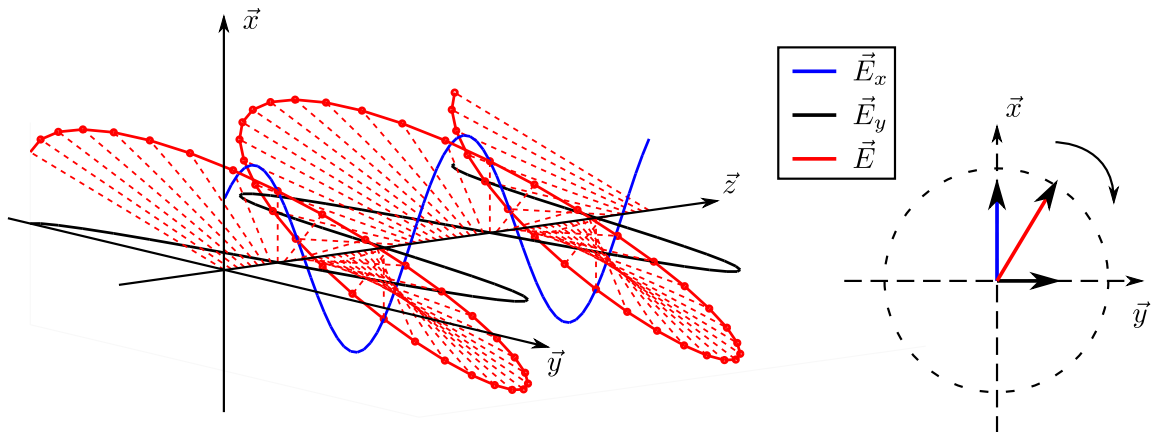
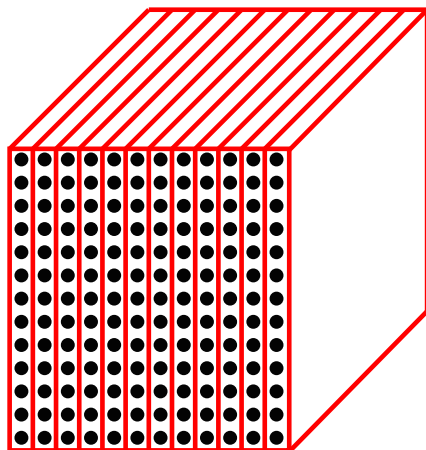
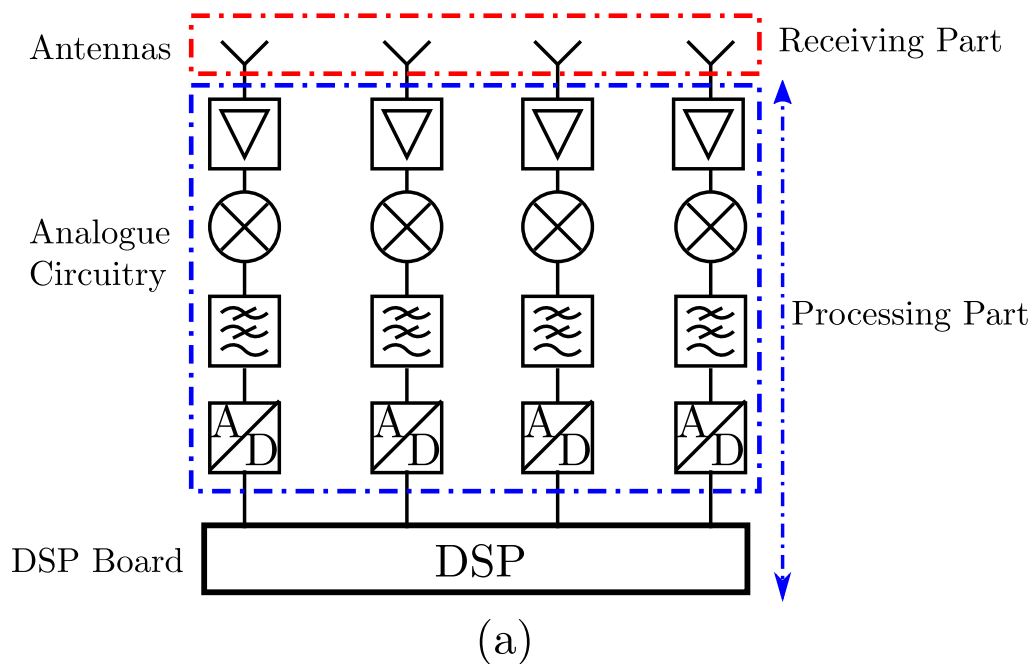


Figure 2.5: Circular polarisation.

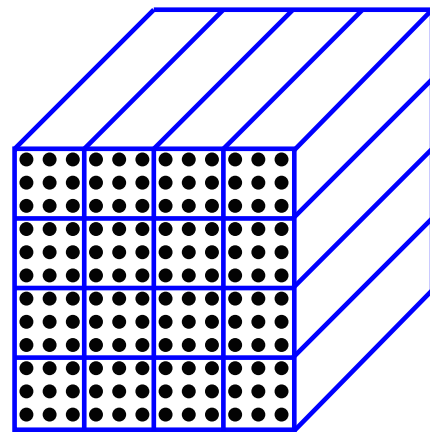
2.3 Receiver System

In this work, we discuss calibration concepts for receiver systems with digital beam forming. As the main system, the receiver is composed of an antenna array (signal receiving part) which connects to the active components of the signal processing part such as low noise amplifiers, bandpass filters, and mixers. The received analogue high frequency signal is first amplified and then down-converted to the baseband signal before it is converted into the digital domain and processed by in a DSP. The



brick architecture

(b)



tile architecture

(c)

Figure 2.6: Architecture of receiver arrays: (a) architecture of a DBF array, (b) brick and (c) tile architecture.

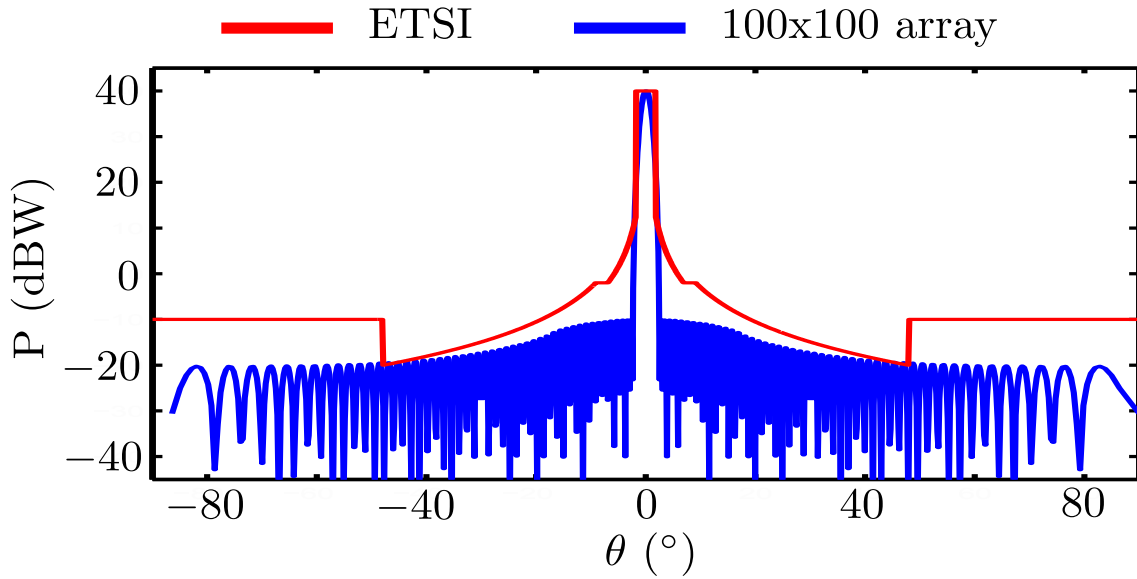


Figure 2.7: EIRP requirements for satellite communication systems at Ka-band and power distribution of a 100x100 array with amplitude tapering.

architecture of the receiver array is sketched in Fig 2.6(a).

Additionally, the array parameters such as the 3dB-beam-width and the side-lobe level (the ratio between the side-lobe with respect to the main-lobe) follow the standards given by the European Telecommunications Standards Institute (ETSI) [20] and illustrated in Fig. 2.7. They require not only a huge number of array elements (e.g. 100x100) for the very narrow beamwidth but also an amplitude taper (e.g. Taylor-function [8]) to satisfy the very low side-lobe level.

Therefore, the modular approach is proposed and developed as a solution to implement a large-size array. Two basic concepts, namely the brick and the tile architectures [21, 22], are illustrated in Fig 2.6(b) and (c), respectively.

In the brick architecture, several linear sub-arrays, the orientation of which is parallel to the vertical direction, are stacked together in the horizontal axis [23]. In contrast, the antennas, different RF devices and control units are mounted on various layers parallel to the aperture plane of the system in the tile architecture. More details about system architectures can for instance be found in [24, 25]. Additionally, an array can be constructed from various similar smaller sub-arrays. The size of a sub-array and the design procedure can be optimized to achieve the highest flexibility and adaptivity as well as the lowest effort for various systems with different requirements and applications. A discussion is given in [26].

On the other hand, planar arrays with patches [27] or with SIW (Substrate Integrated Waveguide) antennas [28] have been proposed and examined to transmit or receive the far-field signals with circular polarization. In order to improve the circular polarization performance of the whole array, sequential rotation can also be applied as described in [29]. Thereby, the output signals shows a

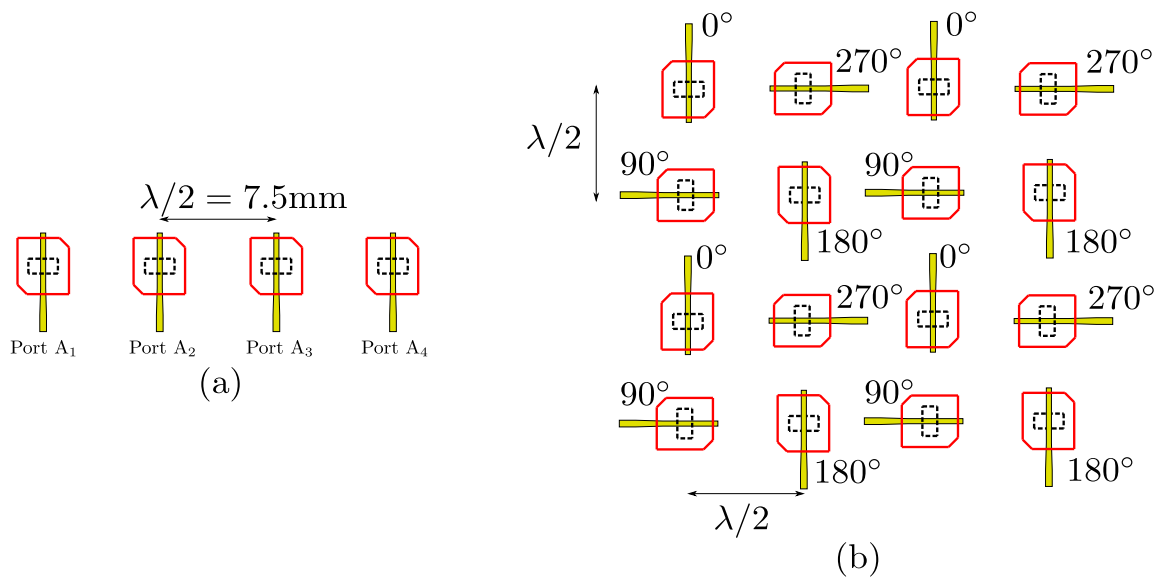


Figure 2.8: Experimental arrays: (a) linear array and (b) sequentially rotated planar array

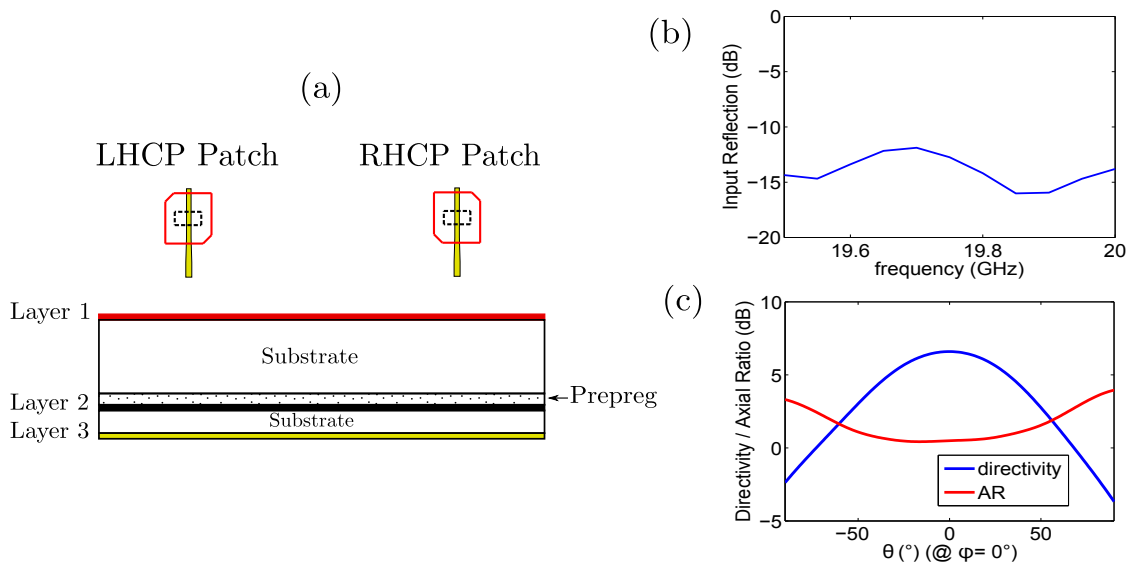


Figure 2.9: Patch antenna: (a) multilayer structure, (b) input reflection, and (c) directivity as well as axial ratio of a patch simulated in CST.

sequential phase change of 90° .

Because of their low cost and simple fabrication, linear and planar arrays of patch antennas as depicted in Fig. 2.8 are used in the experiments. The patches are aperture coupled patch antenna. They are receiver elements at Ka band (19.7-20.2 GHz), and are implemented in a multilayer structure as shown in Fig. 2.9(a). In addition, two patch corners are truncated to realize circular polarization.

As depicted in Fig. 2.9(b), an input reflection below -10 dB over the whole bandwidth is observed for the patch antennas. Additionally, the patch directivity as well as the axial ratio of the receiver

antenna can be seen in Fig. 2.9(c). The 3dB-beamwidth reaches only $\Phi = \pm 50^\circ$. Thus, only a very small amount of signal radiation can be received in the patch plane. This observation shows a possibility of placing the on-board probes of the calibration system at this position to achieve high decoupling and minimize disturbance of the receiver operation [15].

Furthermore, side-lobes are observed in the radiation pattern of the array. The side-lobe level defined as the maximum value of the side-lobes is required to be very low (normally -30dB) according to the ETSI norm. In addition, the element spacing in both x- and y- direction is roughly $\lambda/2$ ($\approx 7.5\text{mm}$ at 20GHz) to avoid grating lobes.

2.4 Tolerance effects

In a large array, a statistical distribution is observed for the gains and the phases of the receiver channels due to fabrication tolerance. If a system with high performance is desired, fabrication technology with high quality should be maintained, and small errors can be assumed. There are intensive examinations of tolerance effects in literature. The readers are referred to [16, 30–32] for more details.

In this section, we review briefly the main results, which are used in the following chapters. Due to (2.3), the ideal beam B_{ideal} in a certain direction θ of an array with amplitude tapering A_n is determined as:

$$B_{\text{ideal}}(\theta) = \sum_{n=1}^N A_n \exp\left(-j \frac{2\pi n d_y \sin(\theta)}{\lambda}\right). \quad (2.9)$$

By extending (2.3), the fabrication errors are taken into account. The actual beam B_{act} is calculated as

$$B_{\text{act}}(\theta) = \sum_{n=1}^N A_n (1 + \delta_{A,n}) \exp(j\delta_{\phi,n}) \exp\left(-j \frac{2\pi n d_y \sin(\theta)}{\lambda}\right). \quad (2.10)$$

Here, the distributions of the relative amplitude deviation $\delta_{A,n}$ and the phase error $\delta_{\phi,n}$ are assumed to be Gaussian with zero means as well as with standard deviations of σ_A and σ_ϕ , respectively. This means:

$$\delta_A \sim \mathcal{N}(0, \sigma_A^2), \quad (2.11)$$

$$\delta_\phi \sim \mathcal{N}(0, \sigma_\phi^2). \quad (2.12)$$

In addition, in order to examine only the tolerance effects on the side-lobe level of the array, the amplitude tapering is normalized as

$$\sum_{n=1}^N A_n = 1 \quad (2.13)$$

Based on the central limit theorem, the distribution of the actual beam error $\Delta B = B_{\text{act}} - B_{\text{ideal}}$ in a certain direction is a complex Gaussian distribution

$$\Delta B \sim \mathcal{CN}(0, \sigma_B^2), \quad (2.14)$$

$$\text{Re}\{\Delta B\} \sim \mathcal{N}\left(0, \frac{\sigma_B^2}{2}\right), \quad (2.15)$$

$$\text{Im}\{\Delta B\} \sim \mathcal{N}\left(0, \frac{\sigma_B^2}{2}\right), \quad (2.16)$$

with the standard deviation σ_B

$$\sigma_B^2 = \frac{1}{2} (\sigma_A^2 + \sigma_\phi^2) \sum_{n=1}^N A_n^2. \quad (2.17)$$

As a result, a Rayleigh- and a Rice distribution are obtained for the magnitudes of the beam (beam: complex field pattern) error ΔB and the actual beam B_{act} , respectively, as

$$\|\Delta B\| \sim \text{Rayleigh}\left(0, \frac{\sigma_B}{\sqrt{2}}\right), \quad (2.18)$$

$$\|B_{\text{act}}\| \sim \text{Rice}\left(B_{\text{ideal}}, \frac{\sigma_B}{\sqrt{2}}\right). \quad (2.19)$$

The cumulative probability distribution $\mathcal{P}(B_{\text{act}})$ of the actual beam can be calculated as

$$\mathcal{P}(B_{\text{act}}) = \int_{-\infty}^{\|B_{\text{act}}\|} \text{Rice}\left(B_{\text{ideal}}, \frac{\sigma_B}{\sqrt{2}}\right) dB = 1 - Q_{M=1}\left(\frac{B_{\text{ideal}}}{\sigma_B}, \frac{B_{\text{act}}}{\sigma_B}\right). \quad (2.20)$$

Here, Q_M is the Marcum Q-function which is defined in [33] as

$$Q_M(a, b) = \int_b^\infty x(x/a)^{M-1} \exp\left(-\frac{x^2 + a^2}{2}\right) I_{M-1}(ax) dx, \quad (2.21)$$

with I_{M-1} being the modified Bessel function of order $M - 1$.

As a consequence, the Peak Side-lobe Level (PSL) $B_{\text{threshold}}$ can be defined for a given cumulative probability F with

$$\mathcal{P}(B_{\text{act}} < B_{\text{threshold}}) = F. \quad (2.22)$$

As an example, the pattern of the PSL $B_{\text{threshold}}$ is determined for a 16-element linear array with $\sigma_A = 1$ dB and $\sigma_\phi = 3^\circ$. As depicted in Fig. 2.10(a), the real disturbed beam pattern is below the calculated PSL pattern (with a possibility of 95%). Furthermore, (2.22) is illustrated by the phasor representations of the beam in Fig. 2.10(b) at a certain direction angle θ . Although the PSL $B_{\text{threshold}}$ has to be actually calculated for each angle θ , it fluctuates slightly in the side-lobe region. Hence, we consider

$$\text{PSL} = \max_{\theta \leq \theta_1 \& \theta \geq \theta_2} (B_{\text{threshold}}(\theta)), \quad (2.23)$$

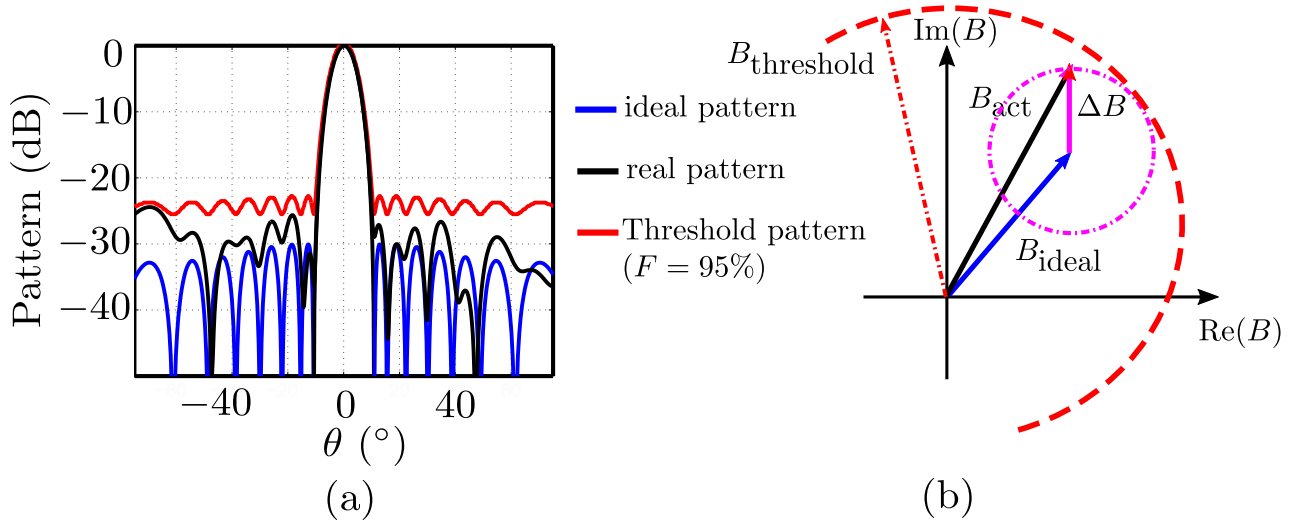


Figure 2.10: Example of a 16-element linear array: (a) the ideal-, the real disturbed beam pattern, and the PSL pattern ($F = 95\%$) with $\sigma_A = 1$ dB and $\sigma_\Phi = 3^\circ$ as well as (b) their phasor representations at a certain direction angle θ .

in further discussions. Here, θ_1 and θ_2 are the angular positions of the nulls beside the main beam. In order to take the tolerance effects into account, the amplitude tapering has to be chosen so that $B_{\text{ideal}} < \text{PSL}$ with PSL being the desired side-lobe level for a given probability F (e.g., $F = 95\%$ in this work).

A similar examination is applied to determine the effect of the mutual coupling as derived in [32]. If the channel deviations are compensated and only mutual coupling between adjacent channels is taken into account, the beam pattern of a linear array can be written as

$$\begin{aligned}
 AF &= \sum_{n=1}^N A_n \exp\left(-j \frac{2\pi n d_y \sin(\theta)}{\lambda}\right) \\
 &+ \sum_{n=1}^{N-1} \beta_{n,n+1} A_n A_{n+1} \exp\left(-j \frac{2\pi d_y \sin(\theta)}{\lambda}\right) \\
 &+ \sum_{n=2}^N \beta_{n,n-1} A_n A_{n-1} \exp\left(-j \frac{2\pi d_y \sin(\theta)}{\lambda}\right). \tag{2.24}
 \end{aligned}$$

with $\beta_{n,m}$ being the mutual coupling between the n^{th} and the m^{th} channel. In practice, the coupling β_{mn} , which generally stays below -10 dB, can be considered as a small disturbance of the beam pattern and modeled as

$$\beta_{nm} = \beta \exp(j\varphi) \tag{2.25}$$

with β being the average coupling level and φ denoting a statistical variable with uniform distribution

$$\varphi \sim \mathcal{U}(-\pi, \pi). \tag{2.26}$$

As a result, the distribution of the actual beam pattern B_{act} is again a complex Gaussian distribution with a variance

$$\sigma_B^2 = \beta^2 \left[2 \sum_{n=1}^N A_n^2 - (A_1^2 + A_N^2) \right]. \quad (2.27)$$

If a receiver array is examined and mutual coupling between a channel with four adjacent channels is taken into account, (2.27) is extended to

$$\sigma_B^2 = \beta^2 \left[4 \sum_{m=1}^N \sum_{n=1}^N A_{mn}^2 - 2 (A_{11}^2 + A_{1N}^2 + A_{N1}^2 + A_{NN}^2) \right]. \quad (2.28)$$

Then, the peak side-lobe level $B_{\text{threshold}}$ as well as the suitable channel tapering can be calculated as mentioned above to fulfill the design requirements.

In addition, the uncertainty Δ_{DOA} of the main beam direction DOA (Direction Of Arrival) of the receiver array is another aspect. As shown in [16], the variance σ_{DOA} of the direction uncertainty of a linear receiver array with uniform weighting can be determined as:

$$\sigma_{\text{DOA}}^2 = \frac{12}{N^3} \sigma_{\Phi}^2 \quad (2.29)$$

with N being the number of the array elements. That means, the direction error is inversely proportional to N^3 and is negligible in case of large arrays. Thus, it is not examined in this work.

3 Calibration Concept

In this chapter, the calibration concept of a DBF receiver phased array is discussed. Firstly, the error sources are identified. Then, various calibration concepts proposed in the literature are reviewed and their advantages and disadvantages in terms of accuracy and complexity are highlighted. Lastly, the concept of the external calibration and its set-up are presented and shown to be suitable for large phased array systems which is the aim in the present context.

3.1 Error Sources

Due to its complex system structure, there are multiple error sources in a DBF receiver system. In order to guarantee the desired performances of the communication system, these errors need to be characterized and corrected during the operation of the system. This is the goal of a calibration procedure.

As proven in [16, 30], the gain fluctuates only slightly, whilst fabrication tolerances have a strong impact on the side-lobe level of the array. On the other side, the controllability of the array pattern can be examined through the peak side-lobe level with a cumulative probability of 95% as explained in Chapter 2. Relating to the ETSI standards for satellite communications [20], we consider a peak side-lobe level PSL_{desired} of -35 dB in this work.

From a practical point of view, we divide the errors into two main groups with respect to their effects:

- (1) Degradation of the radiation pattern due to fluctuations of the channel parameters such as gain and phase.
- (2) Degradation of the radiation pattern due to mutual coupling between the channels.

3.1.1 Channel fluctuations

Each active component in the receiver channel is itself a complex sub-device with DC supplied sources and transistors. Their behavior is influenced by the environmental conditions such as temperature changes or fluctuating supply voltages. Furthermore, deviations between channels exist due to the fabrication tolerance.

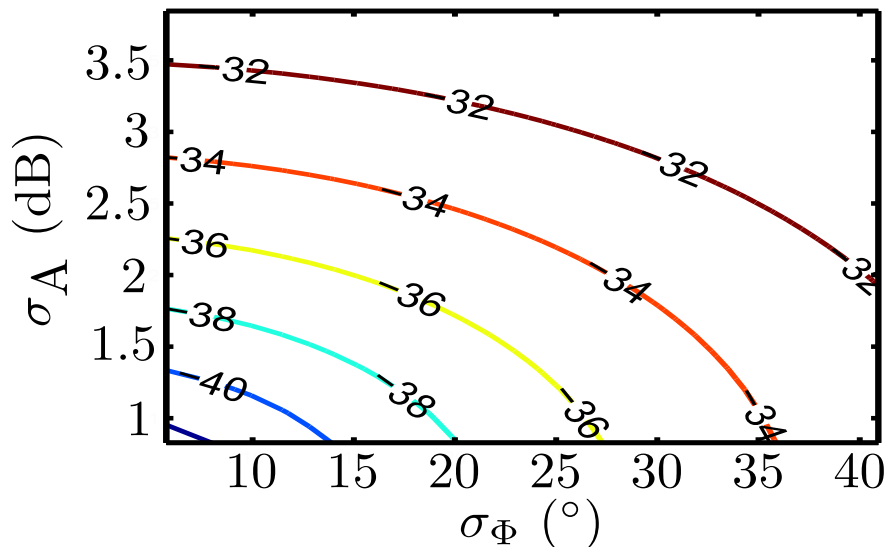


Figure 3.1: 64x64 planar array: peak side-lobe level (in dB) with a probability of 95% as a function of the deviation of the amplitude σ_A and the phase σ_Φ of the channel factors.

As depicted in Fig. 3.1, the peak side-lobe level occurring with a 95% probability is calculated for a 64x64 planar array as a function of the deviation of the amplitude σ_A and the phase σ_Φ of the channel factors based on Chapter 2.4. A side-lobe level below -35 dB is achieved only if the deviation of the amplitude (the phase) of the channel factors is lower than $\sigma_A = 2.5$ dB ($\sigma_\Phi = 30^\circ$). Furthermore, if errors of both amplitude and phase are taken into account and their variances are assumed to be similar to each other, σ_A and σ_Φ are 1.8 dB and 20° , respectively.

3.1.2 Mutual Coupling

The second main error source is the mutual coupling between the receiver channels. In real applications, large systems with multiple functions such as multiple beam-forming or integration of transmit/receive modules need to be built up within a grid of roughly $\lambda/2$. Hence, a high integration density is desired.

Due to the limited space in a compact system, cross-talk between channels may appear at each stage of the signal processing part in the receiver chain, namely from the antenna structure down to the intermediate frequency stage. This is a routing problem, which should be minimized as much as possible in the system design. Furthermore, the possibility of cross-talk existence depends strongly on the distance between two channels as well as on the system architecture.

On the other side, the mechanism of mutual coupling existing between the antennas in the signal receiving part, being different from the cross-talk effect in the signal processing unit, relates to deformations of the electromagnetic field at the patches. This effect is examined firstly in [34] and

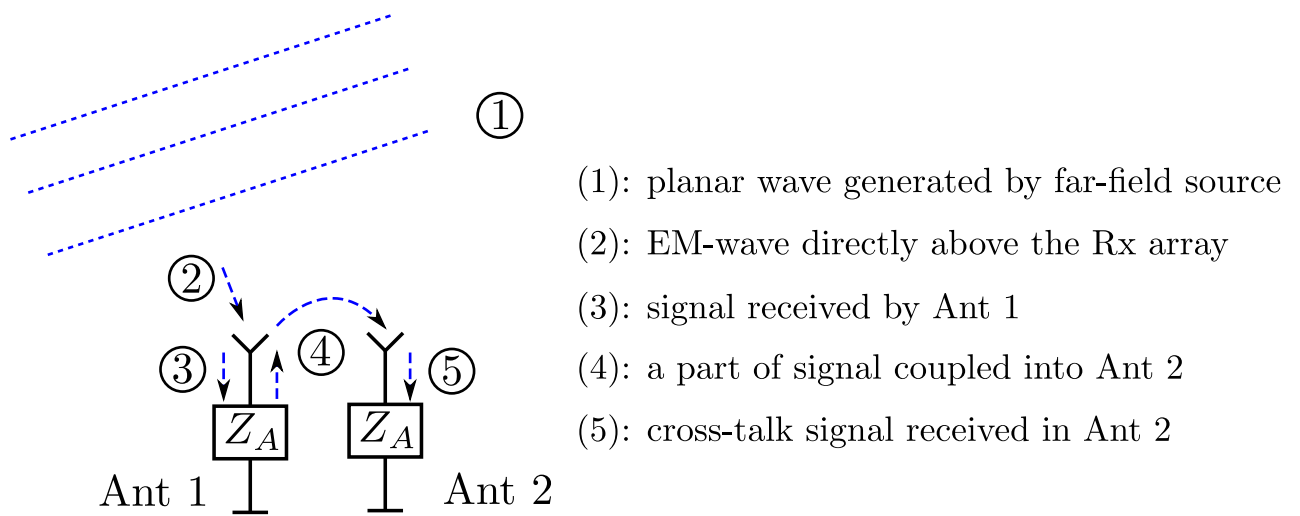


Figure 3.2: Mutual coupling mechanism in an array: five-step diagram

can be reviewed by means of a five-step diagram as depicted in Fig. 3.2.

First, a plane wave generated by a far-field source is detected by the antennas (here: two) of a receiver array. Secondly, due to the existence of antenna 1, the electromagnetic field in front of antenna 2 is deformed and different from that of an isolated antenna if the distance between two antennas is below a certain threshold. In comparison with linearly polarized antennas, the influence of this coupling mechanism is greater in patch arrays with circular polarization because of their asymmetry. Besides, if mismatch exists at the interface between the passive and the active subsystem, a part of the signal received by antenna 1 is reflected, re-radiated into free space, and cross-coupled into

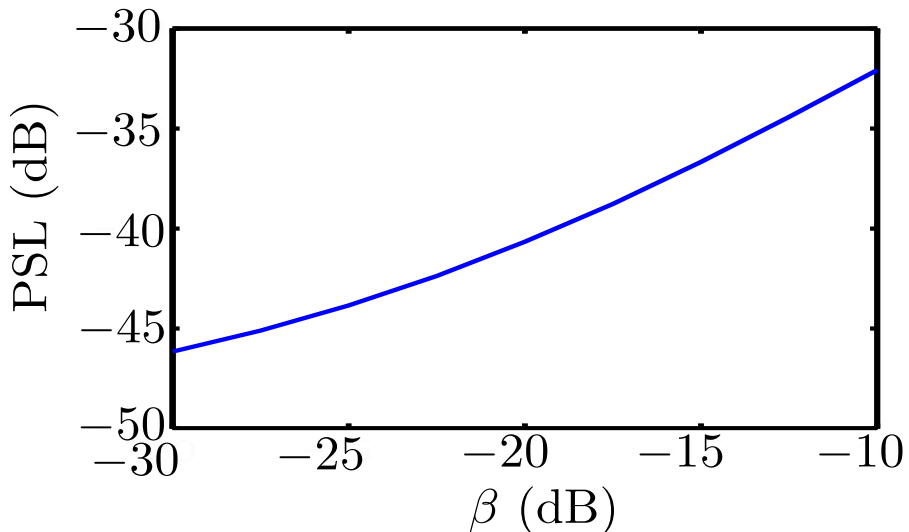


Figure 3.3: 64x64 planar array: peak side-lobe level (in dB) with a probability of 95% as a function of uncalibrated coupling factor.

antenna 2. These two effects result in the difference between the received signals in channel 2 with and without the existence of antenna 1.

As described in Chapter 2, the maximum peak side lobe level can be estimated through the uncalibrated coupling coefficient β by using (2.28). The demand of a peak side-lobe level below -35 dB is satisfied only if the uncompensated coupling stays lower than -14 dB as demonstrated in Fig. 3.3. As a result of the two examples above, the requirements for the calibration accuracy can be derived. In order to realize a well-performing DBF receiver array, not only channel fluctuations smaller than 1.8 dB and 20° are needed but a cross-coupling larger than -14 dB also needs to be compensated.

3.2 Calibration Concepts

The differences between various receiver channels need to be characterized and corrected in terms of their gain and phase as much as possible. In addition, a decoupling method is also necessary to be applied to get rid of the coupling effect between channels. Thus, the antenna array calibration is an essential step to determine and perform the transformation of the signals in the real system into those of an ideal system with all channels being identical and isolated to reproduce as accurately as possible the far-field signals. This idea is sketched in Fig. 3.4.

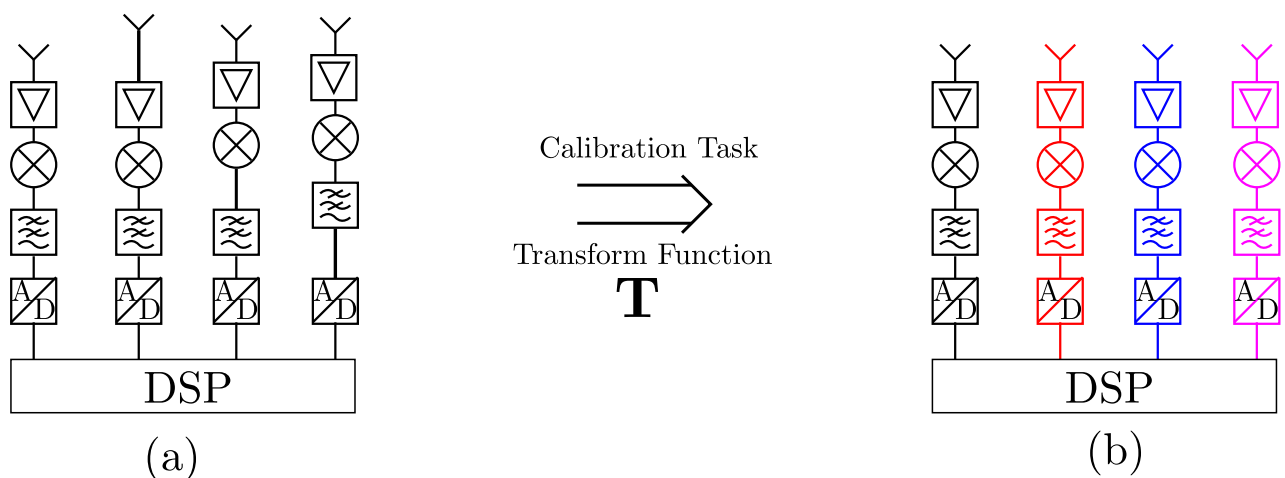


Figure 3.4: Calibration task: determination of a transform function \mathbf{T} between (a) the real receiver system and (b) the ideal system of all identical (same structure) and isolated (represented by different colors) channels.

Depending on their operation time, two types of calibrations can be found in literature, namely the offline and the online calibration.

In the first one, a receiver system can be characterized in an anechoic measurement chamber before it comes into operation. The signals are generated externally by far-field sources [35], [36] or by a near-field scanning system [37] in front of the receiver to replicate the working situation.

Thereby, deviations of all system parameters can be extracted and accurately compensated. In order to improve the calibration accuracy, an eigenstructure-based method based on the null-spectrum of the calibration signals is also proposed. A direct solution found in [38] is shown with several far-field sources to take the channel errors and mutual coupling into account. Alternatively, an iterative approach is discussed in [39] and [40] to calibrate jointly the channel deviations and the mutual coupling or the manifold error by using only a single source. The high cost, as well as the time-consuming and huge measurement effort are drawbacks of the off-line procedure as a trade-off. Thus, it can be performed only once or rarely in large time intervals.

In contrast, the online calibration is carried out periodically with shorter time intervals. The aim is to characterize small errors caused by alterations of the environment and to monitor the system during operation. Additionally, the online calibration has to affect the receiving operation as little as possible. Besides, a compact on-board calibration system is also another attractive approach with reasonable cost for the online procedure. In order to implement this system, two main construction concepts, namely internal and external, are proposed in the literature [41], [42], [43], [44].

Last but not least, the trade-off between the calibration accuracy and its effort is sketched in Fig. 3.5. Due to their complexities, the calibration methods with far-field sources as well as with a near-field scanning systems are only suitable for the offline task. In contrast, an online calibration system can be implemented by means of integrated coupler concepts or with several integrated on-board probes.

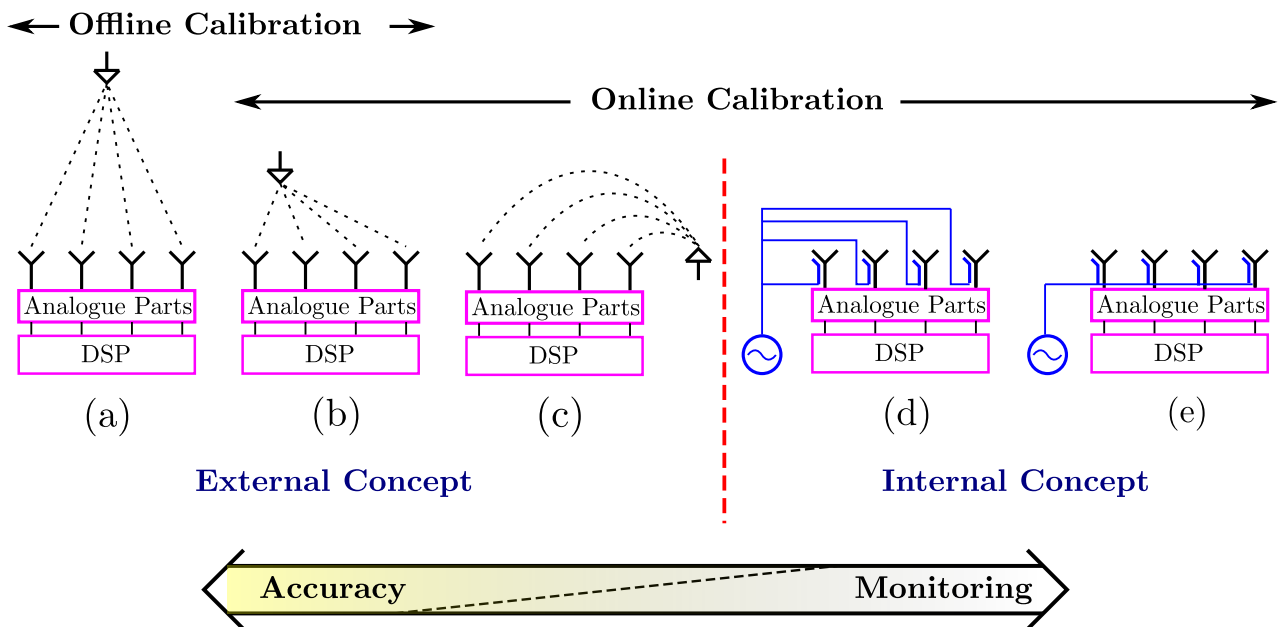


Figure 3.5: Various feeding concepts of calibration signals: external concept with (a) far-field source, (b) near-field source in front of the system, and (c) at end-fire, as well as internal concept with (d) parallel- and (e) serial distribution network

In the following sub-sections, we will review and discuss more in details the different concepts and their advantages as well as disadvantages, which are subject to applications with a large amount of system channels and high integration density.

3.2.1 Internal Calibration Concept

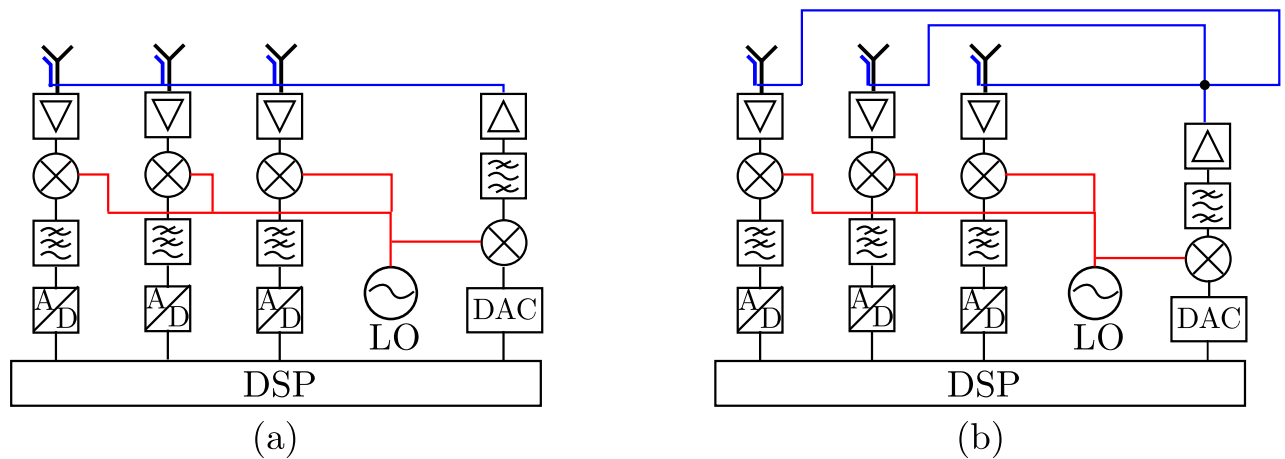


Figure 3.6: Internal calibration concept with integrated couplers: (a) serial and (b) parallel feeding networks.

The principle of the internal calibration concept is depicted in Fig. 3.6. A known signal is synthesized at base band and up-converted to the high frequency band. Depending on the type of distribution network, the calibration signal can be guided and fed serially [42] or be divided into several similar signals and fed in parallel into the receiver channels [41] by means of integrated couplers behind the patch antennas. Lastly, the signals go through all parts of the receiver chain and can be detected again at the base band. The fluctuations of the different channels can be determined by comparing the output signals of the receiver, and then corrected.

The main advantage of this concept is its simplicity. The known signals are distributed into the receiver channels via a complex passive distribution network, the behavior of which can be predicted by simulation. Additionally, due to the fact that the calibration part is integrated into the receiver system, the signal quality is less influenced by the outside environment, and the signal-to-noise ratio requirements are normally not so high.

On the other hand, the simplicity is also its drawback. Because of the fact that the calibration signals are fed behind the patch antennas, the errors of the antenna structure resulting from the fabrication tolerances cannot be detected and corrected with this concept. Furthermore, the fabrication tolerances of the calibration system are generally not considered and limit the calibration accuracy. In addition, the distribution network, which is normally large and the dimensions of which increase proportionally to the number of the channels, is integrated behind the antenna structure and within

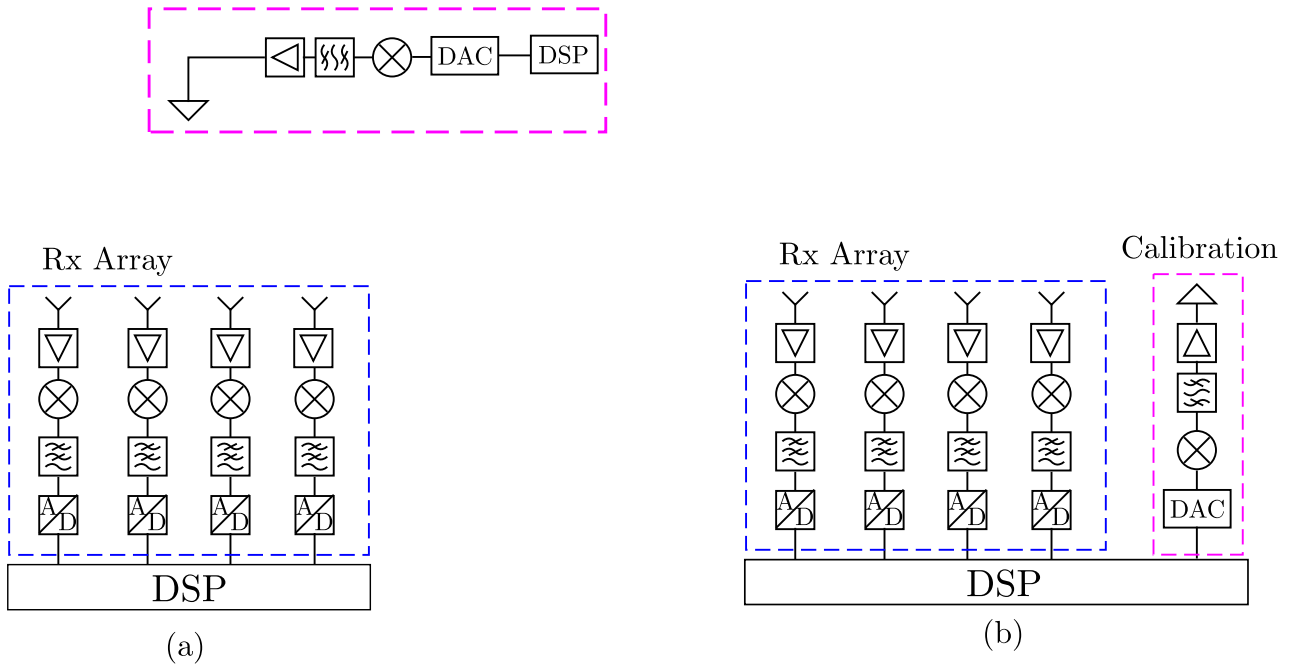


Figure 3.7: External calibration concept: (a) far-field source and (b) near-field probe.

the receiver system. The integration density is enormously increases and higher mutual coupling between the channels is observed.

Due to these two main disadvantages, the internal calibration concept, despite its simplicity, seems to be unsuitable for large-size arrays with desired multi-functions.

3.2.2 External Calibration Concept

The principle of the external concept can be seen in Fig. 3.7. The calibration system is built separately from the receiver. In contrast to the internal concept, the calibration signal at high frequency is radiated by means of an antenna, the so-called probe, and received by the antennas of the receiver system. Depending on the distance to the receiver system, we classify this concept into an antenna calibration with far-field or near-field probes.

Approaches with far-field calibration sources as discussed in [12, 13] achieve the highest accuracy. The working scenario is replicated in the calibration operation by the way, in which the known signals are generated and sent from far-field sources (satellites). Despite the high performance, the enormous and costly set-up is a drawback. Additionally, synchronizing the calibration system with the receiver is also a challenging task.

The concept with external on-board probes is another choice for the online calibration task. In [43], an on-board antenna placed off-boresight is used to perform the calibration task. Mechanical degradation of the system is thereby corrected. As suggested in [11], the external calibration receivers are interleaved in the transmitter system to track the channel fluctuations. Besides, an external sys-

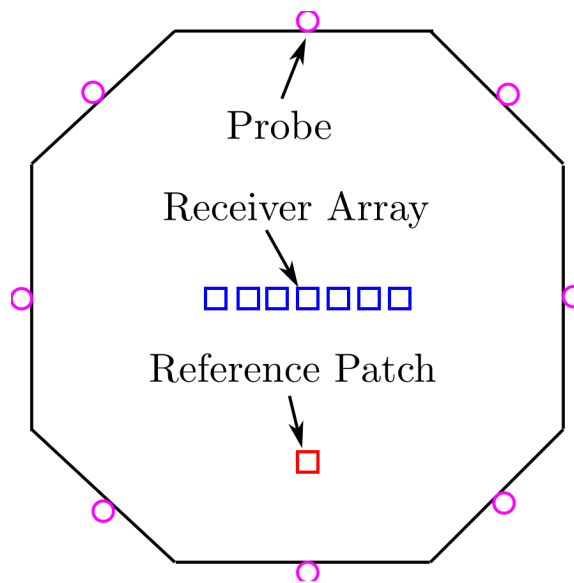


Figure 3.8: External setup of a on-line calibration system for a DBF receiver array.

tem with calibration probes at the periphery of the communication system is proposed in [44] to minimize the disturbance of the main operation.

This configuration is an attractive solution for a large DBF system as it avoids large and complex distribution networks. So, the integration density is nearly unchanged whilst the system enlargement is acceptable for a large array, especially at Ka-Band. Thus, we focus on analyzing the performance of this concept with calibration probes placed off-boresight in this work.

The set-up of the system is shown in Fig. 3.8. Three parts of the system can be seen: a linear/ planar receiver array, calibration probes, and reference channels. The highly integrated receiver system, which is to be characterized, is built in the center of the system. The calibration system consisting of several similar sub-systems is constructed equidistantly at the edge of the housing. Furthermore, reference channels are used to track on-line the signal deviation in different calibration subsystems.

In summary, a comparison between various set-up concepts of the calibration system, namely the internal and the external concept with near-field probes and far-field sources, is depicted in Table 3.1. Whilst the third one shows the best calibration accuracy, it relates to high cost because of external probes, and is not suitable for an online concept. Compared to the internal concept, the external concept with near-field probes requires higher dynamic range because of the different distances between the near-field probes and the various receiver elements, and can take into account the fabrication error of the patch. Additionally, its moderate hardware complexity as well as its high adaptability to large-size arrays are the other advantages. Hence, the external calibration concept with near-field probes is used in this work.

Table 3.1: Comparison of internal and external calibration concepts

	Internal Concept	External Concept	
		near-field	far-field
Accuracy	moderate	high	best
Correction of Antenna	no	yes	yes
Hardware Complexity	high distribution network	moderate near-field probe	high external probes (far-field)
Integration density	much higher	no	no
Coupling model	simple	complex	simple
Adaptability for large array	moderate	good	moderate
Required dynamic range	small	large	small

3.2.3 Calibration Procedure

Due to the presence of several on-board probes, this concept is classified as calibration with multi-sources. Two approaches, namely parallel and serial, are proposed in literature.

In the first approach, the calibration signals from various probes are sent simultaneously to the receiver array, and then separated in the signal processing algorithm by means of either the subspace method [45] or an optimization procedure [46]. Whilst low calibration time is achieved with the parallel approach, high computational demand is its drawback.

In the latter one, the on-board probes are switched on and off sequentially, and the calibration signals are sent in a Time Division Multiple Access (TDMA) scheme. Whilst the calibration time is P -times longer with P being the number of probes, lower computational complexity is achieved with this approach. Besides, this procedure can nowadays easily be implemented with commercial switches [47,48] at intermediate or high frequency or both of them to optimize the signal-to-noise ratio of the calibration signals. Thus, the serial switch approach is chosen for the calibration procedure and the experiments.

The calibration procedure is sketched in Fig. 3.9. The calibration signals are generated sequentially in the calibration system and are then sent to the receiver system. The coupling factor between the probes and the considered receiver patch is K . In the decoupling procedure, the receiver array is then characterized by analyzing all received signals, and a decoupling matrix can be calculated. As illustrated in Fig. 3.9, the accuracy of the calibration procedure depends on the prior knowledge of the coupling factor as well as on the decoupling algorithm, which are both examined more in details in Chapter 4 and Chapter 5, respectively.

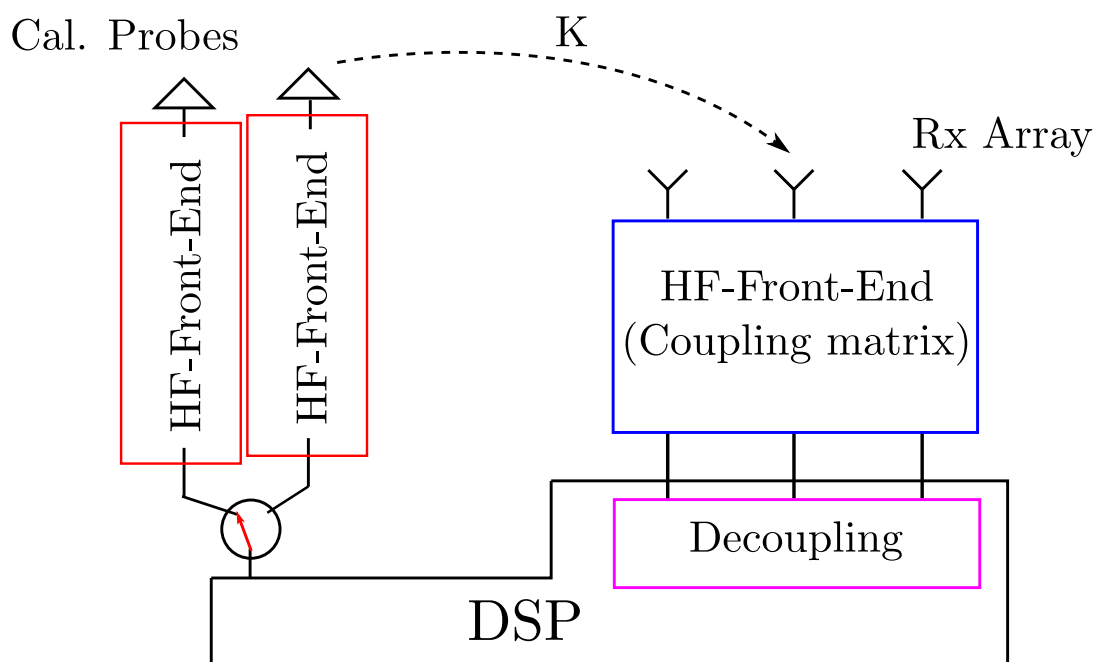


Figure 3.9: Schematic of the calibration procedure with on-board probes.

3.3 Conclusion

The error sources in a receiver array of a satellite communication system are presented and discussed in this chapter. This analysis yields that an efficient calibration system is needed to guarantee a high system performance. In addition, two main calibration concepts, namely internal and external ones, are also briefly examined in terms of their adaptability for the on-line calibration task.

Because of its low hardware complexity as well as its high accuracy, the external concept with a near-field calibration probes is the most suitable choice for the online correction of large receiver arrays. However, several issues must be considered before this concept can be applied further:

- (1) What kind of probes should be used and how are they implemented in the system?
- (2) How can the coupling between the probes and the receiver elements be described?
- (3) How is the calibration procedure to be performed?
- (4) What are the achievable accuracy and the system scalability of this calibration concept with respect to the size of the receiver system?

Inspired by the high demand of the considered application, we try to develop guidelines for the concept by taking into account the above mentioned issues in this work. The first three aspects are examined in Chapter 4 for the calibration of only channel fluctuations. Then, the procedure is extended to consider the joint calibration of channel deviations and mutual coupling in Chapter 5.

Additionally, experimental results are reported in Chapter 6 to validate the usefulness of the calibration concept. Last but not least, accuracy and scalability issues of the concept are discussed in Chapter 7.

4 Calibration of Channel Deviations

In order to characterize and correct channel deviations of a receiver system, the near-field calibration procedure proposed in Fig 3.9 in Chapter 3 is applied. If cross-talk between the channels is rather small and negligible, the n^{th} receiver can be modelled by a complex weighting factor W_n , which does not only include the complex gain of the active components but also the gain deviation of the patch antennas. Besides, K_{nm} denotes the coupling between the m^{th} probe and the n^{th} patch. The simplified procedure is depicted in Fig 4.1.

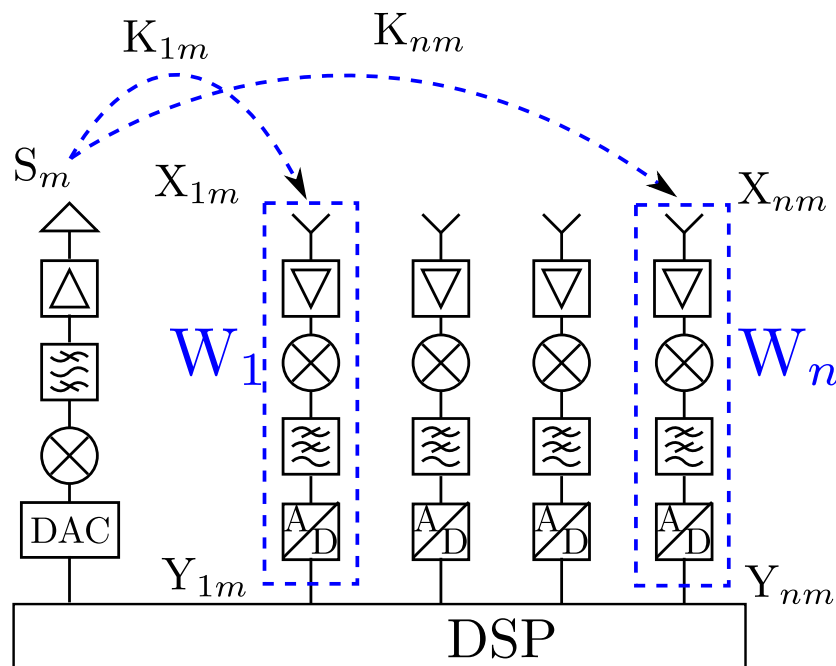


Figure 4.1: Calibration procedure of only channel fluctuations.

In addition, the calibration accuracy does not only depend on algorithms but also on the characterization of probe-receiver coupling. These are the two main themes in this chapter. In Section 4.1, the characteristics and the implementation of the calibration probe are discussed, whilst the modeling approach is highlighted in Section 4.2. Secondly, the calibration algorithms are discussed in Section 4.3. Additionally, a two-step simulation procedure is shown Section 4.4 to demonstrate the usefulness of the proposed concept. Lastly, a summary is given in Section 4.5.

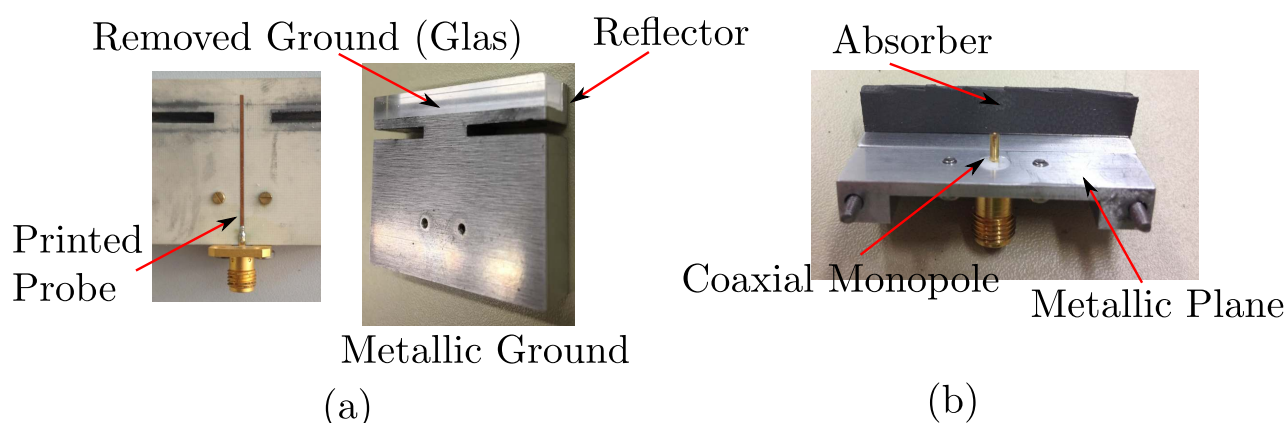


Figure 4.2: Calibration probes: (a) printed and (b) coaxial monopole.

4.1 Calibration Probes

In order to perform the calibration task, the probe shall exhibit the following characteristics: (1) minimized disturbance of the main system operation, (2) a simple structure with high reproducibility, and (3) a radiation pattern that is robust against fabrication tolerances, e.g., an omni-directional one.

As discussed in Chapter 3, the first requirement leads to the placement of the probes off-boresight. This set-up offers high decoupling between the calibration system and the main system during operation.

Regarding the second requirement, a vertical monopole and a horizontal dipole antenna are two attractive candidates because of their rather simple structure, low cost, and high manufacturing repeatability. Instead of circularly polarized signals as in the intended operation, linearly polarized signals sent by the calibration probes are used in our system because they can be received by the R/LHCP patches of the communication system and the probes are simpler to realize.

Thirdly, a monopole antenna features an up to 100° wider main beam than a horizontal dipole as shown in [15]. Hence, it is chosen to be the calibration probe in this work. Because of their ease of fabrication, we implemented two types of monopole probes, namely a coaxial probe and an on-substrate printed probe, as illustrated in Fig. 4.2.

The first probe is an on-substrate printed monopole. The $\lambda/4$ -monopole antenna is realized by removing the ground plane behind the probe. Its advantage is the possibility of integrating active components on the same board. A matching network can be simply designed to minimize the reflection and to improve the radiation efficiency of the calibration probe. Last but not least, a small reflector is constructed behind the probe to focus the calibration signal on the receiver array. Thereby, the disturbance of the environment during the calibration can be reduced. Due to its complex structure, its radiation characteristics are more difficult to be modeled, especially in the near-field region, and the width of the main beam is smaller than that of the second probe.

Moreover, a coaxial probe can be constructed from a coaxial connector¹. The pin length (normally 8-10mm) is cut down to 3.6mm ($\approx \lambda/4$). This modification allows to realizing a $\lambda/4$ -monopole. Due to its stable and simple construction, the coaxial probe offers an omni-directional radiation pattern in the H-plane. Furthermore, a transition or a matching circuit between the coaxial cable and the printed circuit board has to be implemented to feed the calibration signal to the probe. Besides, an absorber sheet² is glued on the reflector to minimize the ripples in the radiation pattern of the probe. The interaction between these probes and the receiver patch will be discussed in details in the following sections to synthesize analytical coupling models. Furthermore, their applicability in practical systems is illustrated in experiments in Chapter 6.

4.2 Probe-Patch Coupling

An accurate model of the probe-receiver coupling impacts significantly the accuracy of the calibration. Three main methods are found in the literature to characterize and to determine the coupling, namely an offline calibration, a full-wave simulation, and an analytical model.

The first approach yields the best calibration accuracy. However, the off-line measurement procedure needs to be performed for each fabricated system, which results in very high production cost. Instead of measurements, the simulation with full-wave programs such as HFSS or CST can be used to calculate the coupling between the calibration probe and all receiver elements. In this case, only the antenna structure, rather than the whole system, is simulated. Despite its high accuracy, this method is still time- and memory consuming, especially for large arrays. Hence, the development of an analytical coupling model is necessary to achieve a good calibration accuracy with acceptable computational effort. This third approach is discussed and developed in this chapter.

4.2.1 Analytical Model

In order to synthesize the coupling model at acceptable computational cost, far-field conditions are assumed to be fulfilled for the coupling. It means that the distance between the probe and the receiver element is sufficiently large so that the effect of multiple reflections is negligible. Furthermore, the electromagnetic field caused by the calibration probe is not modified by the presence of the receiver patch.

Based on these assumptions, the system theory can be applied. Therefor the probe-receiver coupling K , as illustrated in Fig. 4.3, is described by a product of three sub-functions as

$$K \propto K_1(r) \cdot K_2(\eta) \cdot K_3(\xi), \quad (4.1)$$

¹<http://rfconnector.com/sheets/SASF92DNFGT.pdf>. 2016

²Eccosorb: <http://www.eccosorb.eu>. 2016

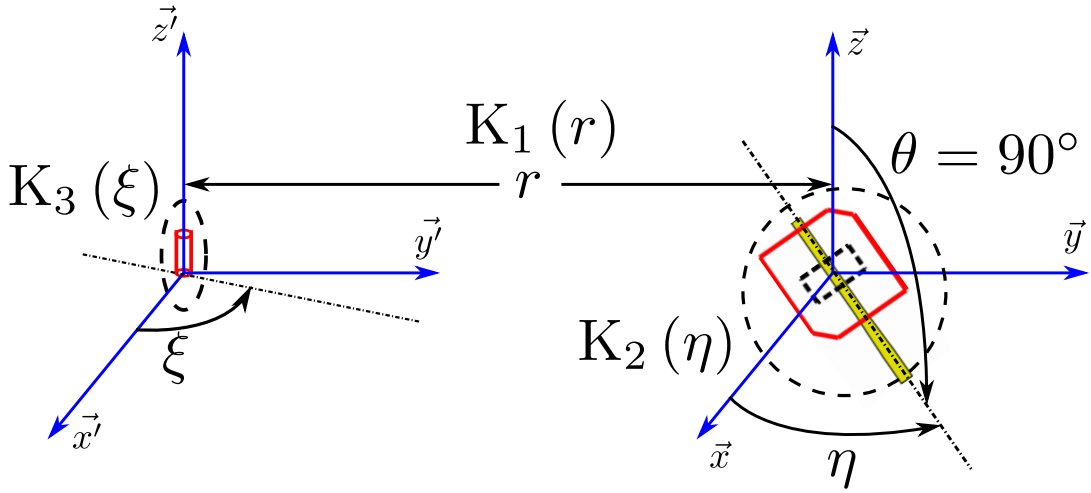


Figure 4.3: Coupling model.

where $K_1(r)$ is the propagation model of the calibration signal, and $K_2(\eta)$ and $K_3(\xi)$ describe the radiation characteristics of the patch and those of the probe in the plane $\theta = 90^\circ$, respectively.

Because a monopole antenna exhibits an omni-directional radiation pattern in the H-plane, $K_3(\xi)$ is constant for all ξ , here. Thus, Eq. 4.1 can be rewritten as:

$$K \propto K_1(r) \cdot K_2(\eta). \quad (4.2)$$

The radiation pattern $K_3(\xi)$ of four different proposed probe structures is shown in Fig. 4.4. Due to its complex structure compared to that of the coaxial probe, the main beam of the printed probe exhibits a ripple of approximately 2 dB, which impacts the accuracy of the proposed model. Additionally, the back lobes in the pattern are significantly suppressed by applying a reflector or an absorber sheet whilst modification of the main beam is also observed. If the maximum deviation is limited to 1 dB as illustrated in Fig. 4.4(e), the ξ -range of the coaxial probe with an absorber sheet is 80° in comparison to 30° for the printed probe with a reflector. This result leads to a compact system set-up with the calibration coaxial probes.

Moreover, if instead of a monopole, other antenna types are used as probe, their radiation characteristics need to be determined here.

4.2.2 Propagation model K_1

In order to derive the asymptotic behavior of the propagation function $K_1(r)$, the far-field condition with $r > r_{th} \gg \lambda$ is assumed to be valid. Additionally, the following phenomena are taken into account in the model synthesis procedure:

- The calibration signal sent from the side of the receiver array does not only propagate in the air but also partly in the substrate of the patch structure. Thus, a relative permittivity ϵ_r is used

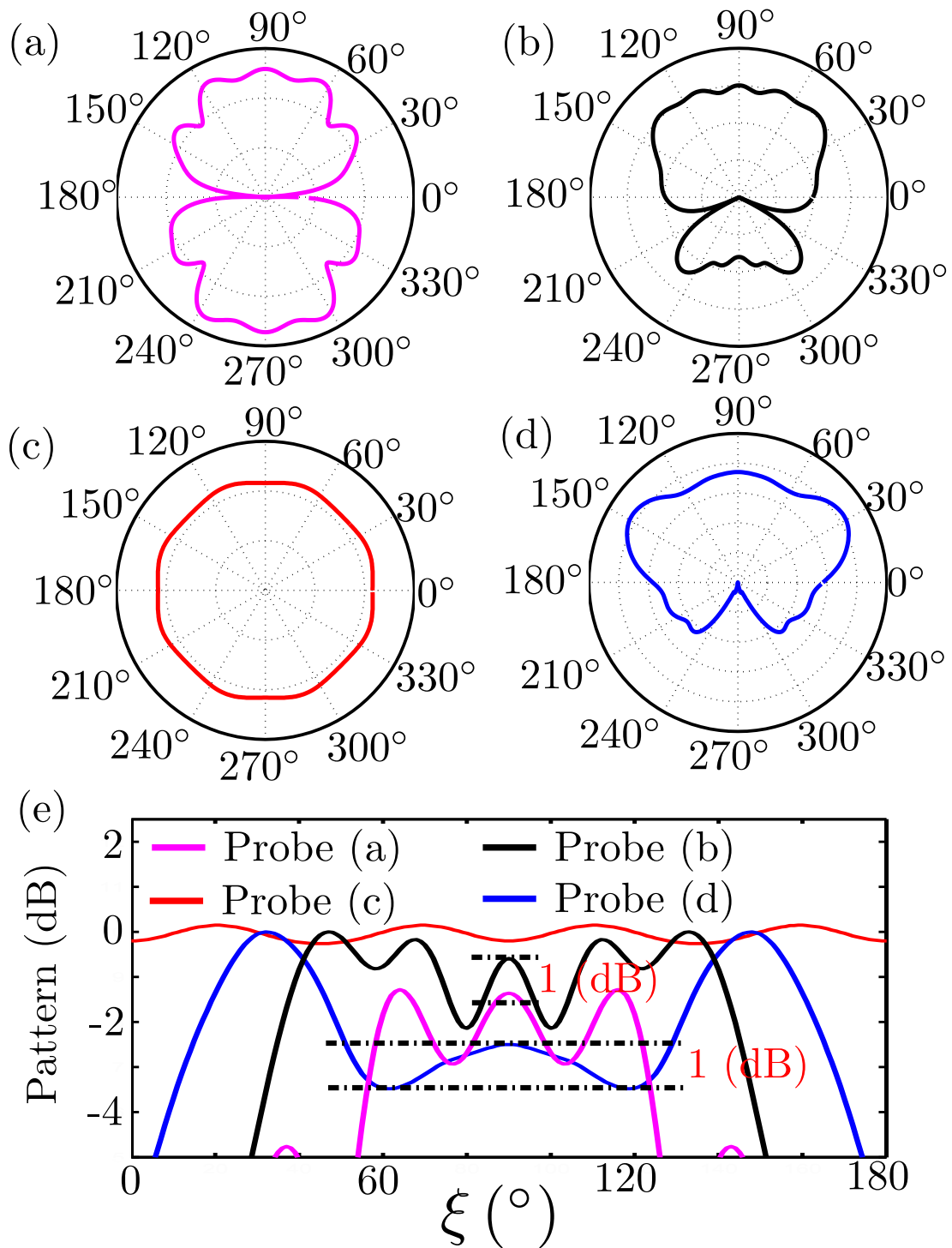


Figure 4.4: Radiation pattern of various monopole probes over the direction angle ξ : (a) printed probe without and (b) with reflector, (c) coaxial probe without and (d) with absorber sheet and (e) pattern comparison of all proposed probes.

to described this effect as

$$K_{11}(r) = \exp\left(-j2\pi\sqrt{\epsilon_r}\frac{r}{\lambda}\right). \quad (4.3)$$

- Secondly, the magnitude of the probe-receiver coupling decreases with the distance r due to the signal propagation in free space:

$$K_{12}(r) = \frac{1}{r} \quad (4.4)$$

- Additionally, the receiver element, which is a patch antenna, is not an isotropic radiator. Its radiation characteristic over θ can be described approximately as [25]

$$P_{patch}(\theta, p) = \cos^p(\theta) = \left(\frac{z}{\hat{r}}\right)^p. \quad (4.5)$$

As depicted in Fig. 4.5, $\hat{r} \approx r$ for large r . Moreover, a $\lambda/4$ -monopole antenna is used as a probe. The normalized current distribution function [8] is

$$I(z) = \cos\left(\frac{2\pi z}{\lambda}\right) \quad (4.6)$$

with z being the position on the probe. By using (4.5) and (4.6), the coupling function $K_{13}(r)$ describing the patch directivity can be derived as

$$\begin{aligned} K_{13}(r) &= \int_0^{z_{\max}} P_{patch}(\theta, p) \cdot I(z) dz \\ &= \frac{1}{r^p} \int_0^{z_{\max}} z^p \cos\left(\frac{2\pi z}{\lambda}\right) dz = \frac{\hat{K}_{13}}{r^p} \end{aligned} \quad (4.7)$$

- Multiple reflections of the signal between the probe and the receiver patch are small and negligible.

Thus, the propagation function $K_1(r)$ is determined asymptotically in the far-field as

$$\begin{aligned} K_1(r) &= K_{11}(r) \cdot K_{12}(r) \cdot K_{13}(r) \\ &= \frac{\hat{K}_{13}}{r^{(p+1)}} \cdot \exp\left(-j2\pi\sqrt{\epsilon_r}\frac{r}{\lambda}\right) \end{aligned} \quad (4.8)$$

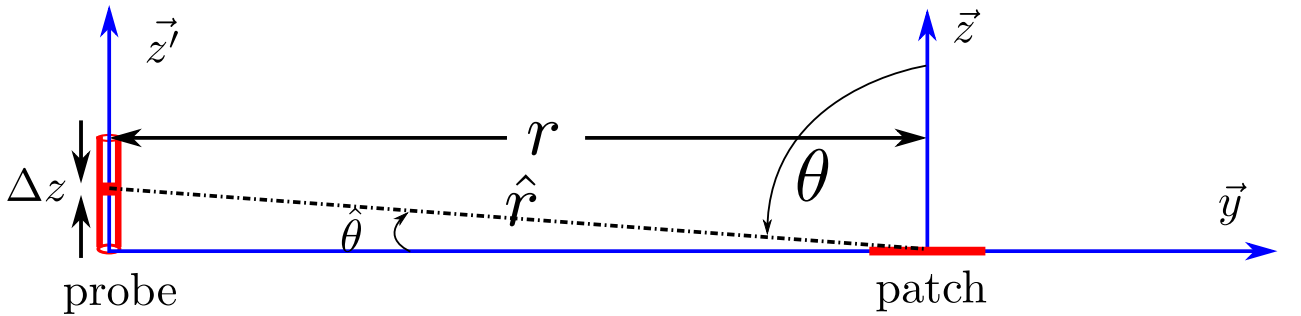


Figure 4.5: Propagation model of the calibration signals.

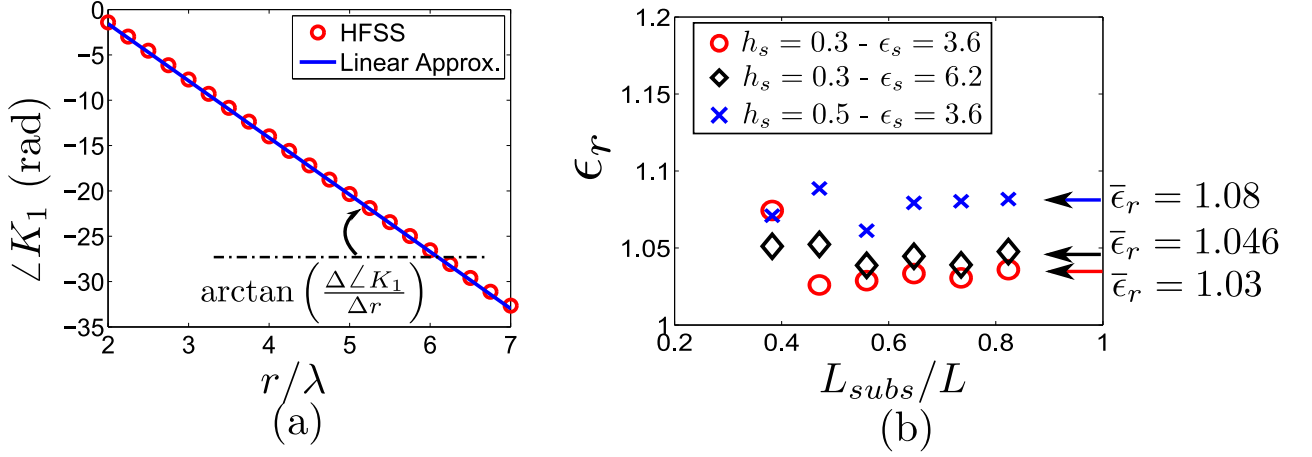


Figure 4.6: Phase function of the propagation model.

with \hat{K}_{13} being positive and independent from r . To improve the propagation model for $r < r_{th}$, a damped oscillation function $\hat{K}_{13}(r)$ instead of a constant is applied as

$$\hat{K}_{13}(r) = A_0 + \frac{1}{r^\rho} \left[A_1 \cos\left(\frac{2\pi r}{\hat{\lambda}}\right) + B_1 \sin\left(\frac{2\pi r}{\hat{\lambda}}\right) \right] \quad (4.9)$$

All parameters ρ , A_0 , A_1 , B_1 and r_{th} can be determined through simulation with full-wave tool such as HFSS³. Now the propagation function $K_1(r)$ can be written in a more general form as

$$K_1(r) = \frac{A_0 + \frac{1}{r^\rho} \left[A_1 \cos\left(\frac{2\pi r}{\hat{\lambda}}\right) + B_1 \sin\left(\frac{2\pi r}{\hat{\lambda}}\right) \right]}{r^{(p+1)}} \cdot \exp\left(-j2\pi\sqrt{\epsilon_r}\frac{r}{\lambda}\right). \quad (4.10)$$

Last but not least, the accuracy of the propagation model is verified by comparison with the HFSS simulation.

As shown in Fig. 4.6, the phase of K_1 can be approximately described by a linear function with respect to r . The effective permittivity ϵ_r in (4.10) follows from the slope of the phase $\angle K_1$ as

$$\epsilon_r = \left(\frac{\Delta\angle K_1}{2\pi\Delta r/\lambda} \right)^2. \quad (4.11)$$

It is slightly larger than $\epsilon_r = 1$ of air, and nearly constant over $\frac{L_{subs}}{L}$ with L_{subs} and L denoting the in-substrate propagating distance of the signal and the total distance between the probe and the receiver, respectively. It depends on the height h_s as well as on the relative permittivity $\epsilon_{r,subs}$ of the antenna substrate.

In addition, the proposed magnitude function, as can be seen in Fig. 4.7, is already valid for $r \geq 4\lambda$, whilst the far-field approximation only holds for $r \geq r_{th} = 10\lambda$.

³Anslys: <https://www.ansys.com/products/electronics/ansys-hfss>

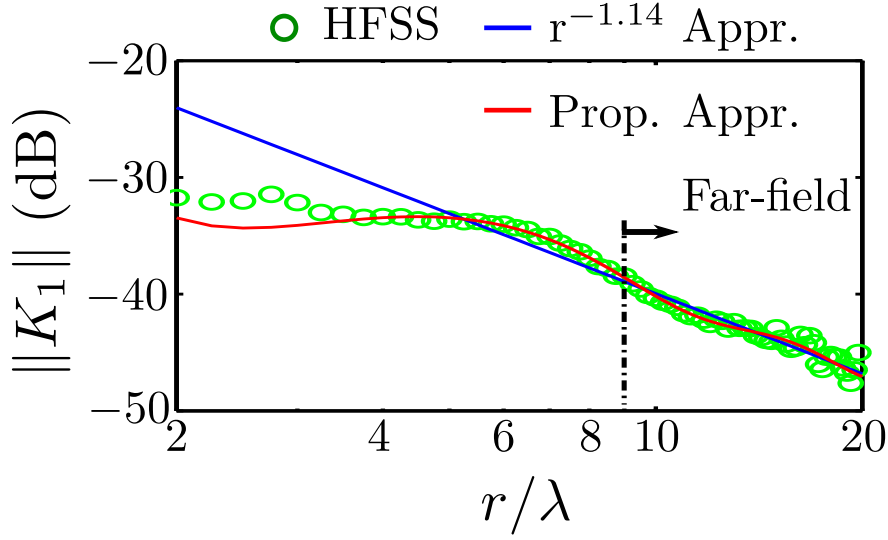


Figure 4.7: Magnitude function of the propagation model.

4.2.3 Radiation characteristics K_2 of the patch

The patch behavior is expressed by the radiation characteristics K_2 with respect to the rotation angle η in the xy -plane ($\theta = 90^\circ$). Due to the fact that the RHCP patch is a mirrored version of the LHCP patch relating to its feed line, we can derive the relation

$$K_{2,\text{RHCP}}(\eta) = K_{2,\text{LHCP}}(-\eta), \quad (4.12)$$

which is demonstrated in Fig. 4.8.

With respect to the 2π -period of η , the function K_2 of a RHCP patch, as demonstrated in Fig. 4.8, is expressed by a Fourier expansion

$$K_2(\eta) = C_0 + \sum_{t=1}^T [A_t \cos(t\eta) + B_t \sin(t\eta)]. \quad (4.13)$$

With L values of $K_2(2\pi \cdot l/L)$ ($l = 0, \dots, L-1$) determined by the simulation in HFSS, the complex coefficients C_0 , A_t , and B_t can be calculated as

$$C_0 = \frac{2}{L} \sum_{l=0}^{L-1} K_2\left(2\pi \frac{l}{L}\right), \quad (4.14)$$

$$A_t = \frac{2}{L} \sum_{l=0}^{L-1} \left[K_2\left(2\pi \frac{l}{L}\right) \cdot \cos\left(2\pi t \frac{l}{L}\right) \right], \quad (4.15)$$

$$B_t = \frac{2}{L} \sum_{l=0}^{L-1} \left[K_2\left(2\pi \frac{l}{L}\right) \cdot \sin\left(2\pi t \frac{l}{L}\right) \right]. \quad (4.16)$$

In order to keep the residual error between the Fourier-based model and the HFSS simulation below -20dB , $T = 3$ is chosen in this work.

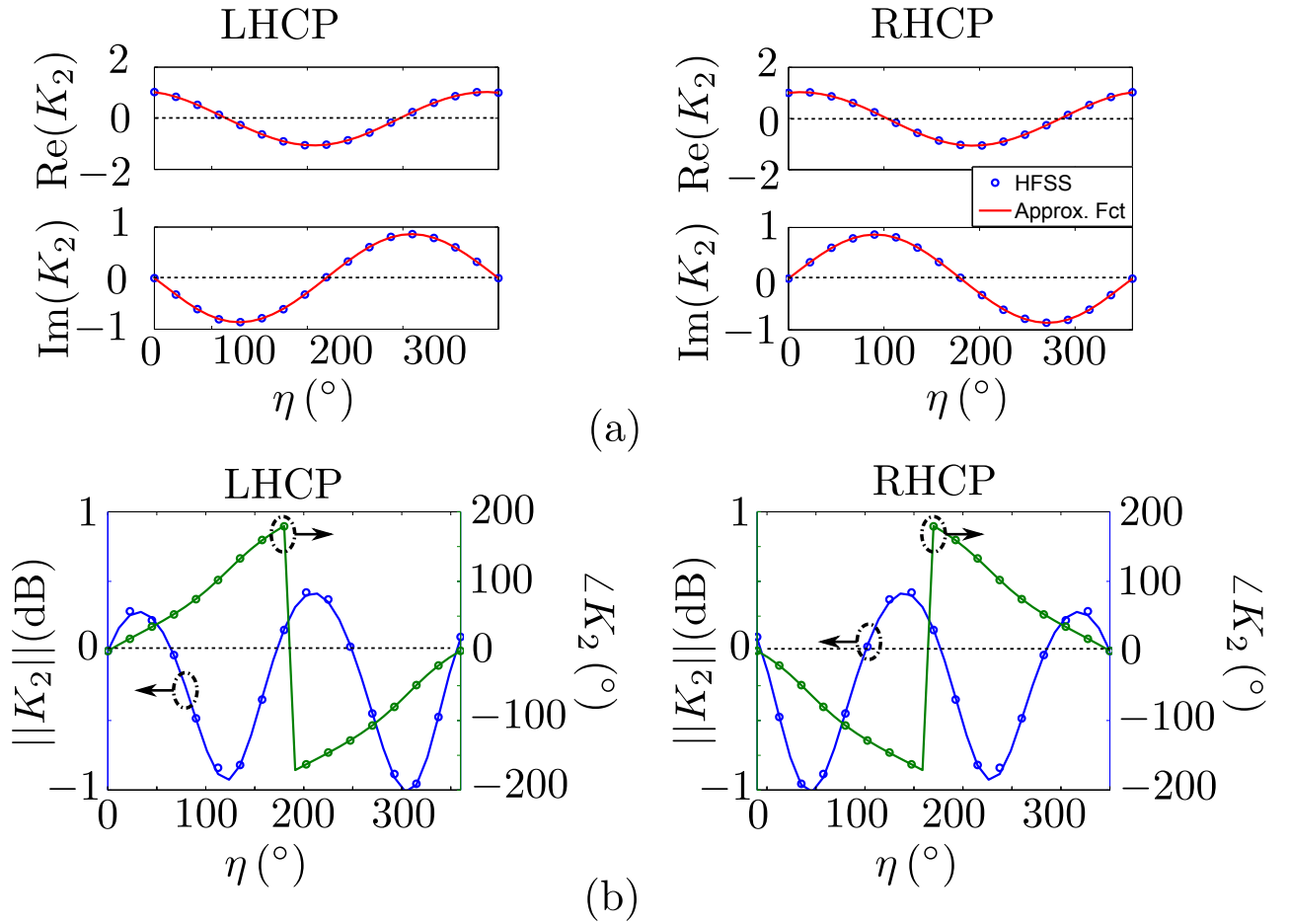


Figure 4.8: Radiation characteristic of circular-polarized patch at $\theta = 90^\circ$: (a) real and imaginary parts as well (b) magnitude and phase of the LHCP and RHCP patches.

4.2.4 Model Expansion with Superposition Principle

As discussed above, a metallic reflector or an absorber sheet is placed behind the probe to minimize the disturbance of the surroundings during calibration and vice versa. Because of its easy fabrication, a planar reflector is taken into account in this work.

An image source of the calibration probe can be constructed virtually based on image theory. As a result, the coupling is determined by means of the superposition principle as

$$K = K_1(r) K_2(\eta) + \sigma K_1(r_{im}) K_2(\eta_{im}). \quad (4.17)$$

The geometry parameters are defined in Fig. 4.9. The complex reflection coefficient σ depends on the reflector parameters including of conductivity and surface roughness. To keep the model simple, its dependence on the reflection angle β_p is neglected in this work. Additionally, the σ values of the metallic reflector as well as of the absorber are chosen to $\sigma = -1$ and $\sigma = 0$, respectively.

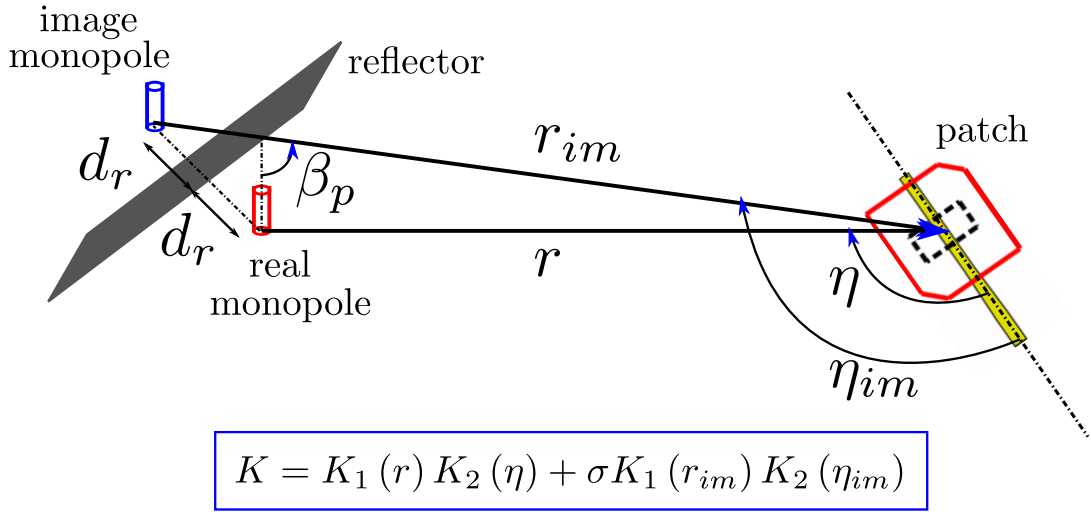


Figure 4.9: Model of the coaxial probe using image theory.

4.3 Algorithms

If the m^{th} probe is turned on, the received signal Y_{nm} at the n^{th} receiver is

$$Y_{nm} = W_n \cdot X_{nm} = W_n \cdot K_{nm} \cdot S_m \quad (4.18)$$

with S_m and X_{nm} being the transmitted and the ideal signal before the RF path, respectively.

The relative channel coefficient R_{nm} of the n^{th} channel with respect to channel 1 is determined as

$$R_{nm} = \frac{W_n}{W_1} = \frac{Y_{nm}/X_{nm}}{Y_{1m}/X_{1m}} = \frac{Y_{nm}}{Y_{1m}} \cdot \frac{K_{1m}}{K_{nm}}. \quad (4.19)$$

Furthermore, various averaging methods, namely the arithmetic and the geometric mean, can be applied to estimate the relative channel coefficient if measurement results of M calibration probes are used.

Arithmetic Mean

The arithmetic mean is the most commonly used method in different experiments with an assumption of randomly gaussian distributed measured samples. It is defined as

$$R_n = \frac{1}{M} \sum_{m=1}^M R_{nm} = \frac{1}{M} \sum_{m=1}^M \left(\frac{Y_{nm}}{Y_{1m}} \cdot \frac{K_{1m}}{K_{nm}} \right). \quad (4.20)$$

The magnitude and the phase of the complex coefficient R_n are estimated as

$$\|R_n\|_{\text{dB}} = 20 \cdot \log \left(\frac{1}{M} \sum_{m=1}^M R_{nm} \right), \quad (4.21)$$

$$\angle R_n = \angle \left(\frac{1}{M} \sum_{m=1}^M R_{nm} \right). \quad (4.22)$$

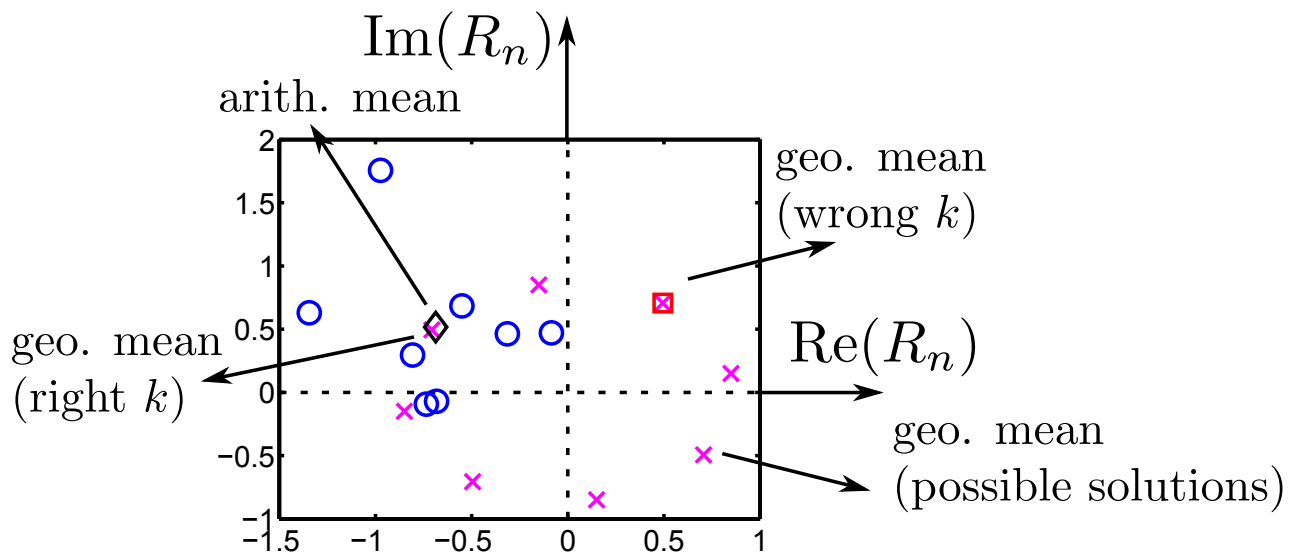


Figure 4.10: Example of the relative channel factor R_n measured with various calibration probes: measured points (\circ), arithmetic mean (\diamond), possible solutions of the geometric mean (\times) and the geometric mean with wrong k (\square).

Geometric Mean

In contrast to the arithmetic mean, the geometric mean, also called the log-average, is determined as

$$R_n = \sqrt[M]{\prod_{m=1}^M R_{nm}} = \sqrt[M]{\prod_{m=1}^M \left(\frac{Y_{nm}}{Y_{1m}} \cdot \frac{K_{1m}}{K_{nm}} \right)}. \quad (4.23)$$

As a result, the magnitude and the phase of the complex R_n can be calculated as

$$\|R_n\|_{\text{dB}} = \frac{1}{M} \sum_{m=1}^M 20 \log(\|R_{nm}\|), \quad (4.24)$$

$$\angle R_n = \left(\frac{1}{M} \sum_{m=1}^M \angle R_{nm} \right) + k \frac{2\pi}{M}, \quad \text{with } k = 0, \dots, (M-1). \quad (4.25)$$

Combination of both methods

Regarding (4.24), the geometric mean relates to the power of the measurement samples, and its behavior is more stable in case of low SNR measurements with existence of outliers in comparison to the arithmetic mean.

Due to the log-operator, an ambiguity of the phase estimation with the geometric mean is observed in (4.25). As a result, this leads to a large phase error if a wrong period k in (4.25) is chosen. On the other side, the arithmetic mean in (4.22) shows an unambiguous solution. As illustrated in Fig. 4.10, the periodicity coefficient k in (4.25) is chosen to minimize the difference between the solutions

$R_{n,\text{geo}}$ and $R_{n,\text{arith}}$ estimated by means of the geometric and arithmetic mean, respectively, as

$$\min_{k=0,\dots,(M-1)} \|R_{n,\text{geo}} - R_{n,\text{arith}}\|_2^2. \quad (4.26)$$

4.4 Simulation

The two-step simulation procedure sketched in Fig. 4.11(a) is used in this work to verify the proposed calibration concept.

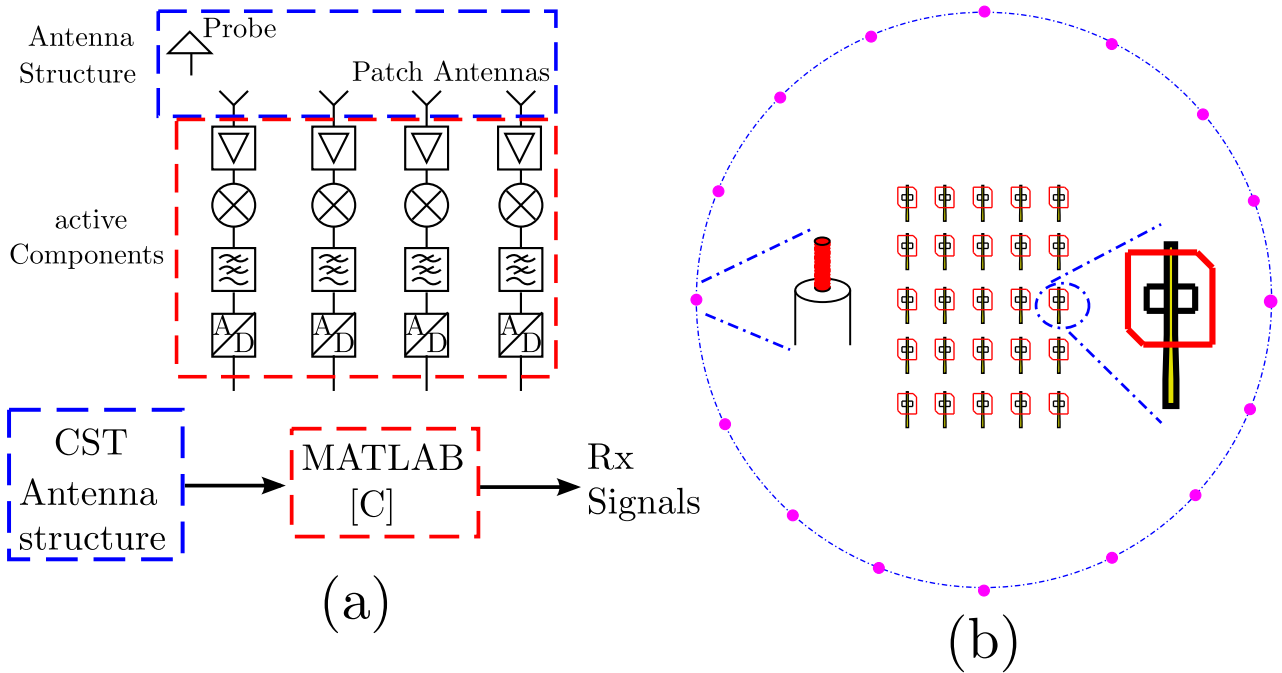


Figure 4.11: (a) Schematic of the two-step simulation procedure with CST and MATLAB and (b) structure of a 5x5 patch array with 16 connector probes.

In the first step, a planar array of 5x5 patches with 16 calibration probes depicted in Fig 4.11(b) is simulated in the full-wave simulation program CST⁴. The interaction between the calibration probes and each receiver patch can be determined in terms of the scattering parameters. The calculated mutual coupling of two patches does not exceed of -17 dB for two adjacent elements and can thus be neglected. Besides, the behavior of the patch array is simulated also with far-field excitation for verification.

Furthermore, a diagonal matrix $[C]_A$ representing the channel factors of the signal processing part of the receiver array can be generated in MATLAB⁵. Finally, by cascading the simulation results in MATLAB, the output signals of the receiver system can be determined for both cases, i.e., the

⁴CST Microwave Studio: www.cst.com/products/cstmws

⁵<https://de.mathworks.com>

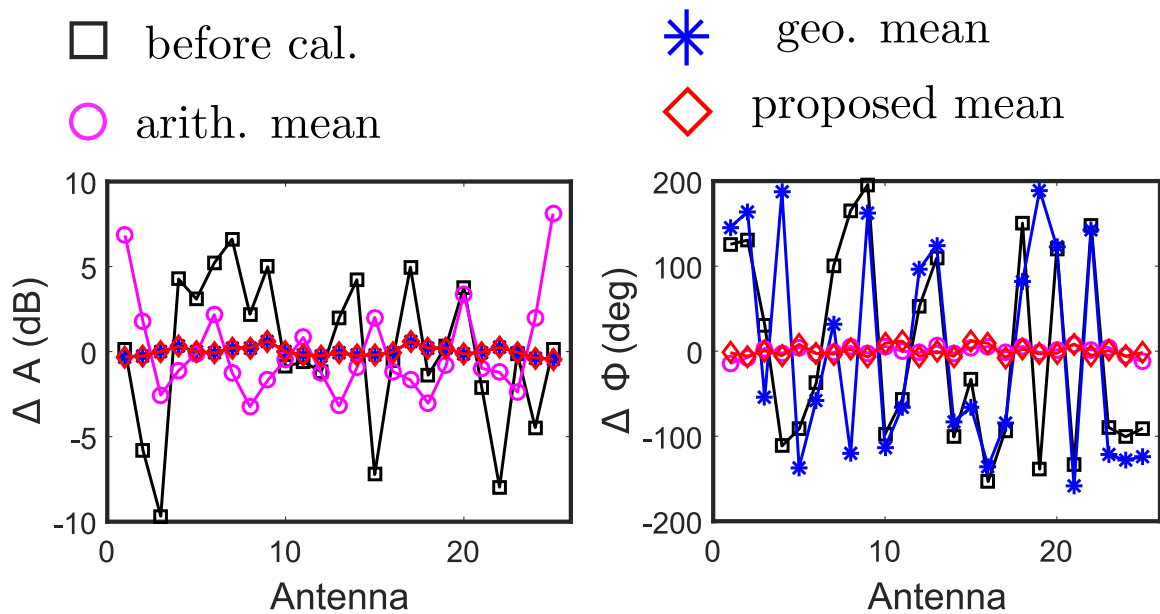


Figure 4.12: (Left) Amplitude and (right) phase deviation of the 5x5-patch array before and after calibration with three various averaging methods.

calibration and the far-field excitation. It should be noted, that the impact of additive white noise in the calibration measurements is not taken into account in this simulation and its effect will be discussed later in Chapter 7.

As depicted in Fig. 4.12, the correction of the amplitude and the phase deviations by means of the near-field calibration method is illustrated for the channel factors of the 5x5 receiver array. Additionally, the proposed mean demonstrates how the amplitude problem of the arithmetic mean and the periodicity problem of the geometric mean is overcome. As a result, a maximum amplitude deviation of 0.6 dB and a maximum phase error of 11° are achieved.

4.5 Summary

The calibration of channel deviations by means of an on-board calibration system is discussed. Two aspects are considered, namely the characterization of the probe-receiver coupling and the calibration procedure.

In the first topic, an analytic model of the probe-receiver coupling is synthesized step-by-step based on system theory. Whilst the calibration probe is characterized by an omni-directional radiation, the characteristics of the patch receiver are described by a Fourier model. In addition, the interaction between the probe and the receiver is derived asymptotically under the far-field assumption.

In comparison to full-wave simulation programs such as Ansys HFSS, the computational complexity is dramatically reduced and the memory requirements are significantly lowered.

Arithmetic and geometric mean methods as well as their characteristics are highlighted in the later one. Whilst the arithmetic mean shows large estimation errors in the presence of outliers, ambiguity problems are observed in the geometric mean. In order to achieve a high calibration accuracy, a combination of both mean methods is proposed in this work.

Despite the low computational effort of the analytical model, the requirements for the channel deviations derived in Chapter 3 can be fulfilled after the calibration in the simulation of the 5x5 receiver array with 16 probes. This demonstrates the usefulness of the proposed calibration procedure.

5 Calibration of Coupling Matrix

The joint calibration of the channel deviations and the mutual coupling is an important aspect discussed in this work. A procedure to determine coupling matrix is proposed and then examined in details.

In order to characterize the behavior of a receiver array, the representation of the coupling matrix is firstly reviewed in Section 5.1. Moreover, various simplified models of the coupling matrix are assumed for different system architectures.

As the main theme of this chapter, various decoupling algorithms are proposed in Section 5.2 to determine the simplified coupling matrix of the receiver array. Additionally, simulation results obtained in MATLAB to verify the applicability of the proposed procedure are reported in Section 5.3. Lastly, a summary of this chapter is given Section 5.4.

5.1 Coupling Matrix

The concept of coupling matrix is illustrated in Fig. 5.1. A signal S , generated by a far-field source (e.g., a satellite), propagates through the atmosphere and is detected by a receiver array. A vector of signals $\vec{S} = [S_1, \dots, S_N]^T$ representing a replicated version of the original signal S is assumed to be perfectly sampled by N receivers. By applying antenna theory (Chapter 2), a complex scaled version of S can be reconstructed.

In practice, the ideal signal \vec{S} is detected by a receiver system consisting of different analogue and digital processing components before it is displayed on a monitor as signal $\vec{R} = [R_1, \dots, R_N]^T$. Under the assumption of a linear receiver system, a transformation with a coupling matrix $[C]$ can be used to describe the relation between the input vector \vec{S} (ideal signals) and the output vector \vec{R} (actual signals) as

$$\vec{R} = [C] \vec{S}, \tag{5.1}$$

$$\begin{pmatrix} R_1 \\ R_2 \\ \vdots \\ R_N \end{pmatrix} = \begin{pmatrix} C_{11} & C_{12} & \cdots & C_{1N} \\ C_{21} & C_{22} & \cdots & C_{2N} \\ \vdots & \vdots & \ddots & \vdots \\ C_{N1} & C_{N2} & \cdots & C_{NN} \end{pmatrix} \begin{pmatrix} S_1 \\ S_2 \\ \vdots \\ S_N \end{pmatrix}.$$

Here, the components C_{nn} on the main diagonal correspond to the channel factors (gain and phase)

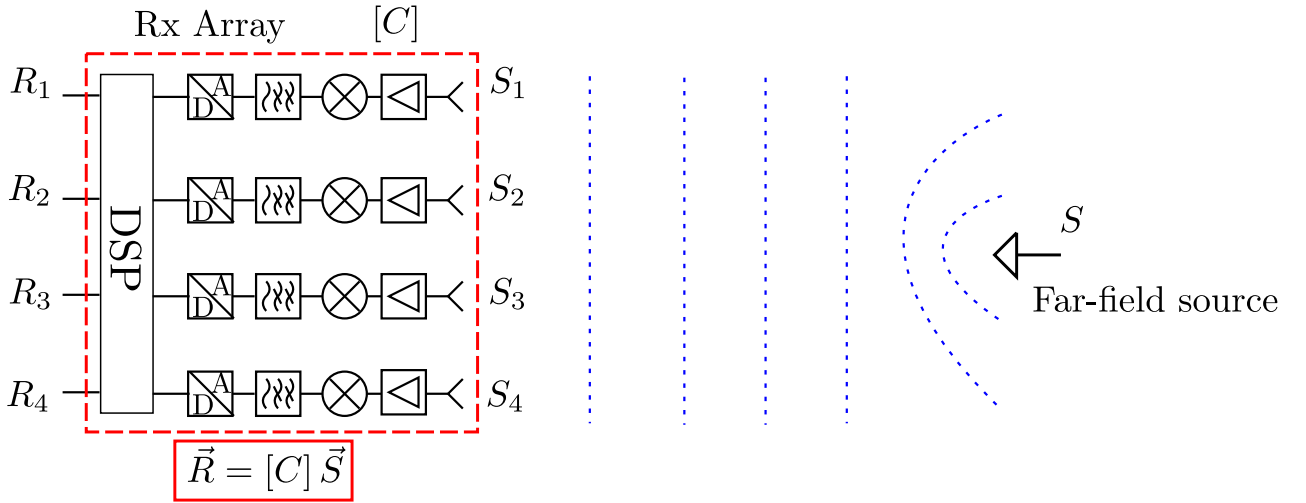


Figure 5.1: Concept of coupling matrix

whilst the other coefficients C_{nk} with $n \neq k$ represent the mutual coupling between the n^{th} and the k^{th} channel.

As exemplified in Chapter 3, the goal of the calibration task is to determine the transform function \mathbf{T} defined as

$$\mathbf{T} : \vec{R}(\theta, \phi) \mapsto \vec{S}(\theta, \phi) = [\mathbf{C}]^{-1} \cdot \vec{R}(\theta, \phi) \quad (5.2)$$

with $^{-1}$ denoting the inverse matrix. In other words, the calibration procedure is used to characterize the coupling matrix $[\mathbf{C}]$ of the receiver system.

Besides, the coupling matrix $[\mathbf{C}]$ is generally dependent on the direction (θ, ϕ) of the far-field source due to higher order modes generated in the antenna structure. In practice, single-mode mutual coupling is assumed, and the coupling matrix is considered as an average direction-independent relationship [49] written as

$$[\mathbf{R}] = [\mathbf{C}] [\mathbf{S}], \quad (5.3)$$

with

$$\begin{aligned} [\mathbf{R}] &= \left[\vec{R}(\theta_1, \phi_1), \vec{R}(\theta_2, \phi_2), \dots, \vec{R}(\theta_M, \phi_M) \right], \\ [\mathbf{S}] &= \left[\vec{S}(\theta_1, \phi_1), \vec{S}(\theta_2, \phi_2), \dots, \vec{S}(\theta_M, \phi_M) \right]. \end{aligned} \quad (5.4)$$

If M sources are known, the matrix $[\mathbf{C}]$ can be obtained, as derived in [36, 38, 49], by using a Least Square Method such that

$$[\mathbf{C}] = [\mathbf{R}] [\mathbf{S}]^{\text{H}} \left([\mathbf{S}] [\mathbf{S}]^{\text{H}} \right)^{-1}, \quad (5.5)$$

with $^{\text{H}}$ denoting the Hermitian matrix. In order to solve the system of linear equations with high accuracy, a large number of sources is needed with $M \gg N$. Especially for large-size receiver arrays, this requirement calls for a high SNR of the calibration signals as well as for a huge number

of known sources. Whilst these requirements can be satisfied in an offline calibration procedure in a measurement chamber, they are, however, still challenges for an integrated on-board system.

This observation motivates us to synthesize a simplified model of the coupling matrix to maintain an acceptable number of sources in the online calibration procedure.

Firstly, the mutual coupling between patch antennas is normally negligible for large element distances as demonstrated in Chapter 3. Moreover, the possibility that a receiver channel is coupled with all the other is extremely unlikely. Thus, we can assume that the n^{th} receiver is influenced by only $L_n - 1$, and not by all other channels with $L_n < M$.

On the other hand, in the present context, a modular approach is applied to construct a large-size array as mentioned in Chapter 2. This means, the receiver array is built by assembling several sub-modules with similar design. If a sub-module is characterized, information of unessential (negligible) coupling coefficients can be extracted and this prior knowledge can be applied to all others. From a practical point of view, we can assume that only L_n essential coefficients of the n^{th} row vector \vec{c}_n of the coupling matrix $[C]$ need to be calculated. The number L_n , which is different for various receiver channels, includes the channel factor and $L_n - 1$ coupling coefficients. Normally, $L_n \ll N$ holds. Thus, the calibration approach can be performed online with a limited number M of known sources.

5.2 Decoupling Algorithms

In this section, a calibration procedure is proposed and three different algorithms are described. Without loss of generality, the procedure is explained for a linear array to ease the mathematic formulation. The extension to the case of planar arrays is straightforward, though.

It should be mentioned here that the calibration algorithms in this work are proposed and derived for known sources in the near-field region of the whole array. Similar approaches are discussed in [36, 38] for the case of far-field sources.

5.2.1 Calibration Procedure

A Time Division Multiple Access scheme is proposed in the procedure. Various calibration subsystems are switched on and off sequentially to send orthogonal signals to the receiver array.

If a signal S_m sent from the m^{th} probe is received by the n^{th} receiver, the received signal S_{nm} is

$$S_{nm} = K_{nm}S_m \quad (5.6)$$

with K_{nm} being the coupling between the probe m and the patch n . Furthermore, R_{nm} denotes the output signal of the receiver system.

Due to the switching procedure between the calibration probes, deviations of the calibration signals S_m are observed and need to be compensated by means of a reference receiver channel. Alternatively, an external reference channel or an internal compensation network can be utilized as illustrated in Fig. 5.2

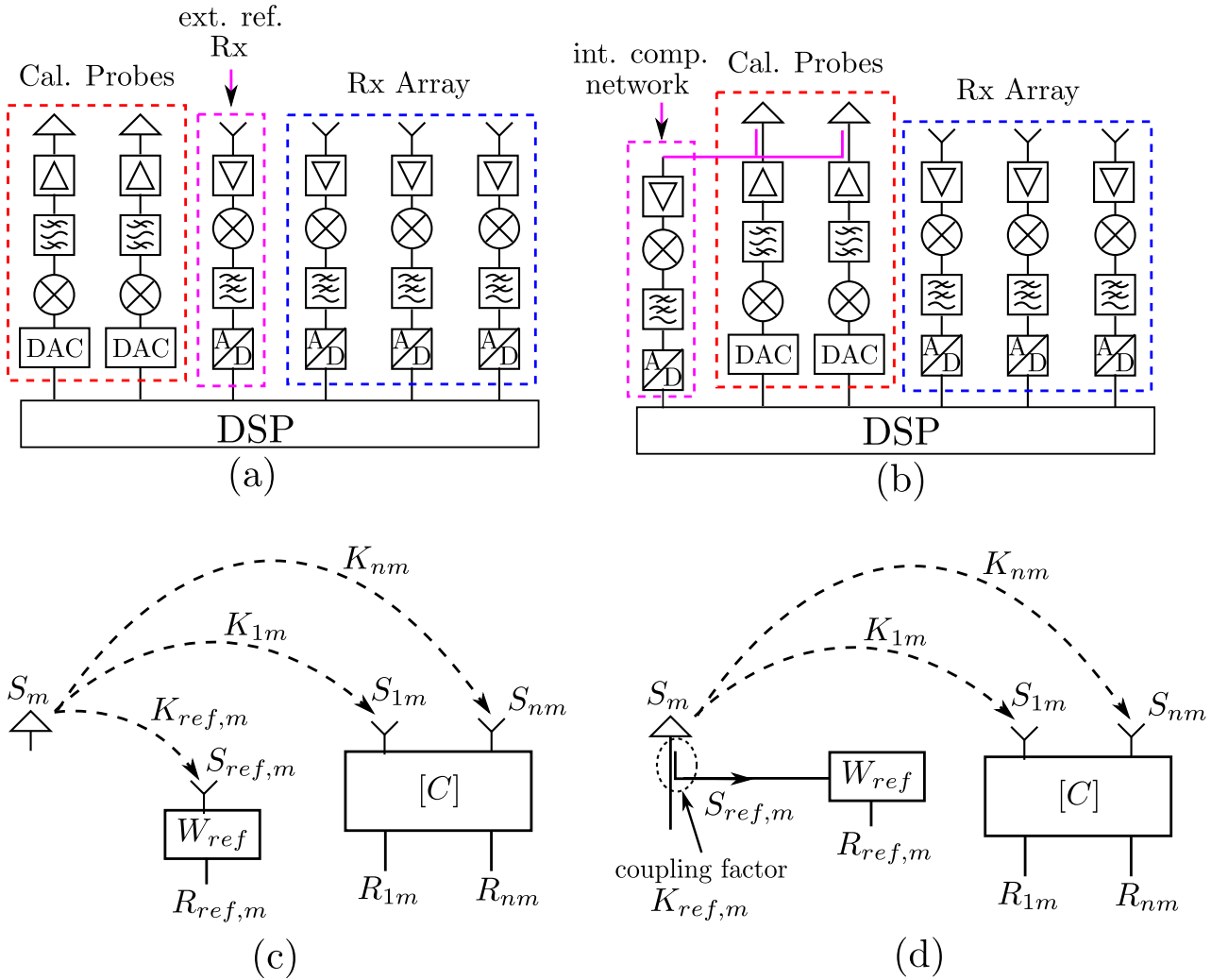


Figure 5.2: Schematic of the calibration procedure with external probes: (a) external reference channel and (b) internal compensation network as well as their signal propagation models in (c) and (d), respectively.

In the similar way, $K_{ref,m}$ is defined as the relation between the received signal $S_{ref,m}$ in the reference channel and the probe signal S_m :

$$S_{ref,m} = K_{ref,m} \cdot S_m. \quad (5.7)$$

In case of the external reference approach, $K_{ref,m}$ is the probe-receiver coupling, whilst it is the scattering parameter of the compensation network in the internal reference approach and can be determined by simulation.

If the probe m is switched on, the output signal $R_{ref,m}$ of the reference channel with a channel factor W_{ref} is

$$R_{ref,m} = W_{ref} \cdot S_{ref,m}. \quad (5.8)$$

Furthermore, the parameters X_{nm} and Y_{nm} of the calibration procedure can be determined as

$$X_{nm} = \frac{S_{nm}}{S_{ref,m}} = \frac{K_{nm}S_m}{K_{ref,m}S_m} = \frac{K_{nm}}{K_{ref,m}}, \quad (5.9)$$

$$Y_{nm} = \frac{R_{nm}}{R_{ref,m}}. \quad (5.10)$$

Because of the simple fabrication and the associated lower hardware cost, the concept of an external reference channel is implemented in this work. By changing the calculation of X_{nm} and Y_{nm} as derived above, similar procedures can be used for the internal concept. Additionally, a comparison of both concepts by means of a tolerance analysis is discussed in Chapter 7.

The relation between the input and output parameters can be written in matrix form as:

$$\begin{aligned} \begin{pmatrix} Y_{1m} \\ Y_{2m} \\ \vdots \\ Y_{Nm} \end{pmatrix} &= \frac{1}{R_{ref,m}} \begin{pmatrix} R_{1m} \\ R_{2m} \\ \vdots \\ R_{Nm} \end{pmatrix} \\ &= \frac{1}{R_{ref,m}} \begin{pmatrix} C_{11} & C_{12} & \cdots & C_{1N} \\ C_{21} & C_{22} & \cdots & C_{2N} \\ \vdots & \vdots & \ddots & \vdots \\ C_{N1} & C_{N2} & \cdots & C_{NN} \end{pmatrix} \begin{pmatrix} S_{1m} \\ S_{2m} \\ \vdots \\ S_{Nm} \end{pmatrix} \\ &= \frac{S_{ref,m}}{R_{ref,m}} \begin{pmatrix} C_{11} & C_{12} & \cdots & C_{1N} \\ C_{21} & C_{22} & \cdots & C_{2N} \\ \vdots & \vdots & \ddots & \vdots \\ C_{N1} & C_{N2} & \cdots & C_{NN} \end{pmatrix} \begin{pmatrix} X_{1m} \\ X_{2m} \\ \vdots \\ X_{Nm} \end{pmatrix} \\ &= \underbrace{\frac{1}{W_{ref}} \begin{pmatrix} C_{11} & C_{12} & \cdots & C_{1N} \\ C_{21} & C_{22} & \cdots & C_{2N} \\ \vdots & \vdots & \ddots & \vdots \\ C_{N1} & C_{N2} & \cdots & C_{NN} \end{pmatrix}}_{[\hat{C}]} \begin{pmatrix} X_{1m} \\ X_{2m} \\ \vdots \\ X_{Nm} \end{pmatrix}. \end{aligned} \quad (5.11)$$

Here, we can recognize that the new input vector does not depend on the absolute signal S of the calibration sources but only on the relative position of the probe and the receiver elements. So the amplitude and phase deviations between various calibration subsystems can be compensated.

Furthermore, only a scalable version $[\hat{C}]$ of the coupling matrix $[C]$ is determined in this procedure, which can be corrected by dividing the whole matrix by its first coefficient \hat{C}_{11} .

If all M probes are considered, we have

$$\begin{aligned}
 [Y] &= [\hat{C}] [X] & (5.12) \\
 \begin{pmatrix} Y_{11} & Y_{21} & \cdots & Y_{1M} \\ Y_{21} & Y_{22} & \cdots & Y_{2M} \\ \vdots & \vdots & \ddots & \vdots \\ Y_{N1} & Y_{N2} & \cdots & Y_{NM} \end{pmatrix} &= \begin{pmatrix} \hat{C}_{11} & \hat{C}_{12} & \cdots & \hat{C}_{1N} \\ \hat{C}_{21} & \hat{C}_{22} & \cdots & \hat{C}_{2N} \\ \vdots & \vdots & \ddots & \vdots \\ \hat{C}_{N1} & \hat{C}_{N2} & \cdots & \hat{C}_{NN} \end{pmatrix} \begin{pmatrix} X_{11} & X_{12} & \cdots & X_{1M} \\ X_{21} & X_{22} & \cdots & X_{2M} \\ \vdots & \vdots & \ddots & \vdots \\ X_{N1} & X_{N2} & \cdots & X_{NM} \end{pmatrix}.
 \end{aligned}$$

The calibration consists now of determining all N independent row vectors of the coupling matrix $[\hat{C}]$. After re-formulation, we can write for the n^{th} row vector of the coupling matrix

$$\underbrace{\begin{pmatrix} Y_{n1} \\ Y_{n2} \\ \vdots \\ Y_{nM} \end{pmatrix}}_{\vec{y}_n} = \underbrace{\begin{pmatrix} X_{11} & X_{21} & \cdots & X_{N1} \\ X_{12} & X_{22} & \cdots & X_{N2} \\ \vdots & \vdots & \ddots & \vdots \\ X_{1M} & X_{2M} & \cdots & X_{NM} \end{pmatrix}}_{[X]^T} \underbrace{\begin{pmatrix} \hat{C}_{1n} \\ \hat{C}_{2n} \\ \vdots \\ \hat{C}_{Nn} \end{pmatrix}}_{\vec{c}_n}. \quad (5.13)$$

Here, we need to solve an under-determined linear system of N variables with M equations ($N \gg M$). In general, it is impossible without any a-prior knowledge and assumptions regarding the system.

Based on the examination in Chapter 3, only the vector \vec{c}_n of L_n essential coefficients is necessary to be determined in a simplified coupling matrix. The other components of \vec{c}_n are assumed to be 0. The n^{th} problem of the coupling matrix is

$$\underbrace{\begin{pmatrix} Y_{1n} \\ Y_{2n} \\ \vdots \\ Y_{Mn} \end{pmatrix}}_{\vec{y}'_n} = \underbrace{\begin{pmatrix} X_{l_1,1} & X_{l_2,1} & \cdots & X_{l_{L_n},1} \\ X_{l_1,2} & X_{l_2,2} & \cdots & X_{l_{L_n},2} \\ \vdots & \vdots & \ddots & \vdots \\ X_{l_1,M} & X_{l_2,M} & \cdots & X_{l_{L_n},M} \end{pmatrix}}_{[X']^T} \underbrace{\begin{pmatrix} C_{l_1,n} \\ C_{l_2,n} \\ \vdots \\ C_{l_{L_n},n} \end{pmatrix}}_{\vec{c}'_n}. \quad (5.14)$$

After all vector \vec{c}'_n have been solved independently, the coupling matrix $[C]$ as well as the transform function \mathbf{T} in 5.2 can be reconstructed.

Furthermore, a Least Square (LS) approach is the standard method to solve (5.14). In order to improve its accuracy, we will discuss two additional signal processing concepts, namely the Principle Component Analysis (PCA) and the extension with Multiple Reference Receivers (MRR). Whilst the PCA uses much higher computational complexity, the MRR demands more reference channels and hardware cost.

5.2.2 Least-Square (LS) Method

As proven above, the under-determined problem of N variables ($N > M$) in 5.13 is rewritten into the over-determined problem of L variables ($L < M$) in 5.14. Thus, with the assumption of an accurate model matrix $[X']$, the Least-Square method can be used to solve this problems as

$$\vec{c}_n = \left([X'] [X']^T \right)^{-1} [X'] \vec{y}'_n. \quad (5.15)$$

This solution is estimated by Maximum-Likelihood method. Its accuracy is achieved only with a sufficient SNR as well as an adequate ratio $\frac{M}{L}$.

5.2.3 Principle Component Analysis (PCA)

In case of calibration signals with high SNR, the concept of the Principle Component Analysis can be applied to reduce the required number of probes (lower $\frac{M}{L}$) whilst still maintaining the calibration accuracy.

The algorithm can be summarized as follows:

- The covariance matrix of the measurement vector \vec{y}'_n is calculated as

$$[Cov] = \vec{y}'_n \vec{y}'_n^H. \quad (5.16)$$

- The eigenvalue decomposition method is applied to determine the signal and the noise subspace, denoted by subscripts S and N respectively. This yields

$$[Cov] = [[E]_S [E]_N] [\Delta] [[E]_S [E]_N]^H, \quad (5.17)$$

$$[\Delta] = \begin{pmatrix} \Delta_1 & \cdots & 0 & 0 & \cdots & 0 \\ \vdots & \ddots & \vdots & \vdots & \ddots & \vdots \\ 0 & \cdots & \Delta_L & 0 & \cdots & 0 \\ 0 & \cdots & 0 & \Delta_{L+1} & \cdots & 0 \\ \vdots & \ddots & \vdots & \vdots & \ddots & \vdots \\ 0 & \cdots & 0 & 0 & \cdots & \Delta_M \end{pmatrix} \quad (5.18)$$

$$\text{with } \underbrace{\Delta_1 > \cdots > \Delta_L}_{\tilde{\Delta}_S} > \underbrace{\Delta_{L+1} > \cdots > \Delta_M}_{\tilde{\Delta}_N},$$

$$[E] = \begin{pmatrix} E_{11} & \cdots & E_{1L} & E_{1,L+1} & \cdots & E_{1M} \\ E_{21} & \cdots & E_{2L} & E_{2,L+1} & \cdots & E_{2M} \\ \vdots & \ddots & \vdots & \vdots & \ddots & \vdots \\ E_{M1} & \cdots & E_{ML} & E_{M,L+1} & \cdots & E_{MM} \end{pmatrix}. \quad (5.19)$$

$\underbrace{\hspace{10em}}_{[E]_S} \quad \underbrace{\hspace{10em}}_{[E]_N}$

Here, $\vec{\Delta}$ and $[E]$ are the eigenvalues and the corresponding eigenvectors of the subspace. Because of L essential coefficients of the vector \vec{c}_n , the L largest eigenvalues $\Delta_1 > \dots > \Delta_L$ belong to the signal subspace whilst the other correspond to the noise subspace.

- Due to the fact that the noise subspace is orthogonal to the signal subspace, an additional linear system can be written in case of low noise and high SNR. It reads

$$\underbrace{\begin{pmatrix} 0 \\ 0 \\ \vdots \\ 0 \end{pmatrix}}_{\vec{0}} = \underbrace{\begin{pmatrix} E_{1,L+1}^* & \cdots & E_{M,L+1}^* \\ E_{1,L+2}^* & \cdots & E_{M,L+2}^* \\ \vdots & \ddots & \vdots \\ E_{1M}^* & \cdots & E_{MM}^* \end{pmatrix}}_{[E]_N^H} \underbrace{\begin{pmatrix} X_{1l_1} & X_{1l_2} & \cdots & X_{1L} \\ X_{2l_1} & X_{2l_2} & \cdots & X_{2L} \\ \vdots & \vdots & \ddots & \vdots \\ X_{Ml_1} & X_{Ml_2} & \cdots & X_{ML} \end{pmatrix}}_{[X]^T} \underbrace{\begin{pmatrix} C_{nl_1} \\ C_{nl_2} \\ \vdots \\ C_{nL} \end{pmatrix}}_{\vec{c}_n}. \quad (5.20)$$

- Combining (5.14) and (5.20) yields the larger linear system

$$\vec{y}'_{new,n} = [Z] \vec{c}_n \quad (5.21)$$

with

$$\vec{y}'_{new,n} = (Y_{1n}, \dots, Y_{Mn}, 0, \dots, 0)^T, \quad (5.22)$$

$$[Z] = \begin{pmatrix} 1 & \cdots & 0 \\ \vdots & \ddots & \vdots \\ 0 & \cdots & 1 \\ E_{1,L+1}^* & \cdots & E_{M,L+1}^* \\ \vdots & \ddots & \vdots \\ E_{1M}^* & \cdots & E_{MM}^* \end{pmatrix} \begin{pmatrix} X_{1l_1} & \cdots & X_{1L} \\ \vdots & \ddots & \vdots \\ X_{Ml_1} & \cdots & X_{ML} \end{pmatrix}. \quad (5.23)$$

So, we have more linear equations for the same number of L variables. Their solution is estimated by means of a Least-Square method from

$$\vec{c}_n = \left([Z]^T [Z] \right)^{-1} [Z]^T \vec{y}'_{new,n}, \quad (5.24)$$

which yields higher accuracy.

In comparison to the LS method, a larger SNR of the calibration signals is necessary here to satisfy (5.20). Furthermore, the eigenvalue decomposition comes always with a higher computational complexity.

5.2.4 Extension with Multiple reference receivers (MRR)

In the above discussion, measurements with high SNR and low noise are demanded for the calibration systems. Two main kinds of noise are noted in the calibration procedure: modeling errors of

the probe-receiver coupling and additive measurement noise. The latter can be reduced by longer measurement time and higher power of the calibration signal whilst the modeling errors decrease with the number of calibration probes, which is limited in practical systems. Another possibility is the diversification of the modeling errors via multiple reference channels distributed between the probes and the receivers.

The extended calibration procedure is sketched in Fig. 5.3. Firstly, all P reference channels, numbered as channel $N + 1$ to channel $N + P$, are assumed to be isolated from each other and also from the other receiver channels. Thus, the procedure proposed in Chapter 4 can be applied to calibrate the deviations of all reference channels. The relative channel coefficient R_p of the $(N + p)^{\text{th}}$ channel normalized to channel $N + 1$ is determined as

$$\begin{aligned} \|R_p\|_{\text{dB}} &= \frac{1}{M} \sum_{m=1}^M 20 \log_{10} \left(\frac{Y_{N+p,m}}{Y_{N+1,m}} \cdot \frac{K_{N+1,m}}{K_{N+p,m}} \right), \\ \angle(R_p) &= \frac{1}{M} \sum_{m=1}^M \angle \left(\frac{Y_{N+p,m}}{Y_{N+1,m}} \cdot \frac{K_{N+1,m}}{K_{N+p,m}} \right) + k \cdot \frac{2\pi}{M}, \text{ with } k = 0, \dots, (M - 1). \end{aligned} \quad (5.25)$$

A discussion about the right choice of k is given in (4.26) of Chapter 4.

As a result of (5.14) and (5.25), a new system of linear equations can be derived as

$$\begin{pmatrix} \vec{y}_{n,1} \\ R_2 \cdot \vec{y}_{n,2} \\ \vdots \\ R_P \cdot \vec{y}_{n,P} \end{pmatrix} = \begin{bmatrix} \mathbf{X}_1 \\ \mathbf{X}_2 \\ \vdots \\ \mathbf{X}_P \end{bmatrix} \vec{c}_n \quad (5.26)$$

with the subscript (n, p) denoting the n^{th} receiver normalized to the $(N + p)^{\text{th}}$ reference channel. Therefore, both the LS and the PCA method can be applied to solve the new linear equation system in (5.26).

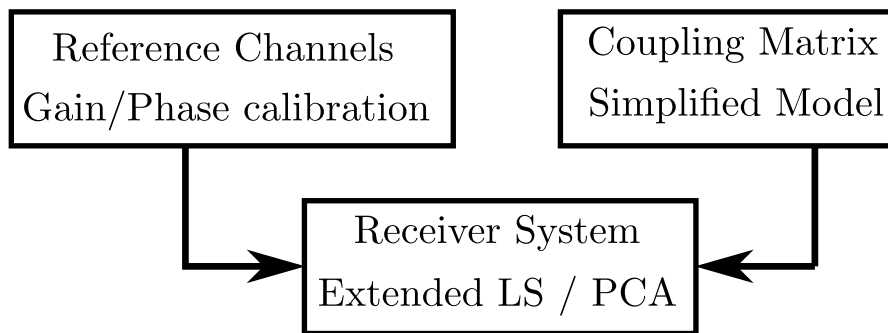


Figure 5.3: Calibration scheme with multiple reference receiver channels.

5.3 Simulation

Simulation in MATLAB is performed for a 8×8 planar receiver array to validate the various calibration procedures. In order to focus only on the applicability of the proposed algorithms, the radiation characteristic of receiver elements is assumed to be omni-directional. Thus, the coupling between the m^{th} monopole probe and the n^{th} receiver antenna at distance d_{nm} can be determined approximately in the simulation as

$$K_{nm} = \frac{1}{d_{nm}} \exp\left(-j2\pi \frac{d_{nm}}{\lambda}\right) \quad (5.27)$$

with λ being the signal wavelength.

A planar array with brick architecture, the coupling matrix of which is illustrated in Fig. 5.4, is examined. This means, channel deviation and coupling between adjacent channels within a linear array are the main error sources. Furthermore, the mutual coupling is estimated to be -18 dB for adjacent antennas and -20 dB for further elements. On the other side, a far-field source at the broad-side ($\theta = 90^\circ$) is used to verify the accuracy of the different proposed calibration procedure. The radiation patterns of the uncalibrated array and the calibrated system with 16 probes are shown

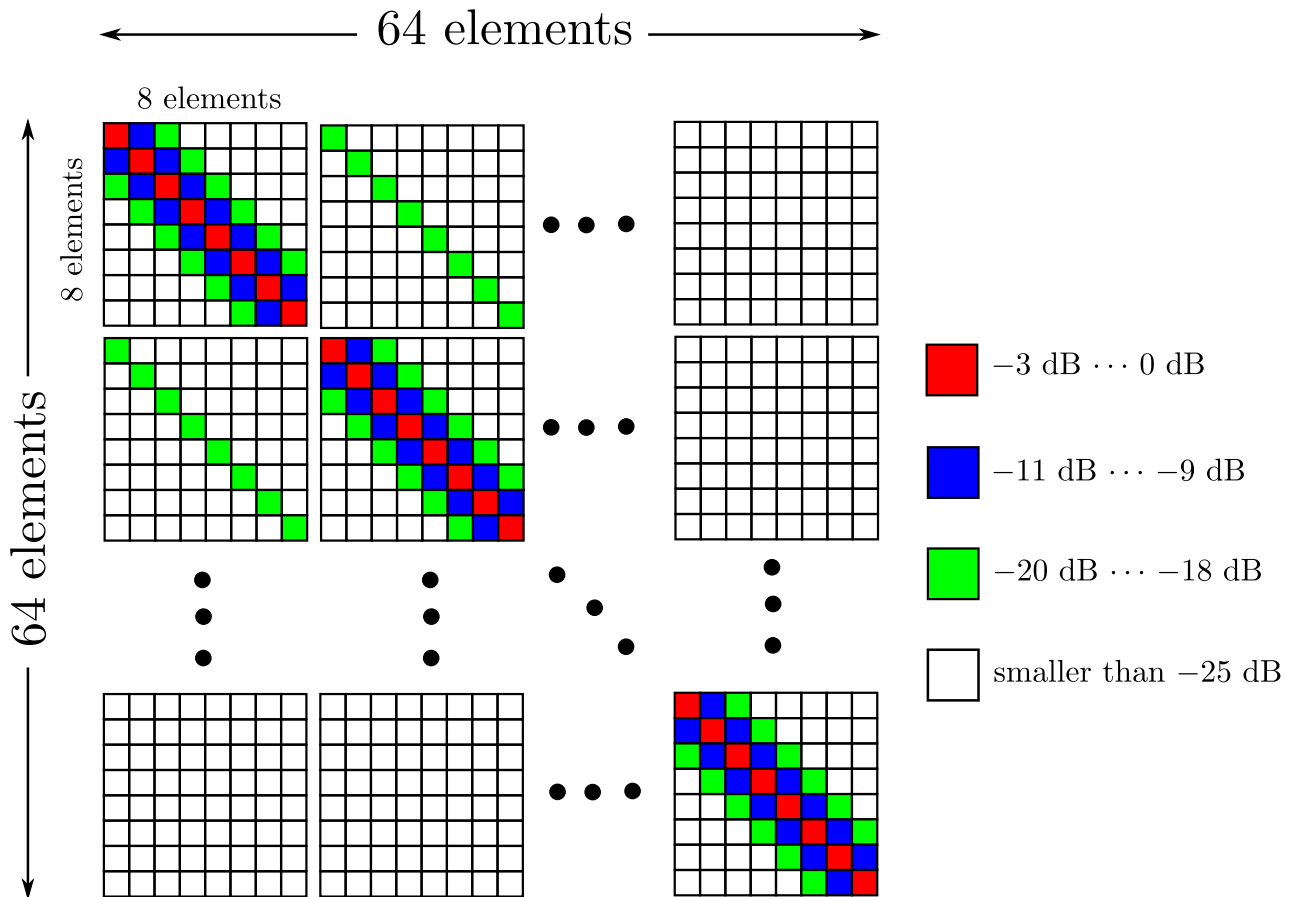


Figure 5.4: Example of a 8×8 array with brick architecture: coupling matrix

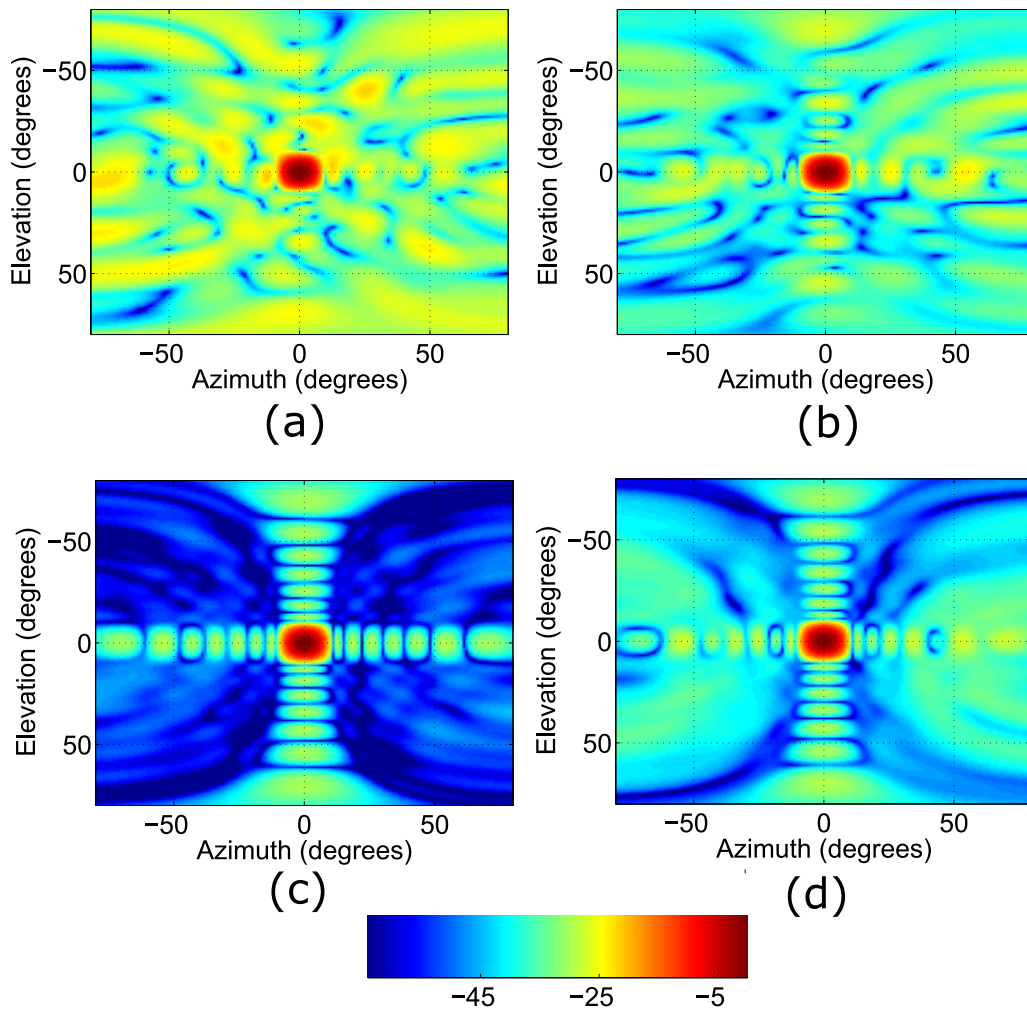


Figure 5.5: Radiation pattern of a receiver array calibrated with 16 probes: (a) without calibration and calibration with (b) one, (c) two, and (d) three mutual coupling coefficients

in Fig. 5.5. The amplitude tapering with Chebyshev function [16] is chosen to achieve the side-lobe level of -30 dB in the ideal case.

In comparison with the pattern of the uncalibrated array in Fig. 5.5(a), a significant decrease of the side-lobe level is observed in that of the calibrated array depicted in Fig. 5.5(c). Additionally, the calibration accuracy decreases when under- or overestimating the number of significant coupling coefficients as illustrated in Fig. 5.5(b) and Fig. 5.5(c), respectively. The same result is also depicted in Fig. 5.7(b), which shows the radiation patterns at the elevation angle of 0° . This statement underlines the need of a prior knowledge of the receiver system.

Fig. 5.6 reports the radiation pattern of the receiver array calibrated with only 8 probes. In case of the underestimated model of the coupling matrix, the calibrated pattern depicted in Fig. 5.6(a) differs only slightly in comparison with Fig. 5.5(b). In contrast, the calibrated pattern degrades significantly

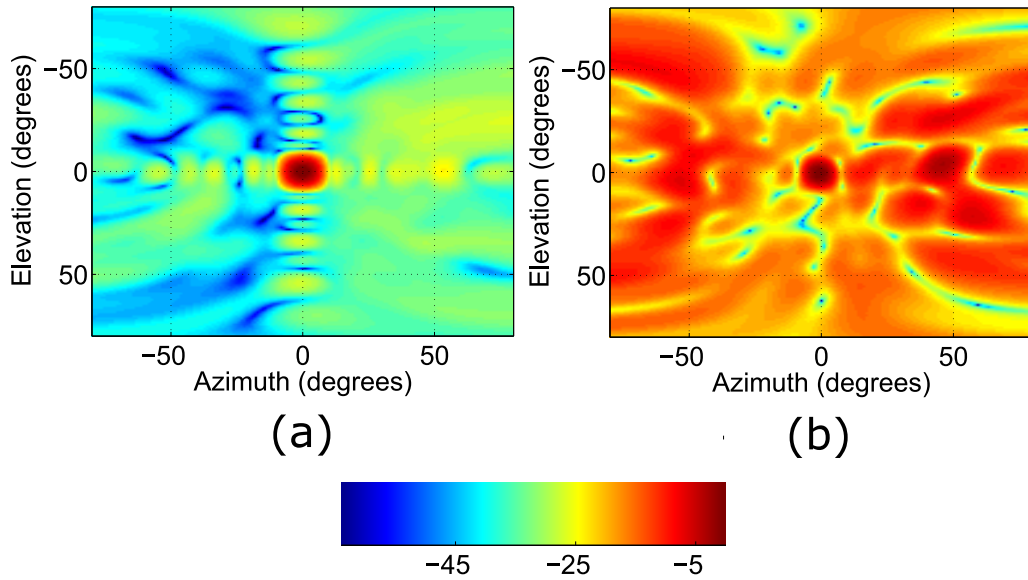


Figure 5.6: Radiation pattern of a receiver array calibrated with 8 probes: (a) one and (b) two mutual coupling coefficients.

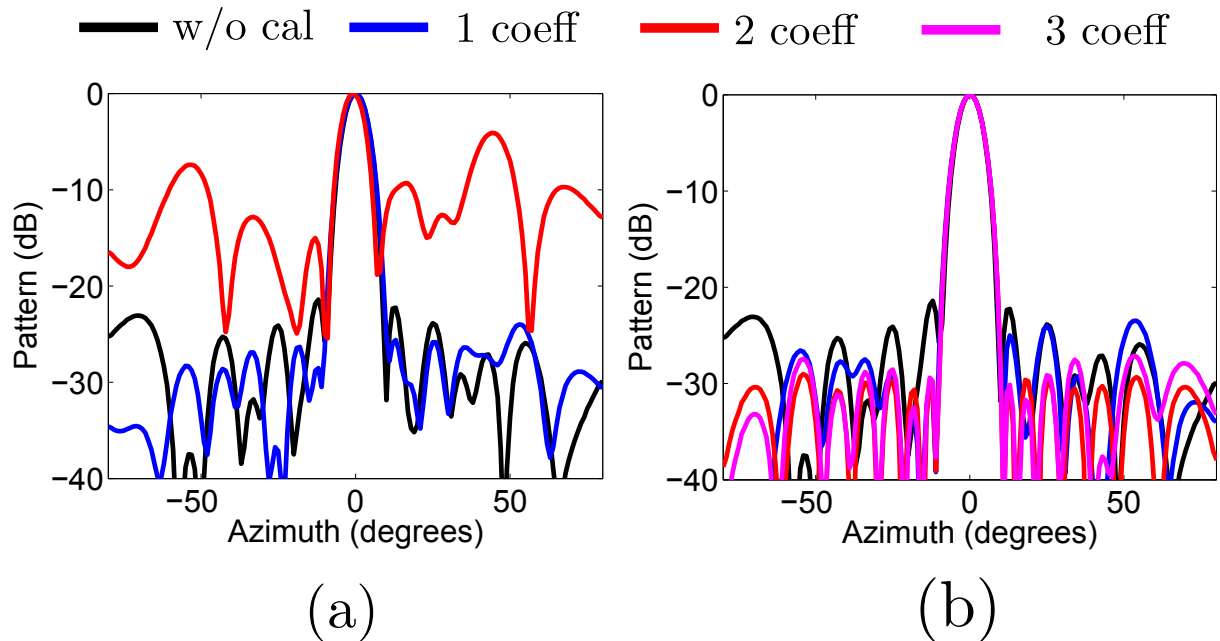


Figure 5.7: Radiation pattern of receiver array with Tschebyscheff window of -30dB side-lobe level at the elevation angle of 0° : calibration with (a) 8 probes and (b) 16 probes.

for the coupling matrix model with two essential coupling coefficients as illustrated in Fig. 5.5(c) and Fig. 5.6(b). This observation emphasizes the requirement of not only high SNR measurements but also a sufficient number of probes to achieve high calibration accuracy.

5.4 Summary

The joint calibration of the channel deviations and the mutual coupling is the main theme of this chapter. The calibration problem is firstly formulated mathematically as calculation of the coupling matrix. Furthermore, a simplified model instead of the full coupling matrix, is considered based on the characteristics of the mutual coupling in real receiver systems. This step leads to the sparseness of the computational effort and hardware cost in the calibration system as well as to an improvement of the calibration accuracy.

In the next step, a calibration procedure is proposed and three different decoupling algorithms, namely Least-Square, Principle Component Analysis, and Extension with Multiple Reference Receivers, are discussed, taking into account various aspects.

The Least Square method relies on the Maximum-Likelihood criterion. This means, a sufficient SNR of the calibration signals as well as a large number of probes are required for a highly accurate calibration.

In order to improve the calibration accuracy, the procedure with PCA is proposed for a given maximum number of calibration probes. The hardware cost is thereby kept nearly unchanged. The main drawback is, however, the higher demand of SNR and the accuracy of the probe-receiver-coupling model. Because its degradation with increased distance between the calibration probe and the receiver, the realizable SNR of the calibration signals is limited by the size of the receiver system. The second disadvantage of this method is its huge computational complexity. Hence, this approach is more suitable for small arrays, which is demonstrated in Chapter 6.

The last proposed procedure demonstrates the best accuracy at the expense of additional hardware cost for the multiple reference receivers. Not only a higher SNR is achieved but the errors due to an insufficiently accurate coupling-model can also be decreased by means of diversifying the reference channels.

Last but not least, simulation is performed to validate the usefulness of the proposed calibration procedures. The necessity of a simplified coupling matrix because of the limited hardware of the on-board calibration system is illustrated.

6 Experiments

Experiments with linear and planar patch arrays are performed to validate the applicability of the calibration concepts proposed in Chapter 4 and Chapter 5, and their results are reported in this chapter.

Firstly, the set-ups of the measurements are described in Section 6.1. Additionally, a printed and a coaxial probe, which are shown in Fig. 4.2 in Chapter 4, are fabricated and used as calibration probes in the experiments.

The experimental results with the printed probe are reported in Section 6.2, those of the coaxial probe in Section 6.3. Thereby, the calibration not only of the channel factors but also of the simplified coupling matrix are discussed. Finally, the trade-off between system complexity and calibration accuracy is summarized in Section 6.4.

6.1 Measurement Setup

A linear 7x1- and a planar 4x4 antenna array are fabricated in a multi-layer structure as depicted in Fig. 6.1. However, to validate the concept, only four patches are operated as a receiver array simultaneously. The others are terminated with 50Ω resistances. Furthermore, a four-port network analyzer R&S ZVA50 is connected to the antenna structure and used as a four-channel receiver.

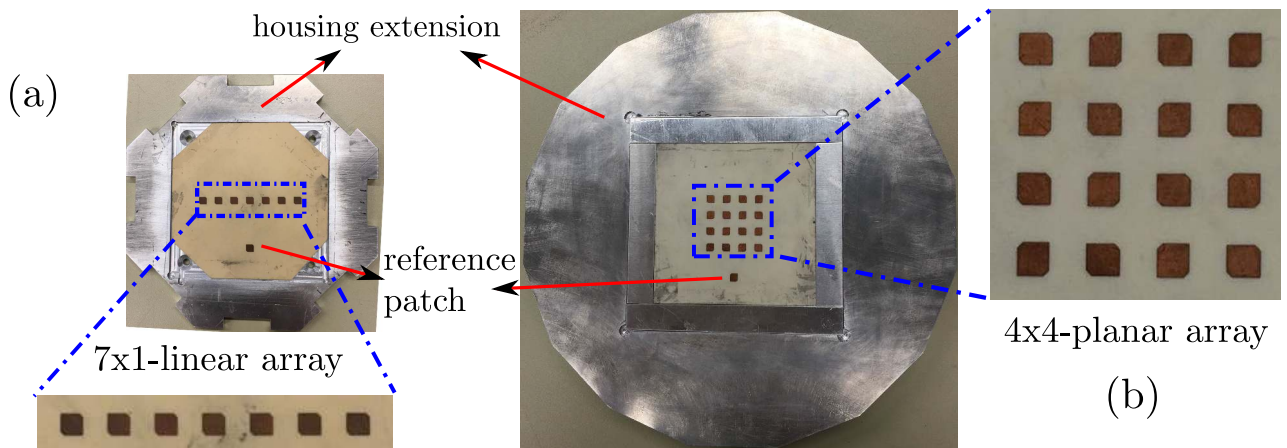


Figure 6.1: Fabricated patch receiver arrays: (a) 7x1 linear array and (b) 4x4 planar array.

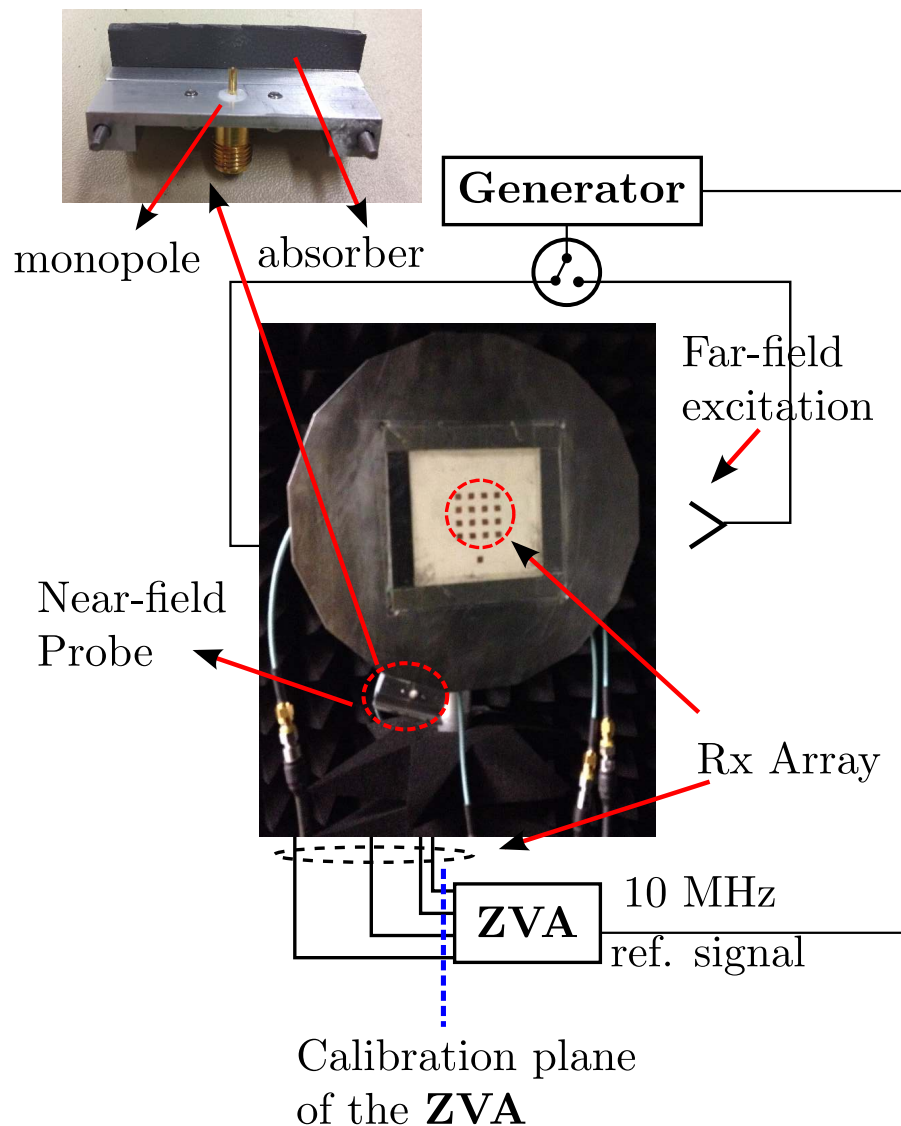


Figure 6.2: Measurement setup of the planar array with the near-field calibration setup.

The calibration signals are provided by an external signal generator Anritsu MG37020A which is synchronized through a 10 MHz reference signal from the R&S ZVA50. A single near-field probe is used in the experiments. Its position is changed manually, in order to emulate multiple calibration probes. An effective permittivity of $\epsilon_r = 1.03$ is determined by means of HFSS simulation. Measurements with far-field excitation at boresight are used to validate the calibration accuracy. The measurement set-up is sketched in Fig. 6.2.

6.2 Microstrip Probe

In this experiment, the microstrip printed probe with a reflector behind it, which is described in Chapter 4, is used. Despite its complicated structure, the radiation pattern of the probe in the H-plane is firstly assumed to be omni-directional in the decoupling algorithm. Furthermore, a generic model of the receiver patch is applied. To validate the calibration concept, a linear array of only 3 antennas is used in the measurements, whilst the other patches are terminated with $50\text{-}\Omega$ resistances. Furthermore, $M = 8$ probe positions are applied to calibrate the mutual coupling of adjacent receiver channels.

Three measurements are performed in the anechoic chamber. The R&S ZVA50 is not calibrated in the first measurement while a SOLT (Short-Open-Load-Through) calibration is applied to the network analyzer in the second and the third one. Because of the uncalibrated ZVA in the first measurement, the coupling between the reference channel and the receiver array still exists. Additionally, the power of the calibration signals used in the third measurement is 15 dB higher than those in the first and the second one. The results are depicted in Fig. 6.3.

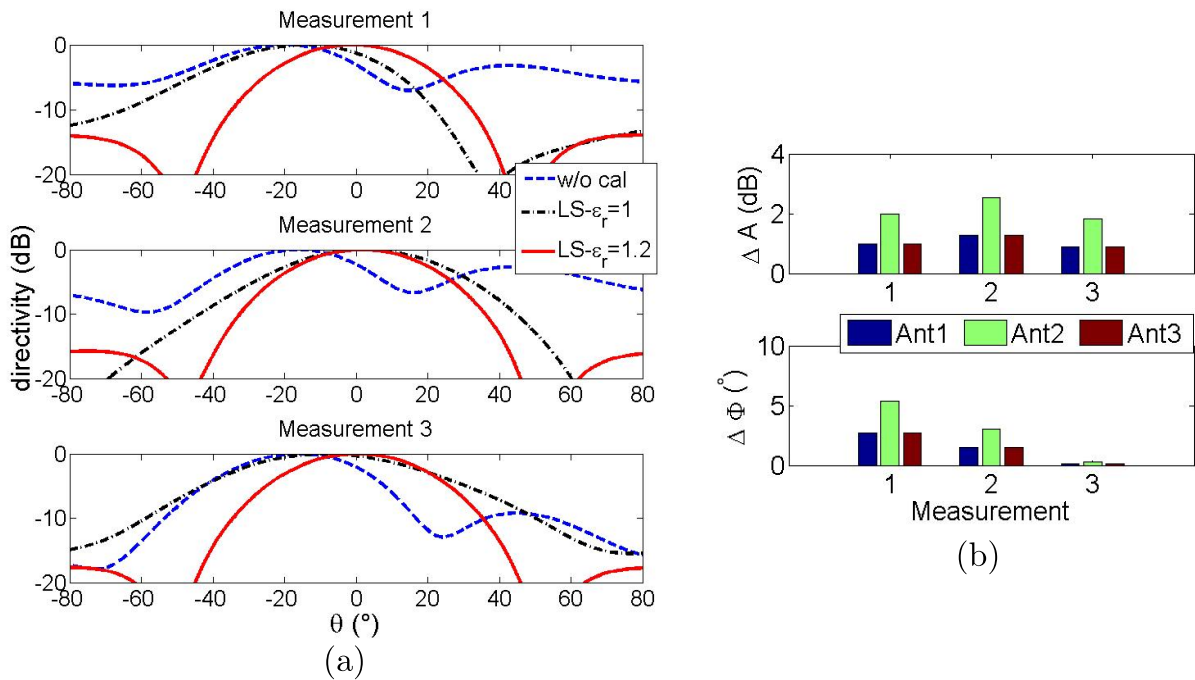


Figure 6.3: Measurement results of a three-patch linear array: (a) Radiation pattern at 20 GHz (blue) before and after calibration with (black) $\epsilon_r = 1$ and (red) $\epsilon_r = 1.2$ for (top) measurement 1, (middle) 2, and (bottom) 3 respectively. (b) (top) Amplitude and (bottom) phase deviations of the array after calibration in all three measurements.

The pointing error of the linear array after applying the external calibration procedure is corrected in all measurements. In comparison with the calibrated results assuming $\epsilon_r = 1$ (free space), a sig-

nificant increase of the pointing accuracy as well as a decrease of the side-lobe level in the radiation pattern are observed with the effective permittivity $\epsilon_r = 1.2$. This effective permittivity, which is different from that shown in Chapter 4, is determined by simulation and includes the impact of the metallic reflector. Besides, a decrease of the phase deviation is also observed from the first to the third measurement as depicted in Fig. 6.3(b). Thus, the requirements of an isolated reference channel and high SNR are thereby emphasized.

On the other side, the calibration accuracy is, however, limited due to the model simplification of the probe-receiver coupling. The amplitude deviations stay still above 2 dB in all three measurements. As a result, the side-lobe level in the third measurement is -18 dB instead of -13 dB in case of an ideal array. This underlines the need of model improvements for the probe-receiver coupling to enhance the calibration accuracy.

6.3 Coaxial Probe

In order to improve the analytical model of the probe-receiver coupling, two aspects are taken into account: (1) a model enhancement of the receiver element as well as (2) an alternative probe design. The first measure corresponds to a new analytical model of the patch pattern at the off-side. As proposed in Chapter 4, the patch pattern of the Fourier-based model is well-matched to that of the HFSS simulation.

The first point involves another aspect. Indeed, improving the model of the probe radiation pattern is limited by the complexity of the probe structure itself. Regarding the microstrip probe, it is not feasible and demands a high computational effort to synthesize a good and simple analytical model of the probe-receiver coupling for all elements of a large array. Thus, redesigning the monopole probe is the second approach to produce an omni-directional radiation pattern in the H-plane. As discussed in Chapter 4, the coaxial probe together with the absorber instead of a metallic reflector behind it is suggested to be used in the experiments.

Two situations are examined now to prove the usefulness of the proposed coaxial probe, namely the calibration of only channel fluctuations as well as jointly with mutual coupling.

6.3.1 Calibration of Channel Fluctuations

The receiver systems are, in most applications, characterized in a measurement chamber. All systematic errors such as position deviation of patches or channel cross-talk can be figured out and corrected with this procedure. On the other side, the channel fluctuations caused by environmental changes are calibrated with the on-board calibration system.

In order to replicate this situation, the network analyzer is first calibrated by means of a SOLT calibration to minimize the mutual coupling between receiver channels. Additionally, the coupling

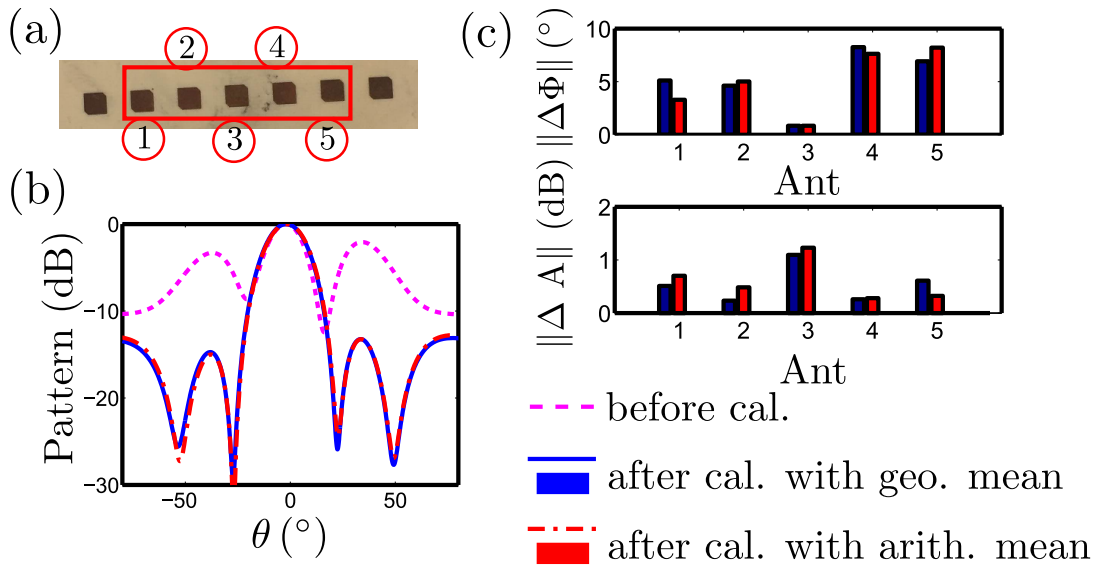


Figure 6.4: Calibration of a five-patch linear array with eight probes: (a) linear array and (b) its radiation pattern before and after calibration as well as (c) the amplitude and phase fluctuations of the calibrated receiver channels.

between adjacent antennas is negligible as shown in the simulation in Chapter 4. Due to different cable lengths and connectors, amplitude and phase errors are observed in various channels.

A five-patch linear array with eight coaxial probes is firstly examined in a small measurement chamber to minimize the disturbing effect of the environment on the calibration accuracy. Furthermore, two different averaging methods are considered in the calibration procedure, namely the geometric mean (GeoMean) and the arithmetic mean (ArithMean). The measurement results are reported in Fig. 6.4.

Because of the sufficient SNR of the calibration measurements with signal powers of 20 dBm and a high number of probes, the two averaging methods demonstrate similar results. Whilst the phase errors are below 9° , a maximum amplitude deviation of about 1 dB is observed.

In the next experiments, the 4x4 planar receiver array is considered. All measurements are still performed in the measurement chamber. Besides the two different averaging methods, three different patch models are examined, namely the isotropic model (M1) from [44], the generic model (M2) from [50], and the proposed Fourier-based model (M3).

In the first experiment, the four antennas 1, 4, 13, and 16 at the corners of the array are considered. Whilst an amplitude deviation of less than 0.5 dB are observed, large phase errors of more than 120° are detected in the received signals. After calibration by means of the proposed concept with 16 probe positions, the signals are significantly improved and phase errors below 5° are demonstrated (see Fig. 6.5(b)). In comparison to that of the geometric mean, larger amplitude errors of up to 0.5 dB are documented in Fig. 6.5(c) for the calibration procedure with the arithmetic mean, whilst a

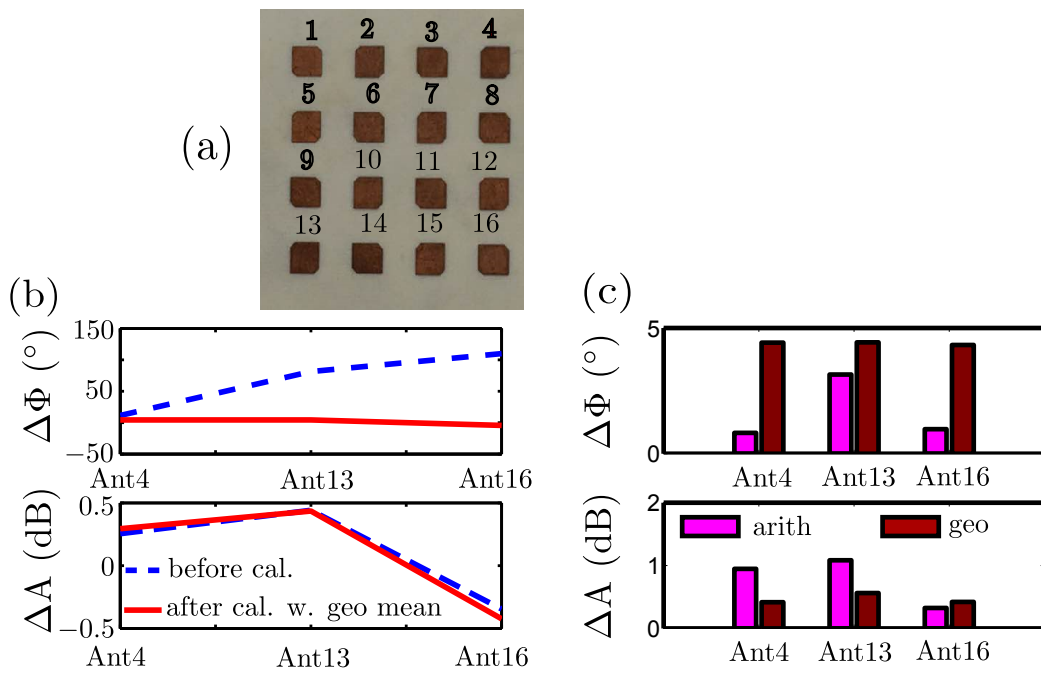


Figure 6.5: (a) 4x4 planar array used in the experiments in the measurement chamber and amplitude and phase errors of array elements 4, 13, and 16 with respect to element 1 (b) before and after calibration with geometric mean as well as (c) after calibration with geometric and arithmetic mean.

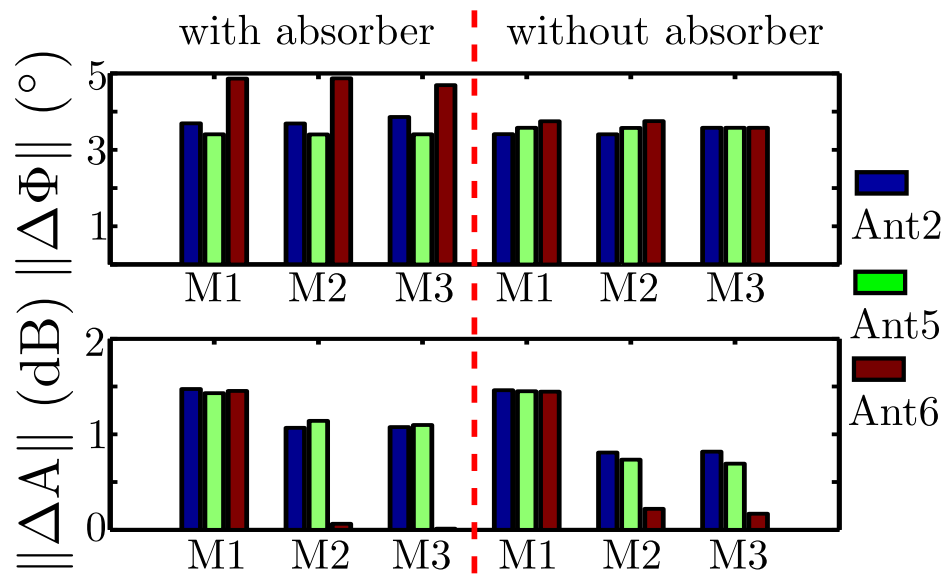


Figure 6.6: Amplitude and phase errors of array elements 2, 5, and 6 with respect to element 1 after calibration by means of monopole probes with and without absorber for three patch-receiver coupling models: the isotropic model (M1) from [44], the generic model (M2) from [50], and the proposed Fourier-based model (M3).

slight enhancement of only 1° is achieved for the phase accuracy. Additionally, due to the circular symmetry of the four antennas, the same calibration results are achieved with all three patch models. In the second experiment, the four antennas 1, 2, 5, and 6 are examined. Due to the asymmetry of the receiver positions, the three patch models yield different calibration results. As depicted in Fig. 6.6,

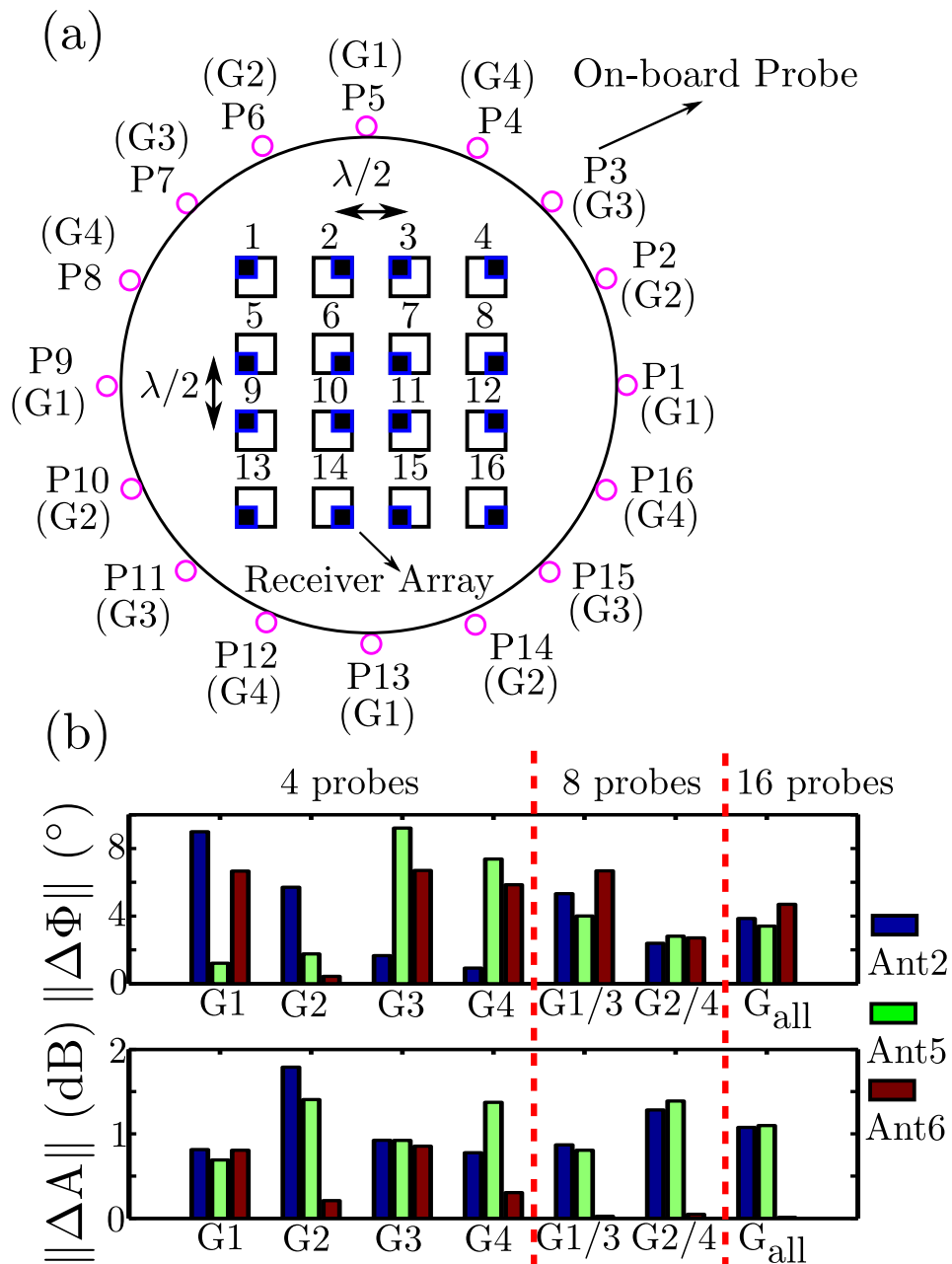


Figure 6.7: (a) Schematic of four groups G1, G2, G3, and G4 of 16 probes and (b) amplitude and phase errors of array elements 2, 5, and 6 with respect to element 1 after calibration with the M3 model of the patch-receiver coupling as a function of the number of probes.

whilst a phase error below 3° is observed for all three models, the amplitude deviation drops from 1.5dB with model M1 to 0.8dB with model M3. Furthermore, the accuracy degradation due to the presence of the absorber is only 1.5° in phase and 0.3dB in amplitude as shown in Fig. 6.6. This demonstrates a good trade-off between the calibration accuracy and the simplicity of the model.

In the third experiment, the 16 probes are divided into four groups G_k of four probes P_{4l+k} with $k = 1, \dots, 4$ and $l = 0, \dots, 3$ (see Fig. 6.7(a)). While the relative positions of the four probes within each group are the same, they rotate by an angle of 22.5° from G1 to G4. As depicted in Fig. 6.7, the total error of all three receiver models decreases with a higher number of probes because of the noise reduction caused by averaging.

On the other side, the sensitivity of the coupling model depends strongly on the relative position of the probe with respect to the patch. This effect together with fabrication uncertainties leads to the result, that the various probe groups yield a different calibration accuracy for each receiver model. A highly accurate result is achieved for antenna 2 with the four-probe group G4. The phase error is reduced from 3° (with 16 probes) to less than 1.5° . The same results are observed in case of

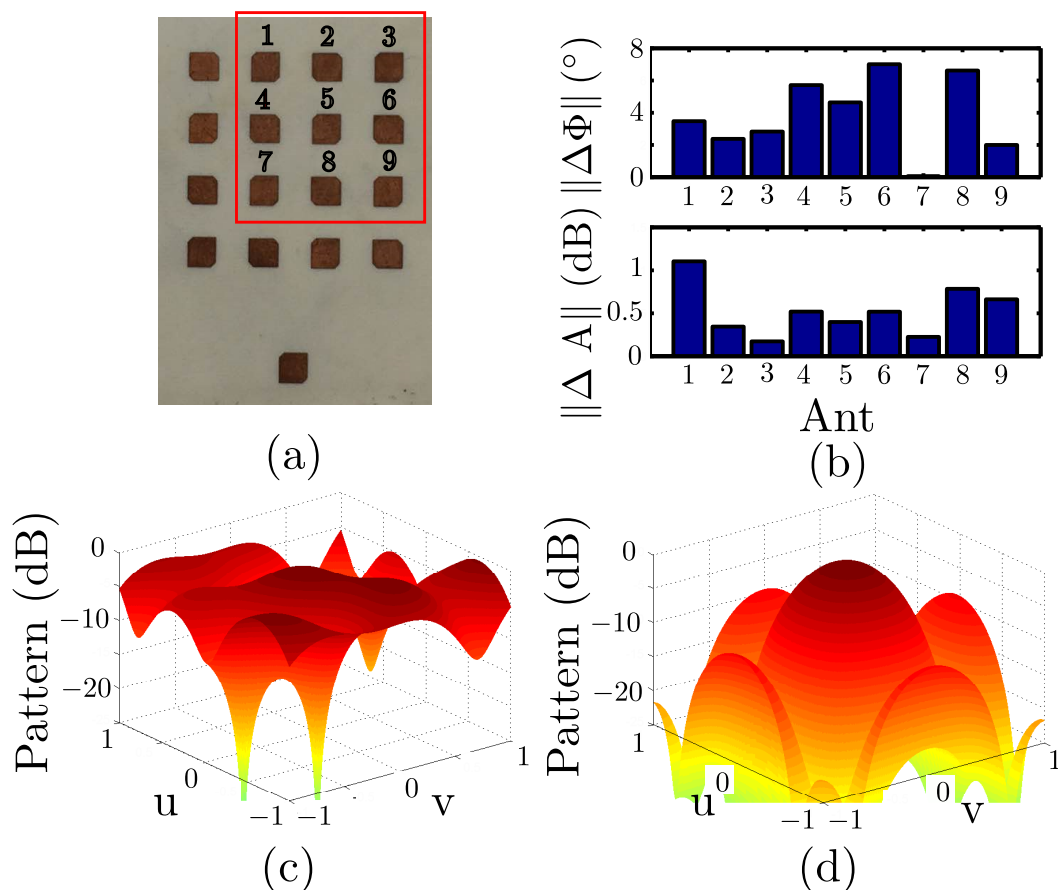


Figure 6.8: 3x3 Planar array: (a) configuration, (b) amplitude and phase deviation of the array elements after calibration as well as beam pattern (c) before and (d) after calibration

antenna 5 and antenna 6 with the probe group G1 and G2, respectively. This observation suggests that, instead of averaging all calibration results, a proper probe selection for the different receiver elements allows to improve the accuracy and the robustness of the calibration procedure.

Last but not least, the proposed calibration procedure is applied to the 3x3 planar array outside the measurement chamber to verify its applicability under more realistic conditions. The number of probes is set to 16. Compared to the beam pattern before calibration, a significant improvement is illustrated in the pattern after calibration as depicted in Fig. 6.8. The direction of the main beam can be correctly detected. On the other side, higher modeling uncertainty, such as from multi-reflections caused by objects in the laboratory, is observed in this experiment. As a result, the side-lobe level of the calibrated pattern stays still above -10 dB, instead of -13 dB of an ideal pattern, which corresponds to a maximum amplitude deviation of 1 dB and a maximum phase error of 7° . This observation underlines the need of calibration signals with high SNR as well as a sufficient number of calibration probes.

6.3.2 Joint Calibration of Channel Fluctuations and Mutual Coupling

Receiver arrays are constructed from various modules with similar design. Thus, an a-priori knowledge of the system and the structure of its coupling matrix can be determined by means of an offline calibration of sample modules. In this case, not only the channel factors but also the mutual coupling between the receivers deviate. The proposed joint calibration procedure of these two error aspects

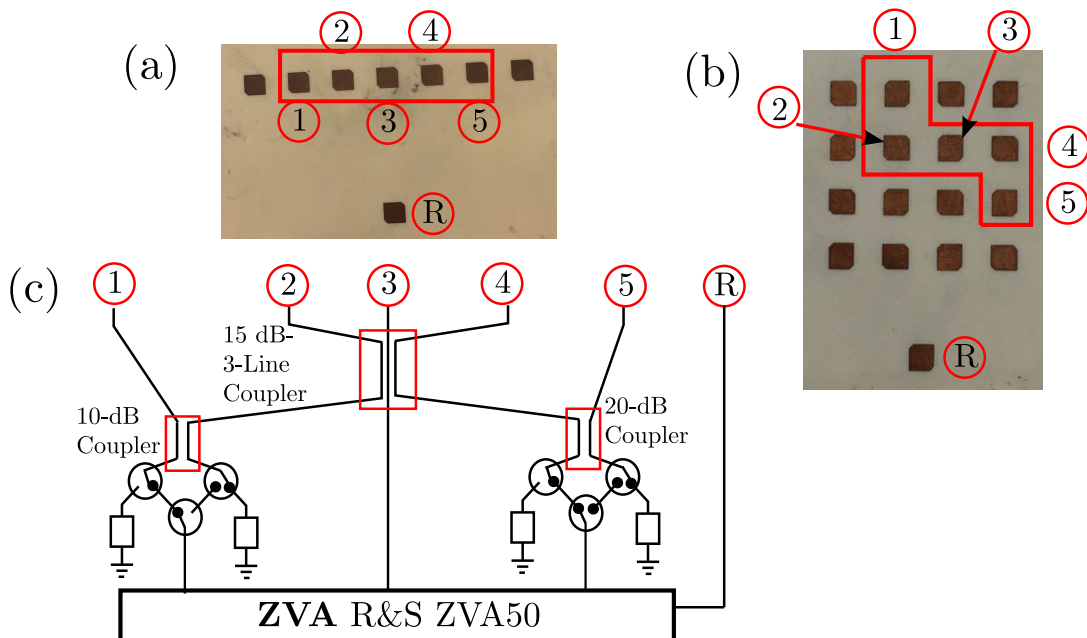


Figure 6.9: Arrays of 5 patches: (a) linear array in the first experiment and (b) a sparse configuration of a planar array in the second experiment as well as (c) the switch matrix.

are verified in the following experiments. Additionally, the M3-model of the probe-receiver coupling is applied.

In the first experiment, a 7×1 linear planar array of patch antennas is built. However, only 5 patches connected with a switch matrix, as shown in Fig. 6.9(a) and Fig. 6.9(c) respectively, are operated as a receiver array simultaneously. Besides, additional patches are used as reference channels. The others are terminated with 50Ω resistances. Furthermore, a vector network analyzer R&S ZVA50 is connected to the other side of the switch matrix and used as the active part of the receiver system. In order to improve the isolation of the reference channels, the network analyzer is first calibrated through the SOLT calibration method. Besides, all measurements are performed in the measurement chamber to achieve the highest possible SNR.

Additionally, four different calibration algorithms are examined in this experiment, namely C_f , C_r , $C_{f,pca}$ and $C_{r,pca}$. Whilst the subscript *pca* refers to the application of the PCA method, *f* and *r*

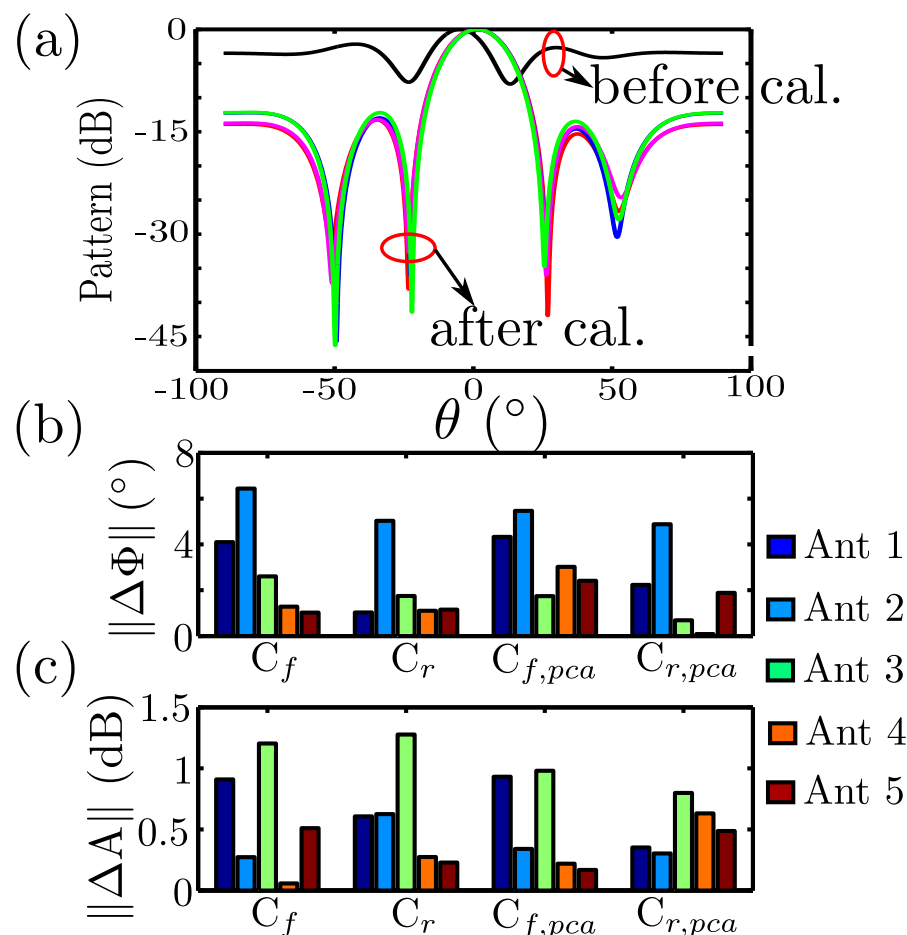


Figure 6.10: Experimental results of a 5×1 linear array calibrated with 16 near-field monopole probes: (a) radiation patterns as well as (b) phase and (c) amplitude deviations of calibrated signals.

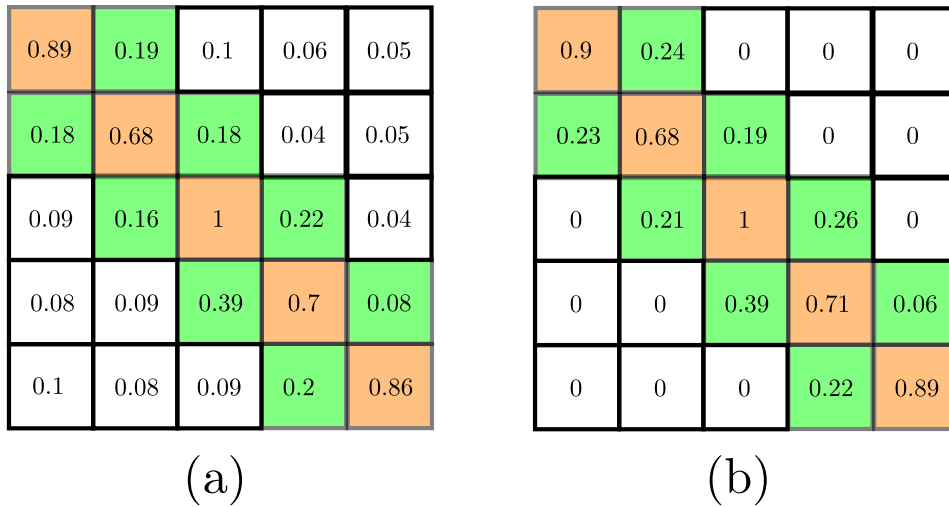


Figure 6.11: Magnitude of the calculated coupling matrix of a 5x1 linear array: (a) a full coupling matrix C_f and (b) a simplified coupling matrix C_r .

denote the determination of a full and a simplified coupling matrix, respectively.

As depicted in Fig. 6.10, the direction of the main beam is corrected by the proposed calibration procedure. In addition a side-lobe level of roughly -13 dB is observed in all calibrated patterns. Phase errors below 7° as well as amplitude deviations of less than 1.5 dB are achieved for all proposed algorithms. Due to the high SNR (transmit power of 20 dBm and measurement bandwidth of 10 Hz) and low modeling errors (center location of the receiver array and high probe/receiver ratio of 16/5), only slight accuracy improvements are demonstrated in the algorithm C_r in comparison to C_f . The magnitude of the full and the simplified coupling matrix is shown in Fig. 6.11. Most of coupling factors smaller than 0.15 (or -18 dB) are neglected in the simplified model of the coupling matrix. Lastly, further enhancements of the calibration accuracy are achieved by means of the algorithm $C_{r,pca}$. The phase errors decrease below 5° whilst the amplitude deviations are less than 0.7 dB.

In the second experiment, sparse configuration of a 3x3 planar array with only five antennas, depicted in Fig. 6.9(b), are connected to the switch matrix. A similar measurement set-up as in the first experiment is used.

As shown in Fig. 6.12, the main beam direction of the receiver array can be clearly identified after the calibration. Moreover, larger modeling errors of the probe-patch coupling are also apparent due to the offset position of the receiver array. This results in a phase deviation of more than 25° and an amplitude error of more than 8 dB for the calibration algorithm C_f . On the other hand, if the simplified model C_r of the coupling matrix is known, calibration accuracy is significantly enhanced. A maximum phase error of roughly 10° with an amplitude error of maximum 2.5 dB reflects this improvement. Furthermore, the phase error decreases to 6° by the PCA method ($C_{r,pca}$). The accuracy of the calibrated amplitudes is, however, not improved. This fact underlines the need of a good probe-receiver coupling model to achieve highly accurate calibration results.

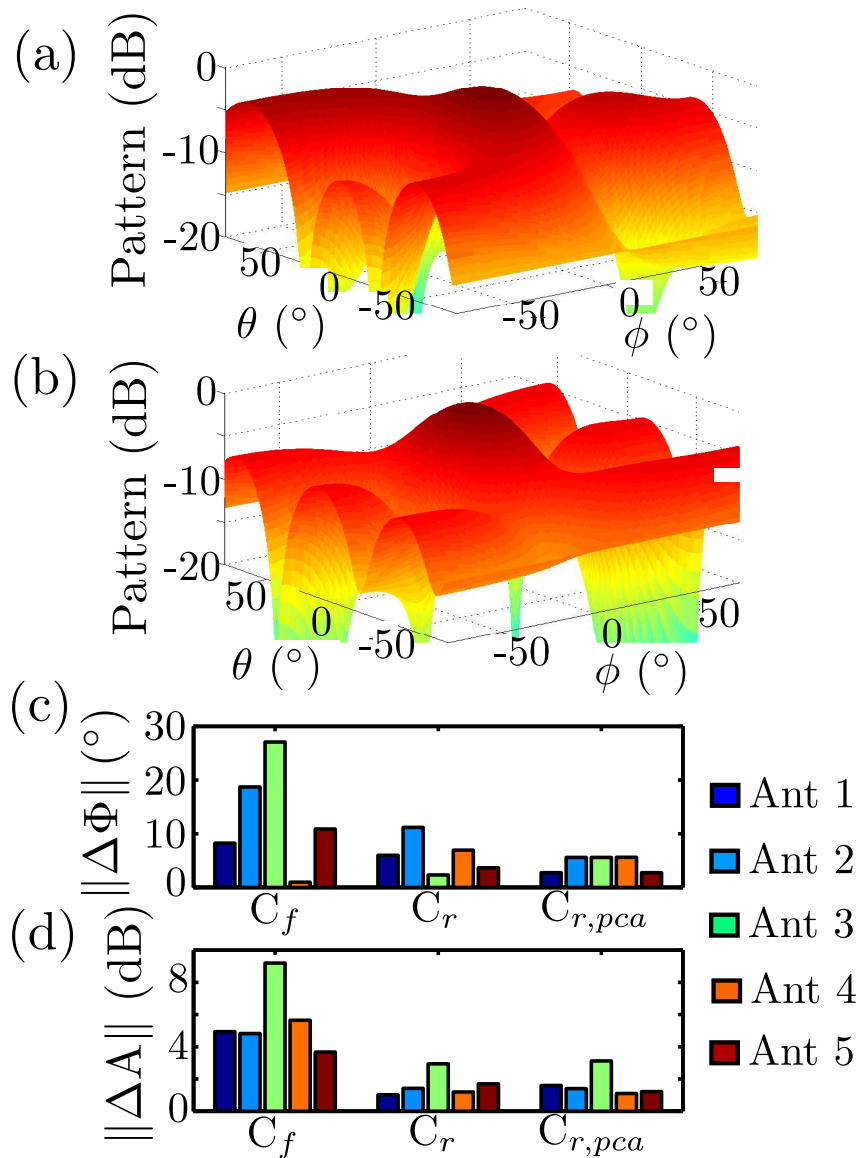


Figure 6.12: Experimental results of a Z-shaped array calibrated with 16 near-field monopole probes: radiation pattern (a) before and (b) after calibration as well as (c) phase and (d) amplitude deviations of the calibrated signals.

In the last experiment, the calibration measurements of the receiver system are performed outside the anechoic chamber. A 4x2 planar array connected to a coupler matrix is used as the receiver array as shown in Fig. 6.13. Three other antennas (R1, R2 and R3) are used as reference antennas. The others are again terminated with 50 Ω resistances. Additionally, 11 ports of a 12-port Agilent PNA are used as an 11-channel receiver. The rest is connected with a power amplifier to generate a high SNR calibration signal.

The radiation patterns of the 4x2 antenna array are illustrated in Fig. 6.14 for four different cases,

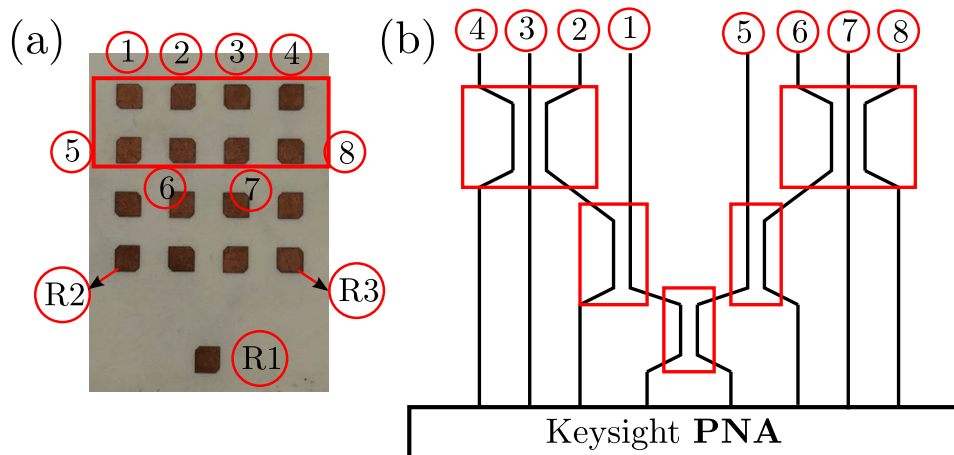


Figure 6.13: (a) The 4x2 planar array and (b) the switch matrix.

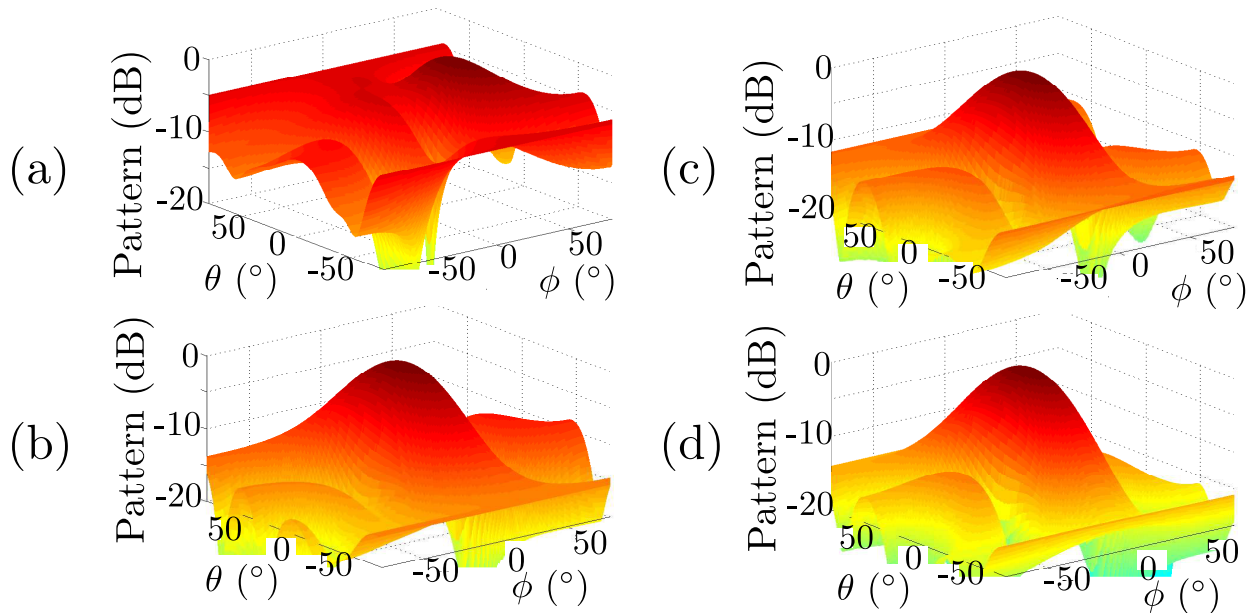


Figure 6.14: Radiation pattern of the 4x2 planar array: (a) before calibration, (b) after calibration with a reference channel and 16 probes (Case 1), and after calibration with 3 reference channels and (c) 8 probes (Case 2) as well as (d) 16 probes (Case 3).

including: the pattern before calibration, the calibrated pattern with 16 probes and one reference receiver (Case 1), the calibrated pattern with three reference channels and eight probes (Case 2) or 16 probes (Case 3), respectively. The correction of the main beam direction is realized in all calibrated patterns. Additionally, the side-lobe level is reduced from -8 dB (Case 1) or -10.8 dB (Case 2) to -12.2 dB (Case 3) as depicted in Fig. 6.15.

The amplitude and phase deviations of the eight antennas are shown in Fig. 6.16 in the case of the PCA method. In comparison with the results in Fig. 6.15, a 2 dB reduction of the amplitude errors

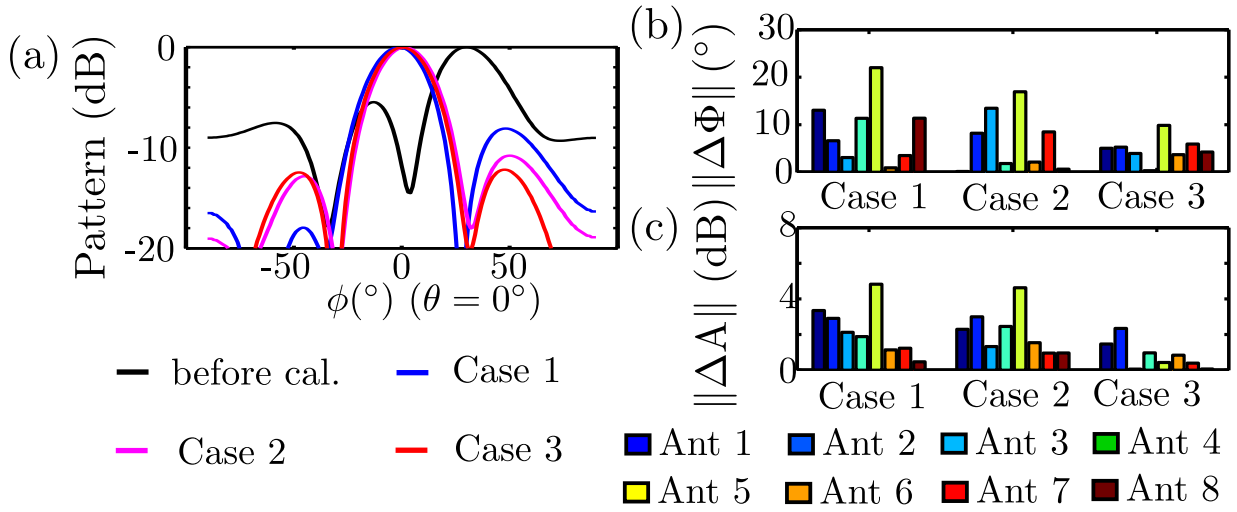


Figure 6.15: (a) Radiation pattern of the 4x2 planar array in the $\theta = 0^\circ$ cut plane and (b) phase as well as (c) amplitude deviations of eight antennas.

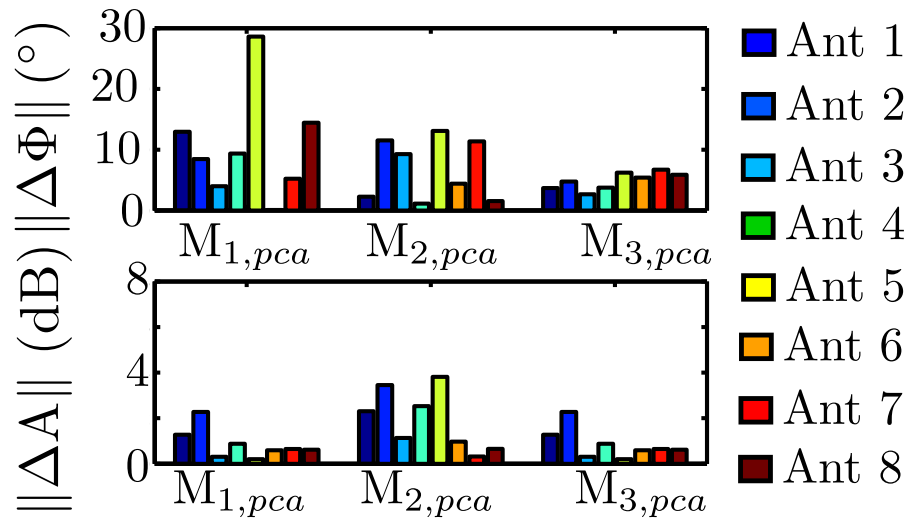


Figure 6.16: (Above) phase as well as (below) amplitude deviations of eight antennas calibrated with the PCA method.

is observed in Case 1 whilst a similar accuracy is achieved for Case 2 and Case 3. This implies that a high calibration accuracy is achieved without PCA if an adequate number of probes and reference receivers is used.

In addition, the most accurate calibration result is achieved with reference antenna 1 as demonstrated in Fig. 6.17. This suggests that there should be sufficient space between the reference antennas and the receiver array to keep a similar modeling ratio $\|K_{mn}/K_{mr}\|$ for all receiver elements.

Additionally, the receiver array is calibrated for the whole frequency bandwidth (from 19.8 GHz to 20.2 GHz) by the proposed method with the coupling model synthesized at the center frequency 20

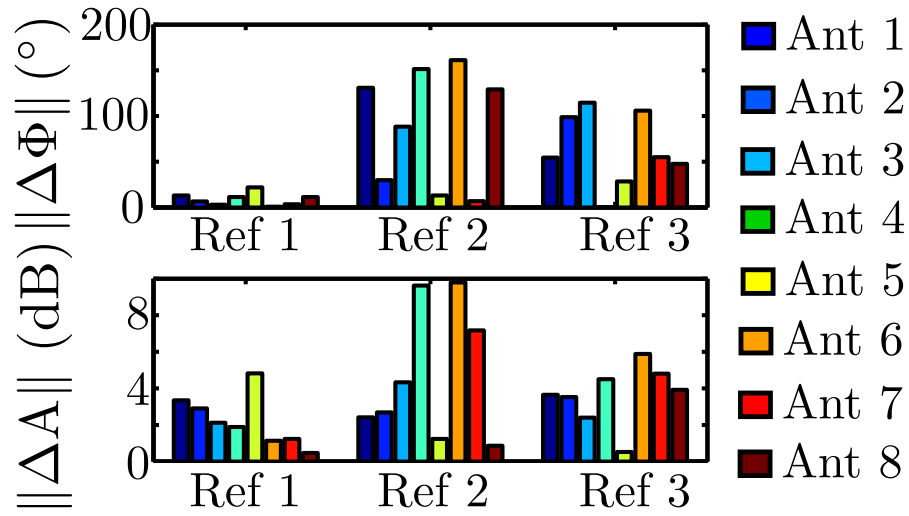


Figure 6.17: (Above) phase as well as (below) amplitude deviations of eight antennas calibrated with different reference antennas.

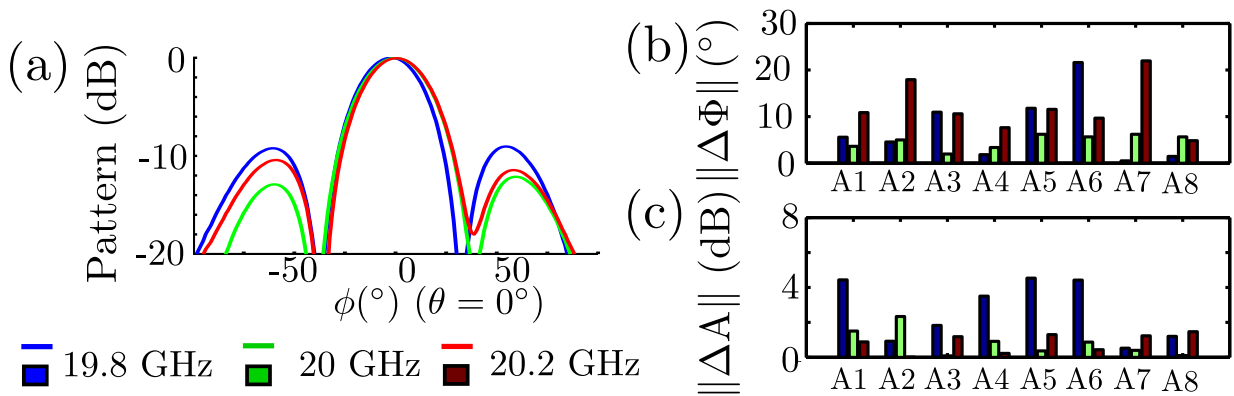


Figure 6.18: (a) Radiation pattern of the 4x2 planar array in the $\theta = 0^\circ$ cut plane and (b) phase as well as (c) amplitude deviations of eight antennas for three different frequencies.

GHz. The calibrated radiation patterns are depicted in Fig. 6.18. Whilst the maximum amplitude deviation increases to 4 dB, the maximum phase error rises to 20° . This results in more than a 2 dB degradation of the side-lobe level. Hence, this emphasizes the necessity of an accurate coupling model to achieve a high quality calibration procedure.

Last but not least, the essential coefficients of the simplified coupling matrix is depicted in Fig. 6.19(a) because of the knowledge of the switch matrix in Fig. 6.13(b). Furthermore, the calibration accuracy decreases as the number of unknown coefficients in the coupling matrix increases. This is illustrated in Fig. 6.19(b). Not only the side-lobe level rises from -12 dB (3 essential coefficients) up to -7 dB (6 essential coefficients), but also an error in main beam direction occurs. This underlines the importance of a prior system knowledge in the on-line calibration procedure.

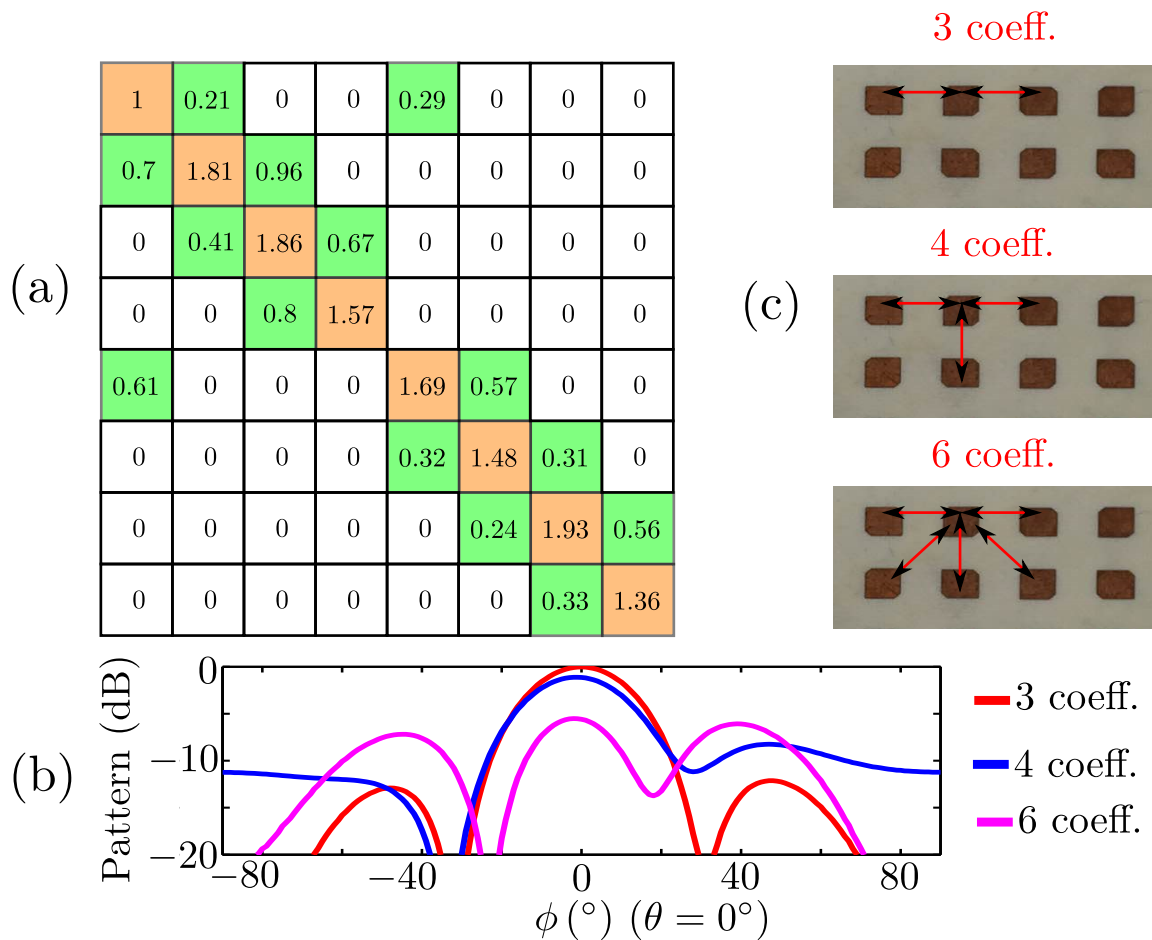


Figure 6.19: (a) Magnitude of the simplified coupling matrix C_r of the 4x2 planar array and (b) the radiation patterns in the $\theta = 0^\circ$ cut plane for various numbers of essential coupling coefficients as well as (c) positions of the essential coupling coefficients.

6.4 Summary

The usefulness of the external calibration concept with on-board probes is validated in the experiments. Due to its ease fabrication, the microstrip monopole is first applied as a calibration probe. As a result, the main beam in the radiation pattern of a three-patch linear array is corrected after the calibration. The need of calibration measurements with high SNR, which is achieved with high power calibration signals as well as long measurement time, is also demonstrated. The calibration accuracy is however limited because of the simple model of the probe-receiver coupling.

In order to overcome the model complexity of the microstrip probe, a coaxial probe backed by an absorber sheet is suggested. In case of only channel fluctuations, phase errors below 8° and amplitude deviations smaller than 1 dB are achieved for a 3x3 planar array after calibration.

In order to achieve similar accuracy in case of a joint compensation of the gain/phase deviations and the mutual coupling, the calibration system has to satisfy higher technical demands. Whilst

the desired accuracy is also illustrated for a 5x1 linear array with 16 probes, additional reference receivers are required for a 4x2 planar array to diversify the modeling errors. The performance degradations of the calibration procedure due to uncertainties of the coupling matrix model are also illustrated in the experimental result.

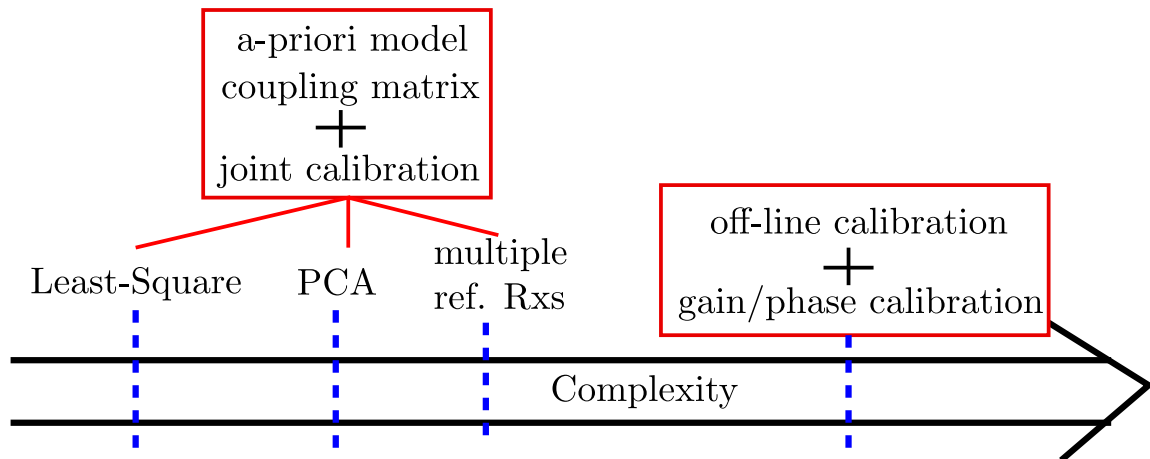


Figure 6.20: Complexity comparison of the different proposed calibration procedures.

Finally, a comparison of the system complexity is illustrated in Fig.6.20 for the various proposed procedures. This illustrates the findings that a higher calibration accuracy results in an increased complexity of the calibration system in terms of signal power, measurement time, and number of calibration probes as well as reference receivers.

7 Tolerance Analysis and Scalability

In this chapter, we investigate the accuracy of the calibration concept for a receiver array realized in brick architecture, as it is relevant in the present context. In detail, we elaborate what kinds of characteristics in terms of fabrication tolerances, signal power and bandwidth or measurement time the calibration system should have in order to guarantee desired performances such as the estimation accuracy of the Direction of Arrivals (DOAs) of the received signals and a low side-lobe level. As discussed in Chapter 2, the error of the DOA is negligible in case of large arrays, and not examined in this work.

To this end, we assume that the system can receive and process the far-field signals as accurately as possible. The effect of noise on the receiver operation is reviewed in Chapter 2, and hence, it is not considered in this work.

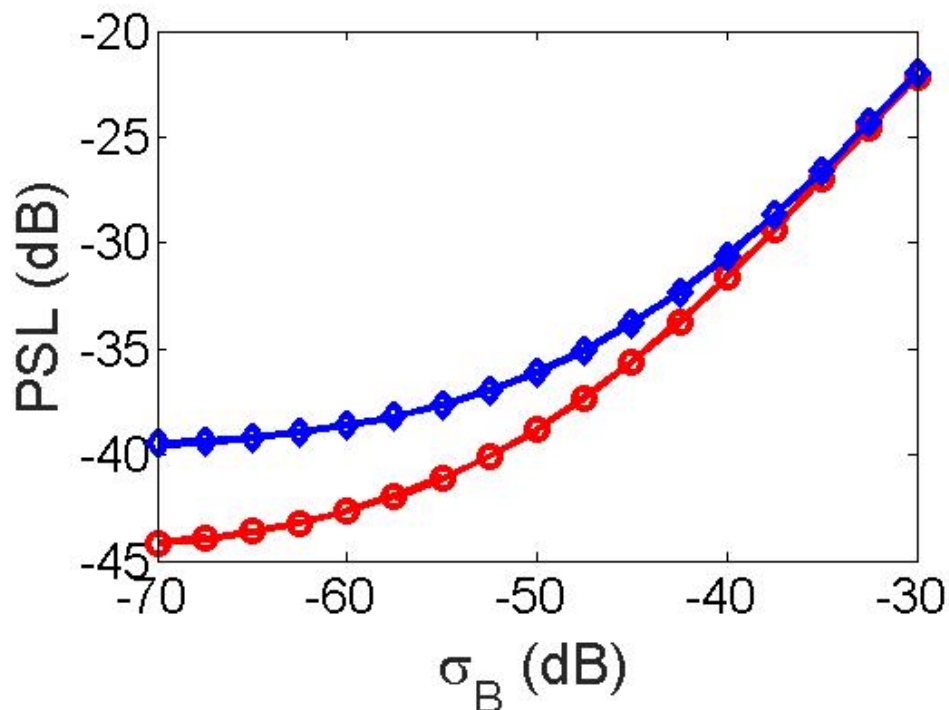


Figure 7.1: Peak side lobe level PSL versus the standard deviation σ_B of the beam pattern for two different array tapers with a designed side lobe of (blue) -40 dB and (red) -45 dB

In addition, the standard deviation σ_B of the first side-lobe in the array beam pattern is examined instead of the peak side lobe level (PSL). The behavior of σ_B and PSL, which is derived mathematically in Chapter 2, is compared in Fig 7.1. In order to achieve the desired PSL of -35 dB, the standard deviation of the beam pattern has to be smaller than -45 dB, which is independent of the array size.

This chapter is structured as follows: the surrogate model is firstly introduced in Section 7.1, whilst the uncertainty propagation method is reviewed in Section 7.2 to examine the impact of small errors in small-size arrays. On the other hand, Monte Carlo simulations are proposed in Section 7.3.3 to examine effectively the performance of the calibration system in case of a low SNR.

Furthermore, the stability and the scalability of the proposed calibration system are discussed in Section 7.4. With regard to the application of the on-board calibration method to a middle- up to large-size receiver system, we investigate the stability of only two procedures. The first one only deals with the calibration of channel deviations (see Chapter 4), while the second one applies the Least-Square method and its extension with multiple reference receivers (see Chapter 5) which was shown to yield the best experimental results (see Chapter 6). The PCA method which demands much higher SNR and computational complexity is not considered in this tolerance analysis.

7.1 Surrogate model

The surrogate model for the error propagation in the calibration operation is depicted in Fig. 7.2.

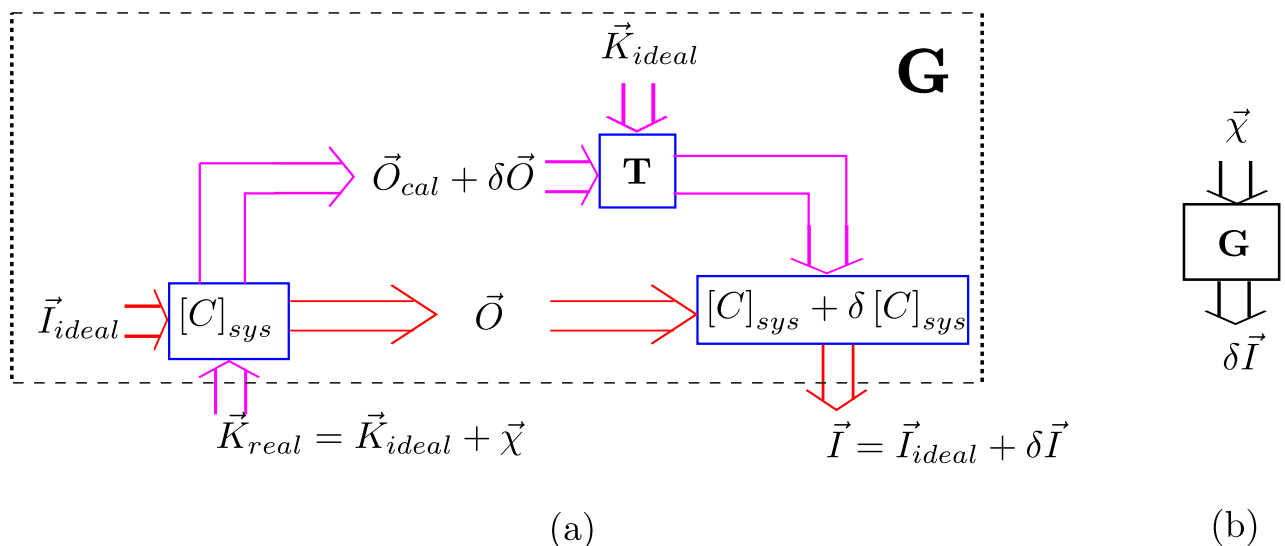


Figure 7.2: (a) Flow chart of calibration (magenta) and receiver operation (red) and (b) surrogate model of the error propagation.

In the real calibration system, the output signals \vec{O}_{cal} are afflicted with errors $\vec{\chi}$. The assumption of an ideal and fully characterized calibration system $[C]_{sys}$, however, is made in the procedure of

determining the receiver coupling matrix. This leads to faulty results. On the one hand, in order to reconstruct the signal of a far-field source in the receiver, the received signals are decoupled and corrected with the help of the faulty coupling matrix $[C]_{\text{sys}} + \delta [C]_{\text{sys}}$. As a result, we observe some deviations $\delta \vec{I}$ between the ideal \vec{I}_{ideal} and the reconstructed signals \vec{I} .

In order to analyze the performance degradation of the receiver with respect to the errors existing in the calibration system, a surrogate model \mathbf{G} of the whole procedure is used to show the relation between the disturbance vector $\vec{\chi}$ and the signal difference $\delta \vec{I}$ as depicted in (7.1). Besides, the disturbance vector $\vec{\chi}$ does not only includes the geometry faults of the calibration system but also the noise in the calibration signals.

7.2 Uncertainty Propagation

If only very small error levels are considered in the calibration system, a linear multivariate model \mathbf{G} of small deviations $\vec{\chi}$ around the system parameters is applied, and the asymptotic behavior can be examined. The surrogate model is expressed as

$$\vec{\chi} = \begin{pmatrix} \chi_1 \\ \vdots \\ \chi_K \end{pmatrix} \mapsto \delta \vec{I} = \mathbf{G}(\vec{\chi}) = \begin{pmatrix} g_{1,re}(\chi_1, \dots, \chi_K) \\ g_{1,im}(\chi_1, \dots, \chi_K) \\ \vdots \\ g_{N,re}(\chi_1, \dots, \chi_K) \\ g_{N,im}(\chi_1, \dots, \chi_K) \end{pmatrix}. \quad (7.1)$$

The Jacobian matrix, which describes the slopes of the surrogate model with respect to the variables, is calculated as

$$[J]_G = \begin{pmatrix} \frac{\partial g_{1,re}}{\partial \chi_1} & \frac{\partial g_{1,re}}{\partial \chi_2} & \dots & \frac{\partial g_{1,re}}{\partial \chi_K} \\ \frac{\partial g_{1,im}}{\partial \chi_1} & \frac{\partial g_{1,im}}{\partial \chi_2} & \dots & \frac{\partial g_{1,im}}{\partial \chi_K} \\ \vdots & \vdots & \ddots & \vdots \\ \frac{\partial g_{N,re}}{\partial \chi_1} & \frac{\partial g_{N,re}}{\partial \chi_2} & \dots & \frac{\partial g_{N,re}}{\partial \chi_K} \\ \frac{\partial g_{N,im}}{\partial \chi_1} & \frac{\partial g_{N,im}}{\partial \chi_2} & \dots & \frac{\partial g_{N,im}}{\partial \chi_K} \end{pmatrix}. \quad (7.2)$$

Here, $g_{n,re}$ and $g_{n,im}$ denote the real and imaginary part of the complex factor of channel n . In this work, the coefficients of the Jacobian matrix are determined numerically by means of the finite difference method as

$$\frac{\partial g}{\partial \chi} \approx \frac{g(\chi + \delta \chi) - g(\chi - \delta \chi)}{2\delta \chi}, \quad (7.3)$$

with $\delta \chi = 10^{-9} \chi$ for the implementation in MATLAB.

In statistics, the deviation of the system parameter χ is described by its mean value $\bar{\chi}$ and its variance σ_{χ}^2 . If for example, χ has a Gaussian distribution, χ lies in the interval $(\bar{\chi} - \sigma_{\chi}, \bar{\chi} + \sigma_{\chi})$ with a possibility of 68%. If χ is uniformly distributed in the interval $(\bar{\chi} - \delta\chi, \bar{\chi} + \delta\chi)$, the variance of χ is $\sigma_{\chi}^2 = \frac{(\delta\chi)^2}{3}$.

If a vector $\vec{\chi}$ of deviations is considered, the covariance matrix

$$[Cov]_{\chi} = \begin{pmatrix} \sigma_{\chi_1}^2 & \sigma_{\chi_1, \chi_2} & \cdots & \sigma_{\chi_1, \chi_K} \\ \sigma_{\chi_2, \chi_1} & \sigma_{\chi_2}^2 & \cdots & \sigma_{\chi_2, \chi_K} \\ \vdots & \vdots & \ddots & \vdots \\ \sigma_{\chi_K, \chi_1} & \sigma_{\chi_K, \chi_2} & \cdots & \sigma_{\chi_K}^2 \end{pmatrix} \quad (7.4)$$

is used, instead of the variance.

The coefficient $\sigma_{\chi_k}^2$ on the main diagonal of the covariance matrix denotes the variance of the k^{th} variable χ_k whilst the off-diagonal component σ_{χ_l, χ_k} with $l \neq k$ represents the cross-covariance of the variables χ_l and χ_k . In case the deviation variables are independent of each other, their cross-covariances are zero and $[Cov]_{\chi}$ is a diagonal matrix.

According to GUM (ISO Guide to the Expression of Uncertainty in Measurement) [51], the covariance matrix $[Cov]_I$ of the output quantities is determined by the law of propagation of uncertainty as

$$[Cov]_I = [J]_G [Cov]_{\chi} [J]_G^T, \quad (7.5)$$

$$[Cov]_I = \underbrace{\begin{pmatrix} \frac{\partial g_{1,re}}{\partial \chi_1} & \cdots & \frac{\partial g_{1,re}}{\partial \chi_K} \\ \frac{\partial g_{1,im}}{\partial \chi_1} & \cdots & \frac{\partial g_{1,im}}{\partial \chi_K} \\ \vdots & \ddots & \vdots \\ \frac{\partial g_{N,re}}{\partial \chi_1} & \cdots & \frac{\partial g_{N,re}}{\partial \chi_K} \\ \frac{\partial g_{N,im}}{\partial \chi_1} & \cdots & \frac{\partial g_{N,im}}{\partial \chi_K} \end{pmatrix}}_{[J]_G} \underbrace{\begin{pmatrix} \sigma_{\chi_1}^2 & \cdots & \sigma_{\chi_1, \chi_K} \\ \vdots & \ddots & \vdots \\ \sigma_{\chi_K, \chi_1} & \cdots & \sigma_{\chi_K}^2 \end{pmatrix}}_{[Cov]_{\chi}} \underbrace{\begin{pmatrix} \frac{\partial g_{1,re}}{\partial \chi_1} & \frac{\partial g_{1,im}}{\partial \chi_1} & \cdots & \frac{\partial g_{N,re}}{\partial \chi_1} & \frac{\partial g_{N,im}}{\partial \chi_1} \\ \vdots & \vdots & \ddots & \vdots & \vdots \\ \frac{\partial g_{1,re}}{\partial \chi_K} & \frac{\partial g_{1,im}}{\partial \chi_K} & \cdots & \frac{\partial g_{N,re}}{\partial \chi_K} & \frac{\partial g_{N,im}}{\partial \chi_K} \end{pmatrix}}_{[J]_G^T}. \quad (7.6)$$

We can recognize that, due to (7.6), the output quantities are correlated to each other, even though all input quantities are independent.

7.3 Effects on the Beam Pattern

The uncertainty of the re-constructed array signals with respect to the calibration errors was determined in the last section. In the following, we further extend the uncertainty analysis and examine the effects on the beam pattern of the array.

As shown in Chapter 2, the far-field signal at the angle position (θ, ϕ) can be re-calculated from the signals $\vec{I} = [I_1, \dots, I_N]^T$ of N receivers as

$$B(\theta, \phi) = \vec{w}^H \text{diag}\{\vec{I}\} \vec{v}(\theta, \phi) = \underbrace{\vec{v}^T(\theta, \phi) \otimes \vec{w}^H}_{\vec{t}(\theta, \phi)} \vec{I} = \vec{t}(\theta, \phi) \vec{I} \quad (7.7)$$

with \vec{w} and \vec{v} being weighting and beam-forming vectors, respectively. Here, \otimes denotes the cross product, or vector product, of two vectors.

By using the flow chart in Fig. 7.2 and equation 7.7, the beam pattern deviation ΔB in a certain direction (θ, ϕ) can be formulated as

$$\Delta B(\theta, \phi) = \vec{v}^T(\theta, \phi) \otimes \vec{w}^H \delta \vec{I} = \vec{v}^T(\theta, \phi) \otimes \vec{w}^H [J]_G \delta \vec{\chi} \quad (7.8)$$

with $\delta \vec{\chi}$ and $[J_G]$ being the vector of deviations and its corresponding Jacobian matrix, respectively. At this point, two interesting questions arise:

- What is the maximum deviation of $\Delta B(\theta, \phi)$,
- and how does the distribution of $\Delta B(\theta, \phi)$ look like?

The first question corresponds to the worst-case bound whilst the second one can be answered by a statistical analysis. A similar analysis of both cases performed in [32] is extended to examine the effects of calibration errors.

7.3.1 Worst-Case Bound

By using the Cauchy-Schwarz inequality, we have

$$\max_{\theta, \phi} \|\Delta B(\theta, \phi)\| \leq \|\vec{v}(\theta, \phi)\|_2 \cdot \|\vec{w}^H\|_2 \cdot \|[J]_G \delta \vec{\chi}\|_2 = (\Delta B)_{\max}. \quad (7.9)$$

In this equation, the L2-norm of the vectors can be calculated as

$$\|\vec{w}^H\|_2 = \sqrt{\sum_{n=1}^N |w_n|^2}, \quad (7.10)$$

$$\|\vec{v}(\theta, \phi)\|_2 = \sqrt{\sum_{n=1}^N \left| \exp\left(-j \frac{2\pi}{\lambda_0} \vec{k}^T \vec{x}\right) \right|^2} = \sqrt{N}, \quad (7.11)$$

$$\begin{aligned} \|[J]_G \delta \vec{\chi}\|_2 &= \sqrt{\sum_{n=1}^N \left[\left(\sum_{k=1}^K \left(\frac{\partial g_{n,re}}{\partial \chi_k} \delta \chi_k \right) \right)^2 + \left(\sum_{k=1}^K \left(\frac{\partial g_{n,im}}{\partial \chi_k} \delta \chi_k \right) \right)^2 \right]} \\ &\leq \sqrt{\sum_{n=1}^N \left[\left(\sum_{k=1}^K \left| \frac{\partial g_{n,re}}{\partial \chi_k} \delta \chi_{k,\max} \right| \right)^2 + \left(\sum_{k=1}^K \left| \frac{\partial g_{n,im}}{\partial \chi_k} \delta \chi_{k,\max} \right| \right)^2 \right]}. \end{aligned} \quad (7.12)$$

Here, $\delta\chi_{k,\max}$ is the largest deviation of the error χ_k . If χ_k is uniformly distributed in the interval $(\bar{\chi}_k - \sigma_{\chi_k}, \bar{\chi}_k + \sigma_{\chi_k})$, then $\delta\chi_{k,\max} = \sigma_{\chi_k}$. This kind of error distribution is suitable for the error analysis of the geometry parameters. If the noise effect is taken into account, a Gaussian distribution with variance $\sigma_{\chi_k}^2$ is assumed. In this case, $\delta\chi_{k,\max} = 3\sigma_{\chi_k}$ is applied because χ_k lies in the interval $(\bar{\chi}_k - 3\sigma_{\chi_k}, \bar{\chi}_k + 3\sigma_{\chi_k})$ with a possibility of 99.7%. Lastly, the maximum deviation of the beam pattern is estimated as

$$(\Delta B)_{\max} = \sqrt{N} \cdot \sqrt{\sum_{n=1}^N w_n^2} \cdot \sqrt{\sum_{n=1}^N \left[\left(\sum_{k=1}^K \left| \frac{\partial g_{n,re}}{\partial \chi_k} \delta\chi_{k,\max} \right| \right)^2 + \left(\sum_{k=1}^K \left| \frac{\partial g_{n,im}}{\partial \chi_k} \delta\chi_{k,\max} \right| \right)^2 \right]} \quad (7.13)$$

and is angle-independent.

7.3.2 Statistical Analysis

As $\vec{t}(\theta, \phi)$ is a constant vector for a given (θ, ϕ) , the variance $\sigma_{\Delta B}^2(\theta, \phi)$ can be calculated from (7.7) as

$$\sigma_{\Delta B}^2(\theta, \phi) = \vec{t}(\theta, \phi) [Cov]_I \vec{t}(\theta, \phi)^H = \vec{t}(\theta, \phi) [J]_G [Cov]_X [J]_G^H \vec{t}(\theta, \phi)^H. \quad (7.14)$$

As discussed in [32], the beam pattern deviation is angle-independent only if $[Cov]_I$ is a diagonal matrix, which means the deviations of all channels are independent of each other. This condition is not satisfied in case of calibration errors as demonstrated above in Section 7.2. Thus, the variance $\sigma_{\Delta B}^2$ fluctuates slightly over (θ, ϕ) .

7.3.3 Monte-Carlo Simulation

In the case of large receiver arrays (e.g. a 64x64 planar array), the number of uncertainty variables exceeds 4000 if the minimum SNR of the calibration signal should be determined. Additionally, it is sufficient in practice to assume Gaussian distribution not only for the noise in the receiver channels (distribution of the input uncertainty) but also for the real and imaginary parts of the beam pattern at a certain angle direction (distribution of the output uncertainty). Compared to the Taylor-expansion method, the traditional Monte-Carlo simulation is more suitable for the examination because of the limited computational cost. The number of sampling is set to 5000 in this work.

7.4 Scalability

In the context of the applications, the calibration procedures are developed for medium- up to large-size arrays. Due to the limited available hardware, their usefulness can, however, only be validated by experiments with small-size receiver arrays in this work. Hence, the last issue of the calibration system mentioned in Chapter 3

- What are the requirements for the calibration system and its achievable accuracy with respect to the size of the receiver system?

should be examined. In other words, the scalability of the calibration system has to be determined for various sizes of the receiver system.

In this Section, we propose a procedure to figure out the technical requirements of the calibration system with external near-field probes for a given receiver system. As a trade-off between the compactness of the system set-up and the model applicability of the proposed probe-receiver coupling, the minimum distance between the calibration probe and the receiver is set to $d_{min} = 4.5\lambda = 67.5$ mm. This corresponds to a maximum probe-receiver coupling of -34 dB. Additionally, without loss of generality, the power of the calibration signals is assumed to be 0 dBW.

Several system errors are considered in this work, namely

- errors of the probe position and alignment,
- the additive noise in the receiver system,
- the modeling uncertainty of the probe-receiver coupling,
- and the number of the essential coefficients of the coupling matrix.

On the other hand, as discussed above, the calibration accuracy is demonstrated by the standard deviation σ_B of the first side-lobe in the array beam pattern. As a result of the tolerance analysis, the technical specifications of the calibration system, such as the number of calibration probes and the required signal-to-noise-ratio of the calibration signals, can be determined.

7.4.1 Channel deviations

The following study concerns the calibration of only the gain and phase errors in the receiver channels as presented Chapter 4. The channel cross-talk is assumed to be negligible in this case and/or already determined through an intensive off-line calibration in an anechoic chamber. Besides, two averaging methods, namely the arithmetic and the geometric mean, are examined.

Limitations due to probe position uncertainty

The stability of the calibration procedure against the uncertainty of the probe position is demonstrated in Fig. 7.3. In order to achieve a beam pattern variance of better than -45 dB, an accuracy of 0.1 mm is required for the probe position.

Additionally, both a GUM- and a Monte-Carlo analysis yield nearly the same results for small position deviations. Due to its simple, first order model assumption, the GUM method shows, however, unrealistic beam pattern errors in case of large deviations. Thus, to assert the results in these cases a Monte Carlo simulation has to be performed.

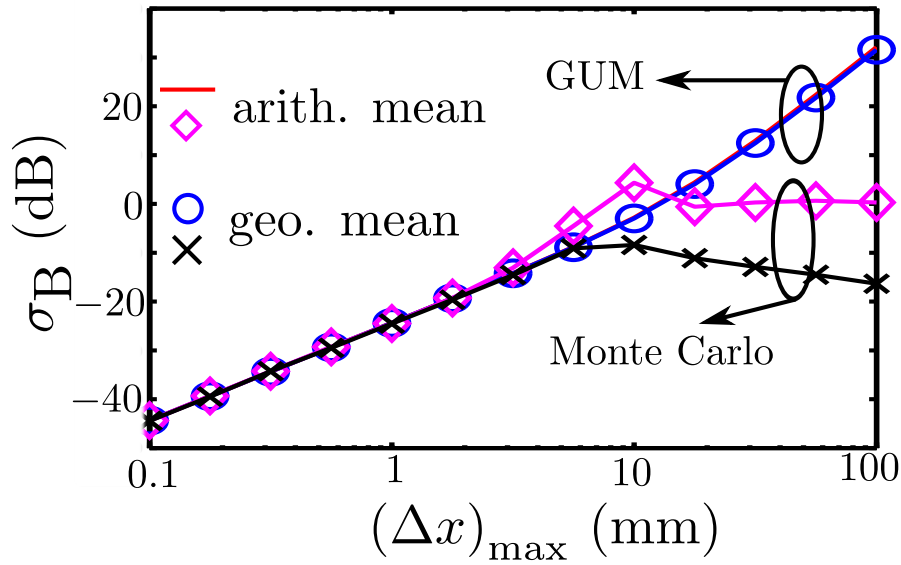


Figure 7.3: A 32x32 planar receiver array calibrated with 32 probes: Variance $\sigma_{\Delta B}$ of the beam pattern uncertainty versus the maximum deviation Δx of the probe position.

Limitations due to receiver noise

Fig. 7.4 demonstrates the variance of the beam pattern uncertainty as a function of the noise power in the receiver channels for a Tschebyscheff and a Taylor window with a side-lobe level of -35 dB (see

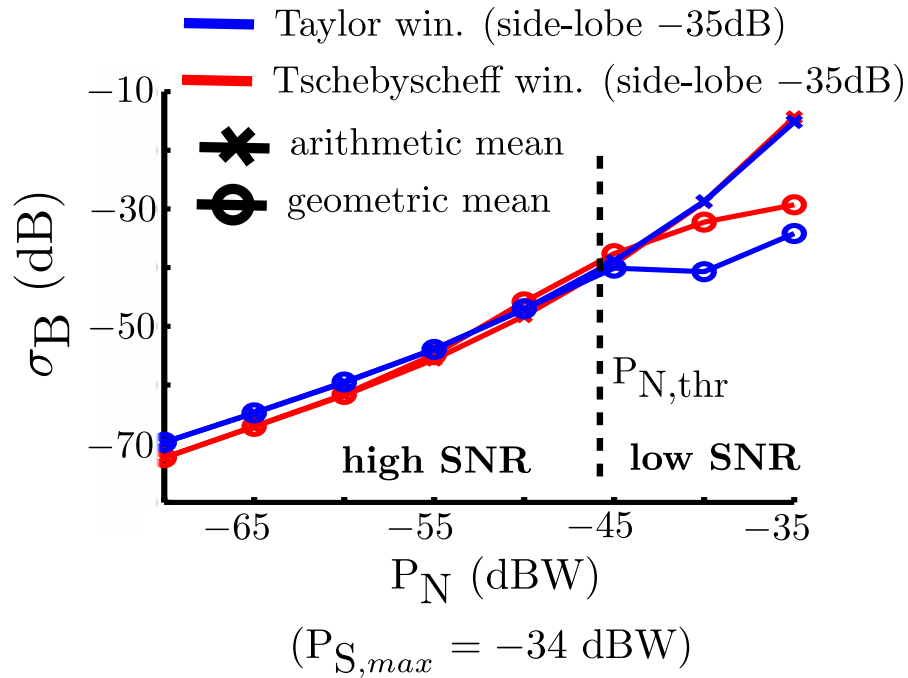


Figure 7.4: A 32x32 planar receiver array calibrated with 32 probes: Variance of the beam pattern uncertainty as function of the noise power in the receiver channels.

Chapter 2). A linear relationship between the pattern variance and the noise power is observed in the case of a high SNR of the calibration signal (low noise power). Additionally, the arithmetic and the geometric mean demonstrate similar calibration accuracy. In regions with low SNR, a nonlinear behavior of the beam pattern variance is observed for both averaging methods. In this case, the calibration algorithm with geometric mean can reduce the influence of outliers (samples with large errors) and hence outperforms the method based on the arithmetic mean.

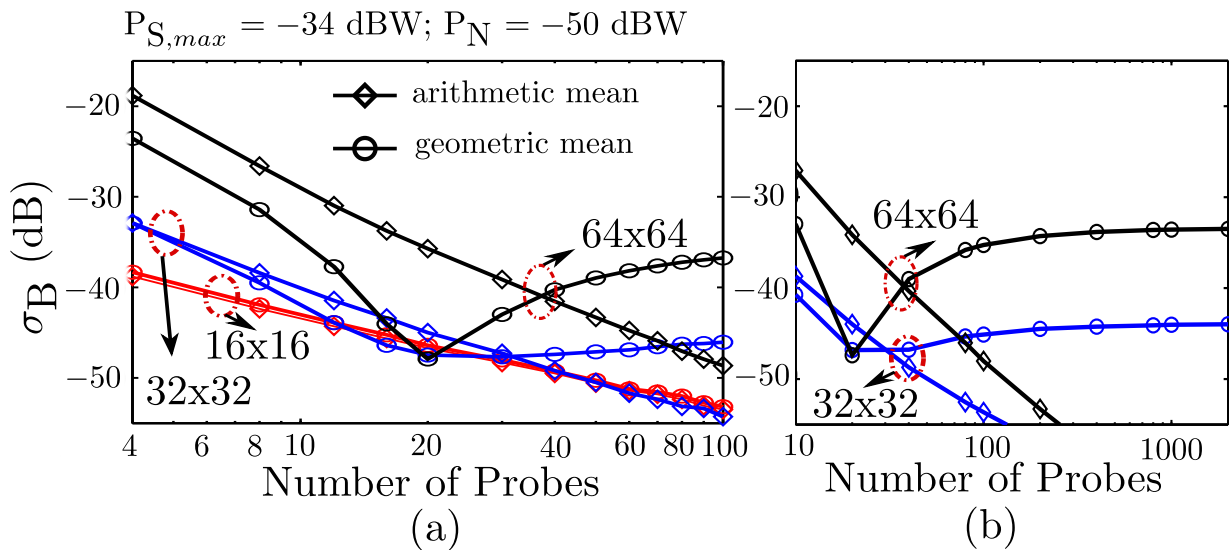


Figure 7.5: Variance of the beam pattern uncertainty as a function of the probe number (logarithmic scale) for different receiver array sizes with $P_{S,max} = -34$ dBW and $P_N = -50$ dBW: (a) interval [4, 100] and (b) [10, 2000].

In the next example, we examine the dependence of the beam variance on the number of calibration probes as depicted in Fig. 7.5. Although this is not practical in a real system, large probe numbers of more than 100 are still considered in this study to demonstrate the asymptotic system behavior.

The variance (in dB) scales linearly with the probe number (logarithmic scale) for the arithmetic mean. The slope of the linear function depends on the average SNR of the calibration signals in all receiver channels, and it is therefore determined by the array size for a given signal power and noise floor.

On the hand, the geometric mean generally exhibits a nonlinear behavior. In case of small arrays, the free-space attenuation of the calibration signals is rather low, and the performance of both approaches is similar. In case of large arrays, the uncertainty variance first decreases dramatically with an increasing number of probes and then reaches a local minimum. However, if the probe number rises further, the variance of the beam pattern uncertainty increases again and approaches its asymptote. This effect can be explained by the intrinsic nonlinear characteristic of the geometric mean.

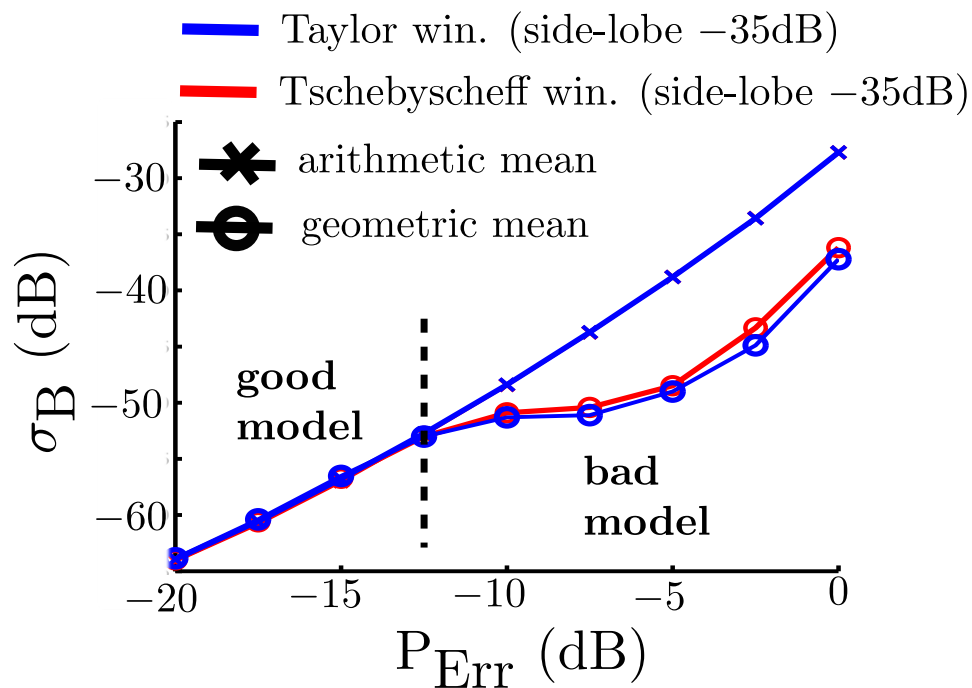


Figure 7.6: A 64x64 planar receiver array calibrated with 16 probes: Variance of the beam pattern uncertainty as a function of the modeling error of the probe-receiver coupling.

Limitations due to modeling uncertainties

Besides the errors caused by measurement noise, modeling uncertainties are another issue, which limits the calibration accuracy. Three aspects should be mentioned, namely:

- (1) the differences between the real world and the simulation model in HFSS,
- (2) the noise floor in the HFSS simulation caused by the discretization and meshing procedures as well as the limited computational resources,
- (3) the smoothing procedure stemming from the analytical model.

In this work, we examine the first and the third aspect with a relative noise whilst the second aspect is represented by an absolute noise floor, the results of which are already highlighted above.

In comparison with the case of the receiver noise, similar results are shown for the modeling uncertainty. As depicted in Fig. 7.6, a linear and a non-linear behavior of the beam uncertainty are obtained for the high and low SNR regions, respectively. With a smaller beam uncertainty in the region of high modeling errors, the geometric mean outperforms the arithmetic mean. This leads to a relaxation of the modeling of the probe-receiver coupling for a desired calibration accuracy as well as the broader applicability of the same coupling model to various working situation of the system.

Limitations due to unessential mutual coupling

Fig. 7.7 shows the degradation of the calibration accuracy caused by the unessential coupling coefficients. The graph shows that calibration signals with an approximately 20 dB higher SNR are required if the unessential coefficients are to be determined.

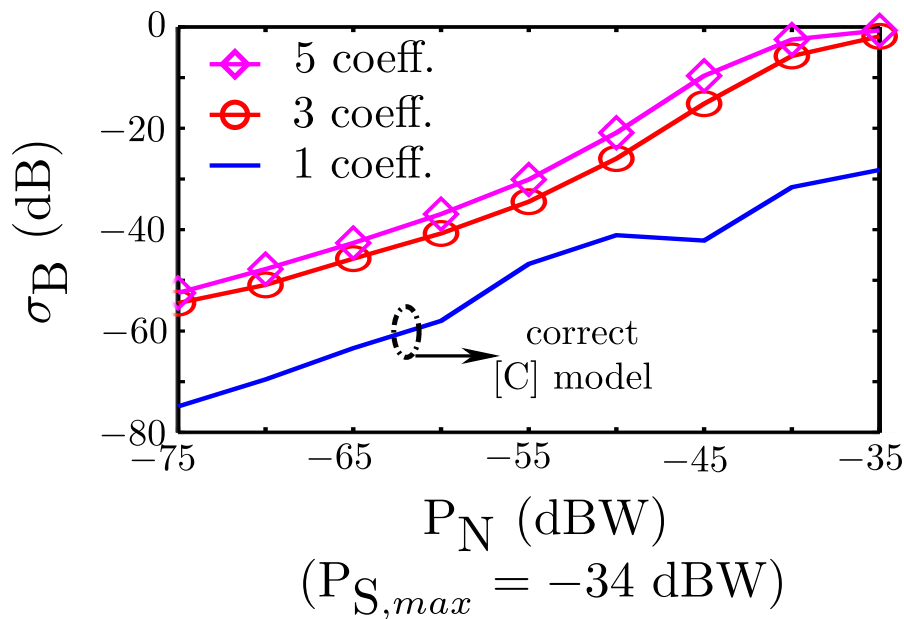


Figure 7.7: A 64x64 planar receiver array calibrated with 32 probes: Variance of the beam pattern uncertainty as a function of receiver noise for different numbers of essential coupling coefficients.

7.4.2 Effect of mutual coupling

In this section, the mutual coupling within the receiver array is taken into account. As mentioned above, a receiver array with brick architecture is chosen in this work because of its flexibility. Hence, the tolerance analysis is performed only for this receiver array. In accordance with practical experience, the cross-talk between sub-modules is assumed to be negligible. It should be mentioned that similar examination procedures can be applied to determine the technical requirements of an online calibration system if other architectures of the main system are considered.

Additionally, we assume that the mutual coupling decreases for larger element distance. This assumption is valid not only for the antenna structure but also for the active circuitry in terms of existence probability. As an example, a receiver has a coupling of -15 dB with the adjacent element and a coupling of -20 dB with the next one. All other couplings are assumed to be negligible.

In the first investigation, the effect of the number of calculated essential coupling coefficients is studied. The results are reported in Fig. 7.8. If the correct model of the coupling matrix is applied,

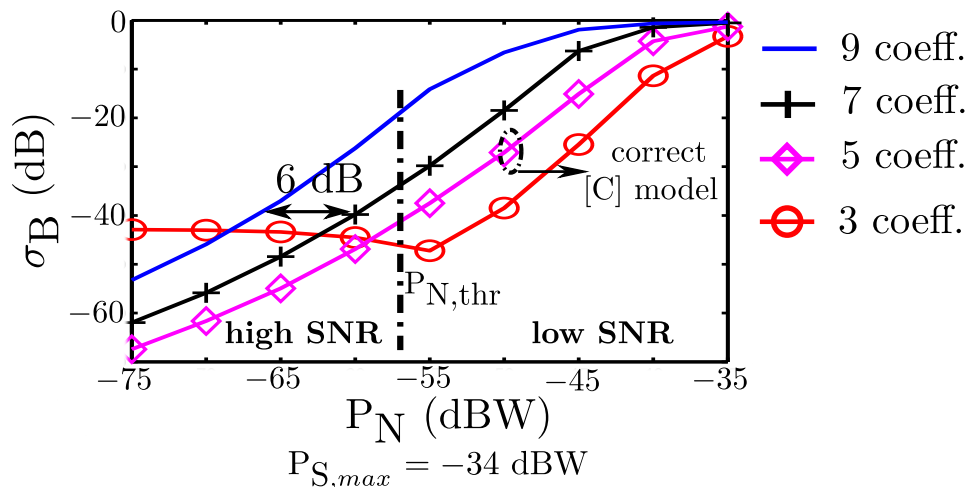


Figure 7.8: A 32x32 planar receiver array calibrated with 32 probes: Variance of the beam pattern uncertainty as a function of receiver noise for different numbers of essential coupling coefficients.

the regions of high and low SNR corresponding to the linear and non-linear behavior of the variance of the beam pattern are well recognized. As a result of mutual coupling, the noise threshold $P_{N,thr}$ is reduced by approximately 10 dB compared to the case reported in Fig. 7.4 for the same system set-up. This is in agreement with the need of higher power calibration signals and low measurement bandwidth as well as longer measurement time, that was already noted previously.

To take more unessential coupling coefficients into account, calibration signals with a larger SNR are necessary. An SNR increase of roughly 3 dB per unessential coefficient is required to achieve a similar calibration accuracy if the model of the coupling matrix is over-estimated. On the other side, there is an accuracy limit due to the undetermined essential coupling coefficients in the under-estimated model of the coupling matrix even if the SNR of the signals rises. A better calibration accuracy is, however, obtained in region of low SNR because the accuracy limit determined by the receiver noise already overcomes the effect caused by small mutual coupling factors.

Besides, an SNR increase of the calibration signals and therefore an improvement of the calibration accuracy, as depicted in Fig. 7.9, are achieved for a given level of receiver noise by increasing the number of calibration probes. A similar behavior of the calibration accuracy relating to an under-/overestimated number of essential coupling coefficients is observed for high and low probe numbers, which correspond to high and low SNR regions in Fig. 7.8, respectively.

Additionally, Fig. 7.10 demonstrates the demand of low fluctuations of the calibration signals. For example, in a calibration system with 56 probes, a beam variance of less than -44 dB is achieved for probe signal with $SNR_{cal.sig.} = 30$ dB. On the other hand, for a probe signal with $SNR_{cal.sig.} = 15$ dB, the calibration accuracy decreases yielding an increased beam variance of -29 dB. This emphasizes the need of a procedure for compensating the deviations in the calibration subsystems of a TDMA

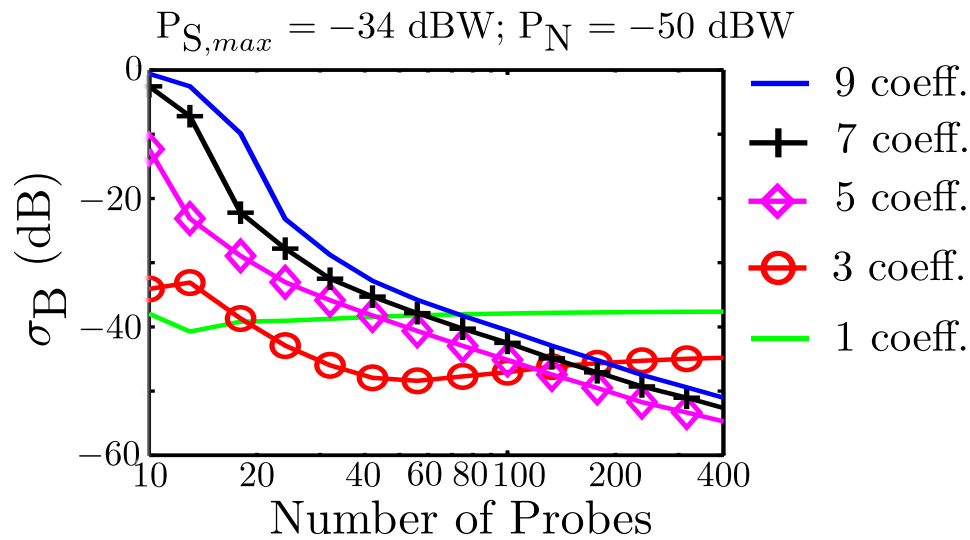


Figure 7.9: A 32x32 planar receiver array: Variance of the beam pattern uncertainty as a function of the probe number for different numbers of essential coupling coefficients with $P_N = -50$ dBW.

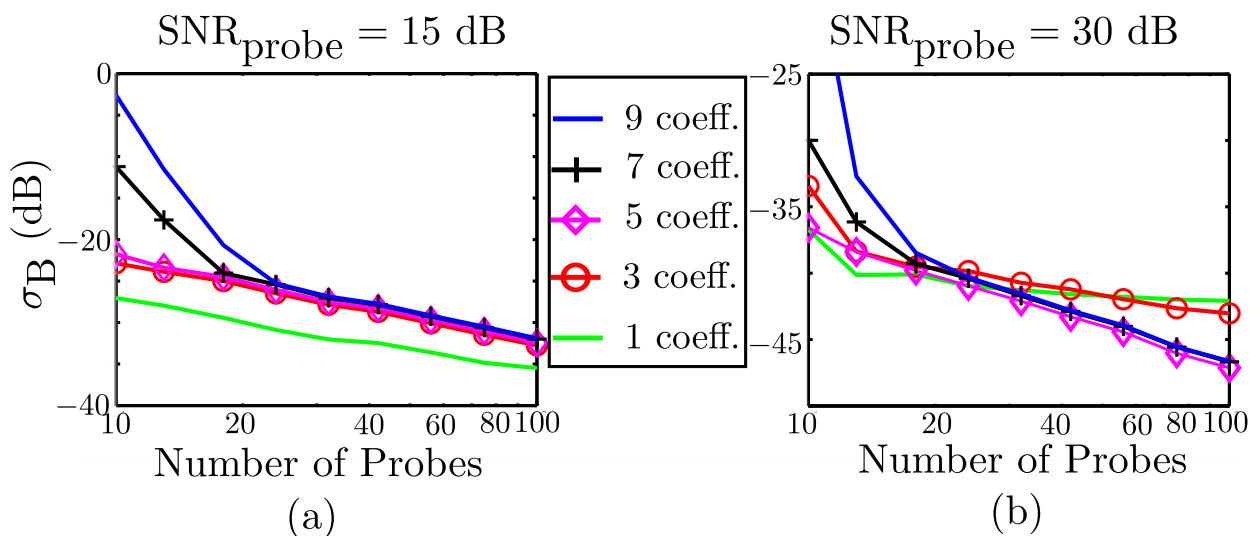


Figure 7.10: A 32x32 planar receiver array: Variance of the beam pattern uncertainty as a function of the number of the probes for different numbers of essential coupling coefficients with (a) $\text{SNR}_{\text{cal.sig.}} = 15$ dB and (b) $\text{SNR}_{\text{cal.sig.}} = 30$ dB.

scheme.

Similar to the calibration approach for the receiver array, two approaches can be considered here to compensate the fluctuation in the calibration subsystems, namely an internal and an external approach (see Fig. 5.2 in Chapter 5). In the latter one, additional isolated reference channels are placed between the receiver array and the calibration probes. By normalizing the received signals to the signals in the reference channels, the deviation of various calibration subsystems can be compensated. As discussed in Chapter 5, SNR improvements of the calibration signals can be achieved by diver-

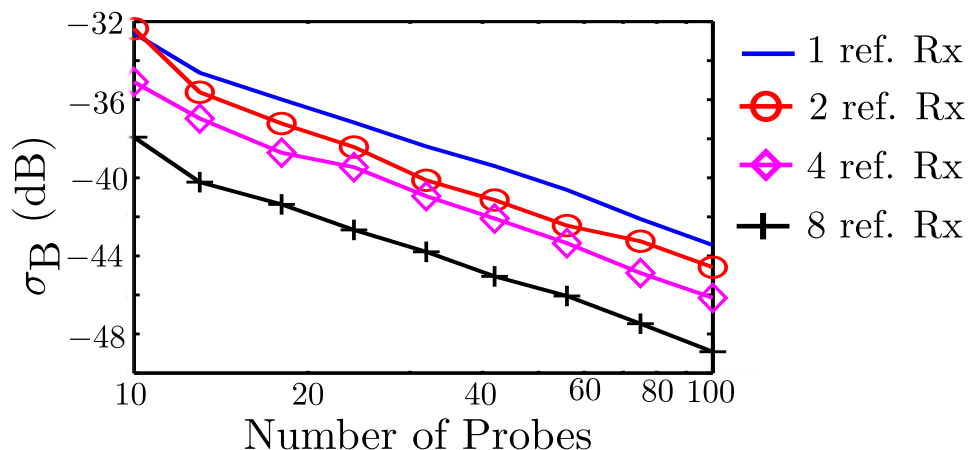


Figure 7.11: A 32x32 planar receiver array: Variance of the beam pattern uncertainty as a function of the number of probes for different numbers of reference channels with $P_N = -75$ dBW and $P_{S,max} = -34$ dBW.

sifying the modeling errors with multiple reference receivers. This fact is illustrated in in Fig. 7.11. Because of its high flexibility and the low hardware cost, this approach is used in this work and its applicability is demonstrated for small receiver arrays.

On the other side, internal couplers and distribution network could be implemented inside the calibration system. Because of the limited number of probes and the low integration density of the calibration system, the hardware complexity would be acceptable, making this approach worthwhile to be studied in future work.

From this point of view, we derive now the requirements and compare the characteristics of the internal and the external compensation approach of the calibration system for large-size receiver arrays.

The beam uncertainty for arrays of different size is plotted in Fig. 7.12 as a function of the receiver noise level. Two different trends are observed for the two concepts.

Due to the closed set-up in the internal approach, a similar SNR is obtained for all calibration subsystems. Additionally, the influence of calibration signal fluctuations is diversified over the number of receiver elements. As a result, the beam pattern variance decreases with the size of the receiver array in the case of low receiver noise. In the case of high receiver noise and low SNR, the pattern variance rises however with the array size. In other words, lower fluctuations of the calibration signals are required in the low SNR region.

In the external approach, the accuracy decreases with increasing receiver size for a given calibration system. This can be explained by the open set-up of the reference channels. Due to their placement, the average distance between the reference antennas and the probes is increased for larger arrays. This means, the power of the received signal in this reference channel and its SNR decrease. Thus,

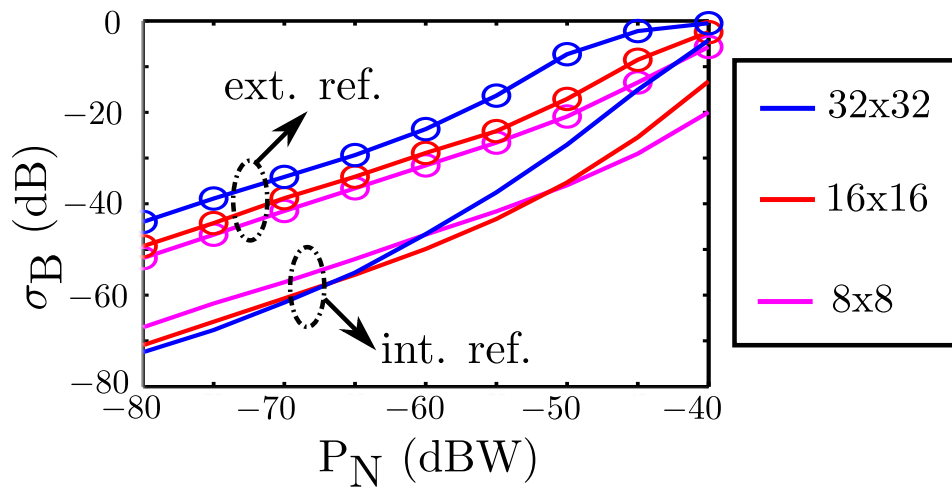


Figure 7.12: Variance of the beam pattern uncertainty as a function of receiver noise level with $P_{S,\max} = -34$ dBW.

compared to that of the internal compensation approach, the SNR of the calibration signals has to be much lower if the calibration system is compensated with the external references.

From this point of view, a proper selection of probes and reference receivers has to be ensured to improve the robustness and accuracy of the external calibration procedure for large-size receiver arrays.

7.5 Summary

Based on a tolerance analysis, the scalability of the proposed calibration procedure with on-board probes is discussed in this chapter. Instead of the peak side lobe level, the equivalent standard deviation σ_B is used as figure of merit in the analysis. The relation between the two parameters is also derived and shown graphically.

Firstly, an approach with a surrogate model is discussed in Section 7.1. Two analysis methods, namely the uncertainty propagation in Section 7.2 and the Monte-Carlo approach in Section 7.3.3, are reviewed and examined. Whilst the uncertainty propagation method shows more insights into the system behavior (under the assumption of small deviations), the Monte-Carlo simulation demonstrates better accuracy for large system errors and also less calculation effort for large-size receiver arrays. Thus, the second approach is used further in the scalability analysis.

Furthermore, the scalability analysis is performed for two calibration procedures, namely the calibration of only channel deviations (see Chapter 4) and the joint calibration of channel deviations and mutual coupling in Chapter 5. The calibration performance with respect to various parameters such as the number of probes and their positions, the SNR of the calibration signals as well as the model

accuracy of the probe-receiver coupling are considered in the study.

As results, a position accuracy of 0.1mm as well as an SNR of the calibration signal of better than 30dB are required for a peak side lobe level of less than -35dB . Besides, if the calibration of mutual coupling is taken into account, the necessity of a simplified coupling matrix of the receiver is emphasized. These results together with the investigations illustrated in Fig. 3.3 in Chapter 3 demonstrate that a mutual coupling less than -15dB should be considered as unessential and neglected in the coupling matrix. Additionally, an increase of not only the number of probes but also the number of reference channels improves the calibration accuracy. Last but not least, the calibration accuracy can be further improved by an additional internal calibration procedure for the calibration probes.

8 Conclusion and Outlook

Besides the recent approaches of reflector antenna systems, electronically controlled phased arrays constitute another interesting approach for satellite communication systems in the near future. Furthermore, digital beam forming approaches show various advantages in comparison to the traditional phased arrays with analogue beam forming technique. Because of the capability to access and control the gain and phase of each channel, DBF systems feature high flexibility and adaptivity as their two main characteristics. Depending on the application scenario, such systems can be simply re-configured in software to fulfill the particular requirements. Additionally, because of the flexibility of the system, complex functions such as multi-beam operation or interference suppression can be implemented.

On the other hand, DBF antenna array systems for satellite communication applications are highly complex. Based on the calculation of the link-budget, more than 1000 channels are necessary in such communication systems with geo-stationary satellites. This means, the main task is integrating and controlling a huge number of active and passive components in a compact system.

The topic of the present work is the development and the analysis of an online calibration concept with external near-field probes for such a DBF receiver array. Therefore all relevant characteristics of antennas as well as of arrays are reviewed in Chapter 2. Besides, a multi-layer realization of a patch antenna as a receiver element with right or left circular polarization is presented, and experimental systems of linear and planar arrays are described.

In Chapter 3, the errors occurring in a receiver system are identified and then calibration concepts proposed in the literature are reviewed. Additionally, the advantages and disadvantages of these concepts are highlighted and compared in the context of large array applications. A so-called external concept is chosen for large-size arrays because of its low impact on integration density and its moderate hardware complexity.

The calibration of channel deviations is the topic of Chapter 4, the modeling of the probe-receiver coupling being one of three main topics discussed there. With regard to the trade-off between computational complexity and accuracy, an analytical coupling model is developed with a three-term-product approach under the assumption of stationary fields. Because of their compactness and robustness against fabrication tolerances, monopole antennas are used as calibration probes, their radiation pattern being approximately omni-directional. Furthermore, a Fourier-based model is proposed to represent the radiation pattern of the receiver patch which is placed in the array plane.

Finally, the propagation behavior of the calibration signals is derived from a system-based approach. Chapter 5 focuses on the calibration procedure. Based on a discussion of the cross-coupling in the system with its modular architecture, a simplified coupling matrix is proposed which is suitable for the online calibration task with limited hardware cost. Additionally, three decoupling algorithms are developed to perform the joint calibration of the channel fluctuations and the mutual coupling. The common Least-Square method is the first approach in case of a large number of probes and calibration signals with high SNR. As a second approach, a combination of Least-Square and Principle Component Analysis (PCA) is proposed and shown to achieve better calibration accuracy with a limited number of probes. Higher computational cost as well as a demand for larger SNR are its drawbacks. Thus, the PCA approach is suitable only for small-size arrays to achieve enough SNR of the calibration signals. Finally, an extension with multiple reference receivers is suggested to diversify the modeling errors of the probe-receiver coupling and therefore to improve the results. Higher hardware cost is associated with this approach.

In order to validate the usefulness of the proposed calibration procedure, experiments with linear and planar receiver arrays are demonstrated in Chapter 6. The demand for high SNR calibration signals as well as a good model of the probe-receiver coupling is first emphasized by the measurements with a printed microstrip probe. Whilst phase errors below 3° are achieved for the three-patch array, amplitude deviations of more than 2.5 dB are observed. As an improved implementation, a coaxial probe is employed in the other experiments. In the calibration of only the channel fluctuations, amplitude errors smaller than 1 dB and phase errors below 5° are demonstrated in the measurements of different sub-modules of a 4x4 array. Furthermore, the applicability of the proposed concept is also shown to compensate jointly the channel errors and the mutual coupling. Phase deviation smaller than 6° (8°) and amplitude fluctuation of 1 dB (2 dB) are achieved in the experiments of a linear 5x1 (planar 4x2) array.

The robustness of the proposed calibration concept is examined in Chapter 7 by means of a tolerance analysis. Because of huge number of channels and uncertainty variables, Monte Carlo simulations are chosen in this work. The relation between the calibration accuracy and the parameters of the calibration system, such as the SNR of the signals, the number of probes and reference channels are demonstrated.

In summary, the following enhancements of the on-line calibration with external on-board probes are demonstrated for the calibration of the channel deviations, namely:

- (1) an improved design of the calibration probes as well as an analytical model of the probe-receiver-coupling to enhance the calibration accuracy with acceptable calculation effort,
- (2) the theoretical examination and validation of the arithmetical and geometrical mean to improve the stability of the calibration procedure.

In addition, the concept is extended towards the joint calibration of the channel fluctuations and the

mutual coupling. The most important points are summarized as follows:

- (1) A simplified coupling model of the receiver system is shown to be necessary to limit the hardware cost.
- (2) The necessity of at least one isolated reference channel is demonstrated for the calculation with the Least-Square Method.
- (3) The extension of the algorithm by means of Principle Component Analysis is suitable only for the calibration of small-size receiver arrays because of the required SNR.
- (4) An increased number of not only the calibration probes but also the reference channels improves the calibration accuracy of the traditional Least-Square-Method, and is relevant for the calibration of a large-size receiver array.

Last but not least, for a given receiver system, a procedure based on a tolerance analysis is suggested to determine the technical requirements of the external near-field calibration system, such as the number of calibration probes and reference channels or the required SNR of the calibration signals. Finally, in future work modern algorithms, such as neural networks, could be considered as a possibility to enhance the performance of the calibration system over long working time. Besides, an additional internal "calibration" network could be implemented to compensate the deviations of the calibration signals of different probes, and increase the SNR as well as the accuracy of the calibration procedure.

Bibliography

- [1] Cisco: *Cisco Visual Networking Index: Forecast and Methodology, 2014-2019*. http://s2.q4cdn.com/230918913/files/doc_downloads/report_2014/white_paper_c11-481360.pdf, 2015.
- [2] D. Roddy: *Satellite Communications*. McGraw-Hill 2001.
- [3] H. Moheb, L. Shafai, M. Barakat, A. Kishk: *K/Ka-band offset reflector antenna system for personal satellite communications*. IEEE Conf. on Antennas and Propagation, Netherlands (1995).
- [4] G. Gothard, J. Kralovec: *Design of a Simultaneous Center-Fed X/Ka-Band SATCOM Reflector Antenna with Replacable C-band Option*. IEEE Military Communications Conference MIL-COM2007 (2007), 1–7.
- [5] A. Stark, A. Dreher, A. Fischer, A. Geise, R. Gieron, M. V. T. Heckler, S. Holzwarth, C. Hunscher, A. F. Jacob, K. Kuhlmann, O. Litschke, D. Lohmann, W. Simon, F. Woetzel, D. Zahn: *SANTANA: Advanced Electronically Steerable Antennas at Ka-band*. Proc. EuCAP 2009, Berlin (2009), 471–478.
- [6] S. Holzwarth, A. F. Jacob, A. Dreher, C. Hunscher, A. Fischer, A. Stark, B. Rohrdantz, A. Geise, K. Kuhlmann, R. Gieron, O. Litschke, D. Lohmann, W. Simon, P. Buchner, M. V. T. Heckler, L. A. Greda: *Active Antenna Arrays at Ka-Band: Status and Outlook of SANTANA Projects*. Proc. EuCAP 2010, Barcelona, Spain (2010), 1–5.
- [7] M. Geissler, M. A. Campo, M. Boettcher, P. Buchner, S. Bruni, R. Gieron: *Hochintegrierte Santana-Antenne fuer mobile applikationen: SAMOA: Schlussbericht zum Verbundprojekt*. <https://doi.org/10.2314/GBV:1017753113>, 2017.
- [8] C. A. Balanis: *Advanced engineering electromagnetics*. Wiley-Interscience 1989.
- [9] H. M. Aumann, A. J. Fenn, F. G. Willwerth: *Phased Array Antenna Calibration and Pattern Prediction Using Mutual Coupling Measurements*. IEEE Trans. Antennas and Propagation **37** (1989), 844–850.

-
- [10] T. Gao, Y. Gou, J. Wang, X. Chen: *Large Active Phased Array Antenna Calibration Using MCM*. IEEE International Symposium on Antennas and Propagation **2** (2001), 606–609.
- [11] R. H. M. Sanchez: *Calibration Technique for Phased Array Antennas* (2010) US20120154206.
- [12] T. W. Nuteson, J. E. Stocker, J. S. Clark, D. S. Haque, G. S. Mitchell: *Performance characterization of FPGA techniques for calibration and beamforming in smart antenna applications*. IEEE Trans. Microw. Theory Tech. **50** (2002), 3043–3051.
- [13] E. Lier, D. Purdy, J. Ashe, G. Kautz: *An on-board integrated beam conditioning system for active phased array satellite antennas*. Proc. IEEE Int. Conf. on Phased Array Syst. and Technol. (2000), 509–512.
- [14] A. D. Monk, C. O. Adler: *Calibration and RF Test of Connexion by Boeing Airbone Phased Array*. Proc. IEEE Int. Conf. on Phased Array Syst. and Technol. (2003), 405–410.
- [15] H. Pawlak: Ein externes Kalibrierverfahren für Gruppenantennen mit digitaler Strahlformung. Dissertation, Technische Universität Hamburg-Harburg, 2008.
- [16] R. J. Mailloux: *Phased Array Antenna Handbook*. Artech House, Inc. 2005.
- [17] R. J. Stegen: *Excitation Coefficients and Beamwidths of Tschebyscheff Arrays*. Proceedings of the IRE (1953), 1671–1674.
- [18] T. T. Taylor: *Design of line-source antennas for narrow beamwidth and low side lobes*. Trans. IRE (1955), 16–28.
- [19] J. Volakis: *Antenna Engineering Handbook*. McGraw-Hill 2007.
- [20] European Telecommunications Standards Institute, ETSI, *Satellite Earth Stations and Systems (SES); Harmonized EN for Satellite Interactive Terminals (SIT) and Satellite User Terminals (SUT) transmitting towards satellites in geostationary orbit in the 29,5 GHz to 30,0 GHz frequency bands (ETSI EN 301 459 V1. 4.1)*, European Telecommunications Standards Institute Std., Jun. 2007.: <http://www.etsi.org/deliver/etsi-en/301400-301499/301459/01.04.01-60/en-301459v010401p.pdf>, 2007.
- [21] N. Fourikis: *Advanced Array Systems, Applications and RF Technologies*. Academic Press 2000.
- [22] A. K. Bhattacharyya: *Phased Array Antennas*. Wiley-Interscience 2006.
- [23] D. E. Riemer: *Packaging Design of Wide-Angle Phased-Array Antenna for Frequencies Above 20 GHz*. IEEE Transactions on Antennas and Propagation **43** (1995), 915–920.

- [24] L. C. Stange: Integrationstechnik und Aufbauarchitekturen für aktive Antennensysteme im Millimeterwellenbereich. Dissertation, Technische Universität Hamburg-Harburg, 2005.
- [25] K. Kuhlmann: Hochintegrierte aktive Sendeantenne für den Millimeterwellenbereich. Dissertation, Technische Universität Hamburg-Harburg, 2013.
- [26] A. Stark: Ein Beitrag zur Skalierbarkeit von Empfangsantennen für die mobile Satellitenkommunikation. Dissertation, Technische Universität Hamburg-Harburg, 2013.
- [27] S. Holzwarth, O. Litschke, W. Simon, K. Kuhlmann, A. F. Jacob: *Far Field Pattern Analysis and Measurement of a Digital Beam Forming 8x8 Antenna Array Transmitting from 29.5 to 30 GHz*. The Second European Conference on Antennas and Propagation EuCAP 2007 (2007), 1–5.
- [28] K. Kuhlmann, K. Rezer, A. F. Jacob: *Circularly Polarized Substrate Integrated Waveguide Antenna Array at Ka-Band*. German Microwave Conference GeMIC 2008 (2008), 471–474.
- [29] K. Kuhlmann, A. F. Jacob: *Scanning Range of Circularly Polarized Antenna Arrays with Sequential Rotation*. German Microwave Conference GeMIC 2014 (2014).
- [30] J. K. Hsiao: *Array Sidelobes, Error Tolerance, Gain and Beamwidth*. ADA147004, 1984.
- [31] A. Swindlehurst, T. Kailath: *A performance analysis of subspace-based methods in the presence of model errors. I. the MUSIC algorithm*. IEEE Transactions on Signal Processing. (1992), 1758–1774.
- [32] C. M. Schmid, S. Schuster, R. Feger, A. Stelzer: *On the Effects of Calibration Errors and Mutual Coupling on the Beam Pattern of an Antenna Array*. IEEE Trans. Antennas and Propagation **61** (2013), 4063–4072.
- [33] A. H. Nuttall: *Some integrals involving the Q_M function*. IEEE Transactions on Information Theory **21** (1975), 95–96.
- [34] Y. T. Yu, H. S. Lui, C. H. Niow, H. T. Hui: *Improved DOA Estimations using the Receiving Mutual Impedances for Mutual Coupling Compensation: An Experimental Study*. IEEE Transactions on Wireless Communications **10** (2011), 2228–2233.
- [35] G. E. Evans: *Antenna measurement techniques*. Norwood, MA, Artech House, Inc. 1990.
- [36] K. Kuhlmann, D. Jalas, A. F. Jacob: *Mutual Coupling in Ka-Band Antenna Array with Polarization Multiplexing*. European Wireless Technology Conf. EuWIT 2009 (2009), 152–155.

-
- [37] A. D. Yaghjian: *An overview of near-field antenna measurements*. IEEE Trans. on Antennas and Propagation (1986), 30–45.
- [38] B. Friedlander, A. J. Weiss: *Direction Finding in the Presence of Mutual Coupling*. IEEE Transactions on Antennas and Propagation **39** (1991), 273–284.
- [39] W. Chen, J. P. Lie, B. P. Ng, T. Wang, M. H. Er: *Joint Gain/Phase and Mutual Coupling Array Calibration Technique with Single Calibrating Source*. International Journal of Antennas and Propagation **2012** (2012).
- [40] B. P. Ng, J. P. Lie, M. H. Er, A. Feng: *A Practical Simple Geometry and Gain/Phase Calibration Technique for Antenna Array Processing*. IEEE Transactions on Antennas and Propagation **57** (2009), 1963–1972.
- [41] B. Rohrdantz, A. Stark, E. Hawamdah, A. F. Jacob: *A circularly polarized antenna array with integrated calibration probes*. Asia-Pacific Microwave Conf. 2014, Sendai, Japan (2014).
- [42] N. Pham, A. F. Jacob: *Loop calibrator for DBF receiver array at Ka-band*. Asia-Pacific Microwave Conf. 2014, Sendai, Japan (2014).
- [43] T. Takahashi, N. Nakamoto, M. Ohtsuka, T. Aoki, Y. Konishi, M. Yajima: *A simple on-board calibration method and its accuracy for mechanical distortions of satellite phased array antennas*. The 3rd European Conference on Antennas and Propagation, Berlin, Germany (2009).
- [44] H. Pawlak, A. F. Jacob: *An External Calibration Scheme for DBF Antenna Arrays*. IEEE Transactions on Antennas and Propagation **58** (2010), 59–67.
- [45] Y. Rockah, P. M. Schultheiss: *Array Shape Calibration Using Sources in Unknown Locations - Part I: Far-field sources*. IEEE Trans. ASSP **35** (1987), 286–299.
- [46] A. J. Weiss, B. Friedlander: *Array Shape Calibration Using Sources in Unknown Locations - A Maximum Likelihood Approach*. IEEE Trans. ASSP **37** (1989), 1958–1966.
- [47] Keysight: *Keysight U9397A/C - FET Solid State Switches*. Technical overview.
- [48] B. Rohrdantz, T. Jaschke, F. Gellersen, A. Sieganschin, A. F. Jacob: *Ka-Band Antenna Arrays with Dual-Frequency and Dual-Polarized Patch Elements*. International Journal of Microwave and Wireless Technologies (2016), 963–972.
- [49] T. Su, H. Ling: *On Modeling Mutual Coupling in Antenna Arrays Using the Coupling Matrix*. Microwave and Optical Technology Letters **28** (2001), 231–237.

- [50] N. Pham, A. F. Jacob.: *Mutual Coupling Compensation of a DBF Receiver Array*. Proc. 45th European Microwave Conf. (2015).
- [51] Bureau International des Poids et Mesures: *Guide to the Expression of Uncertainty in Measurement, International Organization for Standardization*. <https://www.bipm.org/en/publications/guides/gum.html>, 1995.

Lebenslauf

Name	Pham
Vorname	Minh Nhat
Staatsangehörigkeit	Deutsch
Geburtsdatum	19.08.1985
Geburtsort, -land	Ho-Chi-Minh Stadt, Vietnam
09.1991 – 05.1996	Hoa-Binh Grundschule in HCM Stadt
09.1996 – 05.2000	Nguyen-Du Mittelschule in HCM Stadt
09.2000 – 05.2003	Gynasium für begabte Schüler in HCM Stadt
09.2003 – 03.2004	Deutschkurs in HCM Stadt
04.2004 – 08.2004	Deutschkurs in Bielefeld
09.2004 – 02.2005	Studienkolleg in Hannover
04.2005 – 08.2005	Studium an der Technische Universität Clausthal in Clausthal-Zellerfeld
09.2005 – 09.2011	Studium an der Technische Universität Hamburg Abschluss: Diplom Ingenieur
08.2011 – 05.2016	Wissenschaftlicher Mitarbeiter Institut für Hochfrequenztechnik Technische Universität Hamburg
06.2016 – 02.2017	Wissenschaftlicher Mitarbeiter Fraunhofer Institut für Zuverlässigkeit und Mikrointegration IZM Berlin
03.2017 – heute	Entwicklungsingenieur Robert-Bosch-GmbH Leonberg



9 783863 879594

mbvberlin

mensch und buch verlag | 2019

89,90 Euro | ISBN: 978-3-86387-959-4
